Symmetry-driven optoelectronics in two-dimensional layered materials

by

Jun Xiao

A dissertation submitted in partial satisfaction of the

requirements for the degree of

Doctor of Philosophy

in

Applied Science & Technology
and the Designated Emphasis
in
Nanoscale Science & Engineering

in the

Graduate Division

of the

University of California, Berkeley

Committee in charge:

Professor Xiang Zhang, Chair
Professor Feng Wang
Professor Michael F. Crommie

Spring 2018

Symmetry-driven optoelectronics in two-dimensional layered materials

Abstract

Symmetry-driven optoelectronics in two-dimensional layered materials

by

Jun Xiao

Doctor of Philosophy in Applied Science & Technology
and the Designated Emphasis in
Nanoscale Science & Engineering

University of California, Berkeley

Professor Xiang Zhang, Chair

Crystal symmetry and its breaking are the core of modern condensed matter physics and materials science research. They fundamentally determine the crystal topology, pairing mechanism and optoelectronic properties. They play a very important role in many novel phenomena such as quantum spin Hall effect in topological insulators, chiral fermion in Weyl semimetals and high temperature superconductivity in cuprates. Symmetry and related optoelectronic properties become more prominent in reduced dimensional systems, which have rich interfacial physics. For instance, in recent emerging 2D layered materials, inversion symmetry breaking and three-fold rotational crystal symmetry bring a unique valley degree of freedom. Meanwhile, large tunability of 2D materials are subject to external mechanical, electrical stimuli, or interfacial effects, which make symmetry engineering more feasible for potential applications.

This dissertation covers experimental investigation in the emerging fields of two-dimensional valleytronics and polar structural phases in 2D layered materials. Both are closely linked with fundamental crystal symmetry and specific symmetry breaking. The dissertation will first present the discovery of optical selection for nonlinear optical process in monolayer WS_2, while also taking into account both valley and excitonic degrees of freedom (DOF). The three-fold rotational crystal symmetry together with inversion symmetry breaking enables access to excitonic fine structures in specific valley through nonlinear optical processes with larger than 95% valley excitation efficiency. Such a discovery establishes a foundation for the control of optical transitions. This is crucial for valley optoelectronic device applications, such as 2D valley-polarized THz sources with $2p$–$1s$ transitions, and coherent control for quantum computing. Furthermore, the dissertation includes the first demonstration of electrical valley generation through ferromagnetic spin injection. The inversion symmetry breaking in monolayer TMDC leads to a unique spin-valley locking relationship, which is the key to achieve electrical valley generation. The electrical valley generation efficiency is up to 45%. Such high-fidelity achieved by electrical control opens the door towards a new paradigm of

electronics that manifests all three DOFs—charge, spin, and valley—for information processing.

On the other hand, the mirror symmetry breaking in 2D polar materials allows the exploration of novel structural ordering and associated optoelectronic properties in monolayer Janus MoSSe and ferroelectric ultrathin In_2Se_3 crystal. Significant vertical dipoles were observed in both materials by second harmonic generation (SHG) and piezoforce microscopy (PFM). In addition, the measured piezoelectric coefficient for a 3-nm-thick In_2Se_3 is about d_{33} = 0.5 pm/V and shows very high ferroelectric transition temperature T_c up to 700 K. These discoveries are applicable to electromechanical sensors and memory devices at molecular level.

Finally, the demonstration of electrostatic doping induced structural phase transition in monolayer $MoTe_2$ was discussed as an example for crystal symmetry manipulation. Such transition involves substantial crystal symmetry changes: from hexagonal to monoclinic and from inversion symmetry breaking to inversion symmetry preserved. SHG intensity modulation was observed more than one order during phase transition. This crystal symmetry engineering not only shows the capability for dynamic structural engineering at 2D limits, but also highlights the important role of electrostatic doping in controlling different phases, which benefits from weakly electrostatic screening in low-dimensional systems.

Table of contents

List of figures

Acknowledgments

It is my great honor to give thanks to my mentor Professor Xiang Zhang for his trust and generous support through the past six years, who always allocates resource and gives precious advice to me. I am grateful for the opportunity to join our diverse research group as well as the sharp and timely instructions during the years.

I thank Dr. Xiaobo Yin for the guidance on academic and non-academic topics at my early PhD stage, which have become my priceless assets.

I am indebted to Dr. Ziliang Ye and Dr. Kevin O'Brien for the skill training in optics. I am also grateful for the talented and kind colleagues in Xlab for their contributions to my research: Dr. Hanyu Zhu, Dr. Yuan Wang, Dr. Yu Ye, Dr. King Yan Fong, Dr. Mervin Zhao, Siqi Wang, Yousif Alsaid and Hanshen Huang. I thank all the other XLab members for the stimulating time together, as well as the dynamic and supportive atmosphere you have built: Dr. Boubacar Kante, Dr. Peng Zhang, Dr. Alessandro Salandrino, Dr. Tongcang Li, Dr Jia Zhu, Dr. Jie Zhu, Dr. Shaomin Xiong, Dr. Zi Jing Wong, Dr. Sui Yang, Dr. Jeongmin Kim, Dr. David Barth, Dr. Pankaj Jha, Dr. Rongkuo Zhao, Dr. Dafei Jin, Dr. Xingjie Ni, Dr. Yimin Li, Dr. Chad Ropp, Dr. Nicholas Bachelard, Dr. Cheng Gong, Dr. Xiaoze Liu, Dr. Wei Bao, Dr. Shoufeng Lan, Dr. Joseph Smalley, Dr. Pasquale Cilibrizzi, Chengzhi Shi, Yang Xia, Quanwei Li, Xuexin Ren, Haokun Li, Yi Jun, Renjie Tao and Zhaoyu Nie.

In addition, I thank Professor Lain-Jong Li, Professor Evan Reed, Professor Lane W. Martin, Professor David A. Muller, for support and helpful discussion. I am obliged to Dr. Ang-Yu Lu, Yimo Han, Prof. Wei Feng, Prof. Pingan Hu, Yunxia Hu, Arvind, Dr. Yao Li for the fruitful collaboration. Thanks for the help provided by Nga Thien Bui and Tracy Siira.

I also want to thank Professor Feng Wang and Professor Michael F. Crommie for serving in my committee.

Finally, I would like to give my very special thanks to my dear parents and my dear wife Ying Wang who are continuously offering me unconditional love and support through the ups and downs together.

PhD career is a unique experience to me. I experienced a lot and I have grown more than I expected. I really appreciate the resource and the care from Cal campus. I am also grateful for the guidance and the support from my lab and family. Berkeley is the place that shaped me and made me know what type of researcher and teacher I want to be. Go Bears!

1 Introduction

The symmetry in nature is always appreciated, starting from the galaxy our planet belongs to living bodies like butterfly with beautiful symmetric wings. In the field of solid state physics, it consists of various physical aspects of a material such as electrical, mechanical, optical, or magnetic properties. However, the microscopic arrangement of the atomic constituents of the material and the symmetry behind, governs all these physical properties. This can be lack of long-range order leading to a glass material or have a specific order with continuous rotational symmetry breaking leading to a crystalline material [1].

Finding the wonderful symmetries in a crystal is important. On the other hand, identification of symmetry breaking associated with a crystal is probably more amazing for the formation of novel phases. Both of which and the associated optoelectronic properties are the main subjects of this dissertation.

1.1 Crystal symmetry and symmetry breaking

A bulk crystal is a periodic array of atoms whose basic repeating unit is called primitive unit cell. The three linearly vectors $\boldsymbol{a_1}$, $\boldsymbol{a_2}$, and $\boldsymbol{a_3}$ are used to define the primitive unit cell volume. The array of points generated by the translational vector $\boldsymbol{T_{(n_1,n_2,n_3)}}$ is called a lattice.

$$\boldsymbol{T_{(n_1,n_2,n_3)}} = n_1 \cdot \boldsymbol{a_1} + n_2 \cdot \boldsymbol{a_2} + n_3 \cdot \boldsymbol{a_3} \tag{1.1}$$

where n_1, n_2, and n_3 are integer numbers. In a crystal lattice, each lattice site has the same surroundings and is at a corner of a primitive unit cell. Interestingly, the unit cells of a crystal structure can take only a certain number of distinct shapes because of the discrete translational symmetry requirement. This number is four for two-dimensional crystals and seven for three-dimensional crystals [2].

The beauty of symmetry in crystals also has its deep microscopic aspect. It is widely known that the microscopic and quantum nature of a crystal is unraveled by the solution to Schrodinger equation. This solution gives the energy eigenvalues and the wave eigenfunctions of Hamiltonian of the crystal, which are the foundation of observed physical properties. Importantly, the degeneracy and the transformation properties of the wave eigenfunctions are closely related to the symmetry properties of the Hamiltonian. In other words, the “exact” Hamiltonian as well as the eigenfunctions is invariant under corresponding symmetry operation if the crystal has such symmetry. Therefore, without diving into the details of atomic orbitals and bond strength, both degeneracy and transformation properties can be derived from the knowledge of symmetries, which is basis of group theory [3].

Besides the finding the wonderful symmetries that exists in a crystal, it is also amazing to identify specific symmetry breaking associated with the crystal. Symmetry breaking in a

crystal is a result of a decrease in the number of symmetry elements typically occurs at a phase transition. This reduction gives rise to a new lattice or electronic ordering type such as charge density wave, ferromagnetism, superconductivity [4]–[6], which can be probed by various technique such as X-ray structure analysis, neutron diffraction, Raman spectroscopy, optical absorption and electrical transport [7], [8].

Symmetry and symmetry breaking properties becomes more prominent in reduced dimensional systems with rich interfacial physics. The large tunability of 2D materials subject to external mechanical, electrical stimuli or interfacial effect makes symmetry engineering more feasible for potential applications. Among various type of symmetries in 2D layered crystals, two of them are under intensive exploration with substantial impacts.

One is inversion symmetry. Whether a crystal has inversion symmetry or not can be determined through inversion operation. The inversion operation occurs through a single point called the inversion center, *i*, located at within a unit cell of the crystal. Each atom in the unit cell is moved along a straight line through the inversion center to a point an equal distance from the inversion center ($\boldsymbol{r} \rightarrow -\boldsymbol{r}$). If after this operation, the unit cell is identical as before, then the crystal has inversion symmetry otherwise it is with inversion symmetry breaking (Fig. 1.1). This symmetry is quite important in contemporary research. It affects many physical properties like Berry phase [9] and second harmonic generation (SHG) [10]. More details about how inversion symmetry affect SHG will be elaborated in section 2.3.

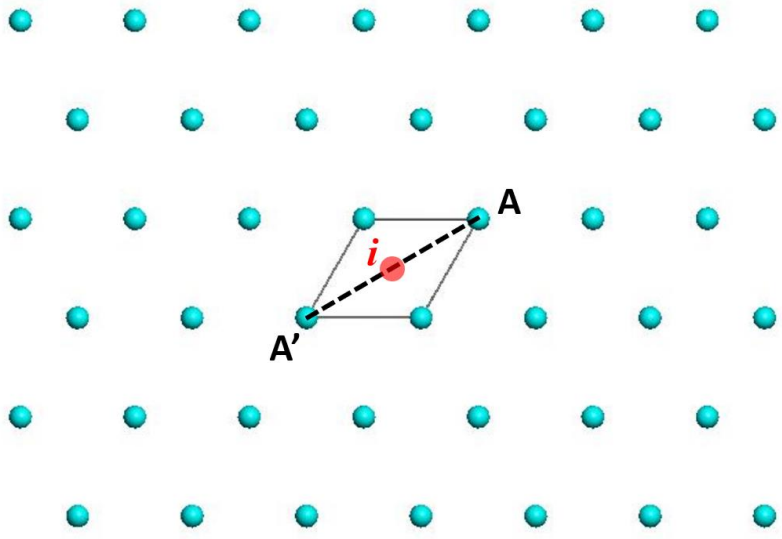

Figure 1.1: Inversion symmetry in a crystal lattice. Here *i* marks as the inversion center. An inversion operation takes any atom located at (*x*, *y*, *z*) and maps it through the inversion center *i* to (-*x*, -*y*, -*z*), like atom A to A'. If after this operation, the new lattice is

equivalent to original lattice, then it has inversion symmetry otherwise inversion symmetry in breaking in this system.

The other one is mirror symmetry. A crystal with mirror symmetry must have at least one mirror plane that divides the lattice into two halves and consequently one half is the mirror image of the other half across the plane (Fig. 1.2). One important example of mirror symmetry (or its breaking) is the absence (or presence) of chirality. Chirality is a fundamental property of an object not identical to its mirror image. It is an important concept widely applied in modern research like the discovery of handedness of neutrinos in electroweak interaction and helical structure of DNA in living bodies [11].

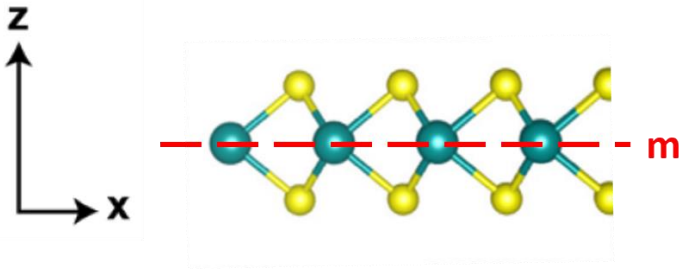

Figure 1.2: Mirror symmetry in a crystal lattice. This a side view of crystal structure of monolayer MoS_2. Yellow balls represent for sulfur atoms while green balls represent for Mo atoms. A mirror plane is labeled by "m" and indicated by the red dashed line. This mirror plane divides the lattice into two halves and one half is the mirror image of the other half. Therefore, this lattice has mirror symmetry (more specifically, it is out-of-plane mirror symmetry).

The exploration of the presence and absence of these two symmetries as well as associated optical properties in two-dimensional layered materials are the main targets of this dissertation. In next section, I may briefly overview of 2D layered materials for introductory purpose.

1.2 Two-dimensional layered materials

Since the discovery of graphene (first 2D layered material) in 2004 [12], the club of 2D layered materials is expanding rapidly with many distinct members such as transition metal dichalcogenide [13], [14], black phosphorous [15], metal carbides [16], III_2-VI_3 van der Waals crystal [17] , etc.

Generally speaking, layered materials are formed by specific order stacking of monolayers. In each layer, atoms are tightly bonded by ionic-covalent bonds while van-der Waals force provides weak interlayer attraction. The interlayer interaction governed

by van der Waals interaction is so weak that monolayer can be separated by mechanical exfoliation with scotch tape. Meanwhile, multiple synthetic methods such as chemical vapor deposition (CVD) can provide large-scale monolayer even not exist in nature. The mature of sample preparation guarantee a routine exploration of fundamental physics and device applications because of their emerging physical properties.

Here, I provide an overview of transition metal dichalcogenides, which is one type of the most important layered materials and weighs significant portions in this dissertation. Their crystal structures are summarized in figure 1.3. III_2-VI_3 van der Waals crystals, another type of 2D materials studied in this dissertation will be elaborated in chapter 4.

Layered transition metal dichalcogenides (TMDCs) in the form of MX_2 (M=Mo, W; X = Se, S, Te, etc.) are covalently bonded within the layer, but weakly bound by van der Waals interactions between each layer. Because of the three-atom layer nature, there are multiple crystal configurations in TMDCs such as 2H, 1T and 1T' phases. Exploration on above distinct phases and manipulation of their crystal symmetry are significant for understanding of interplay between distinct crystal symmetry in two-dimensionality and enable 2D reconfigurable device and 2D electronic memory.

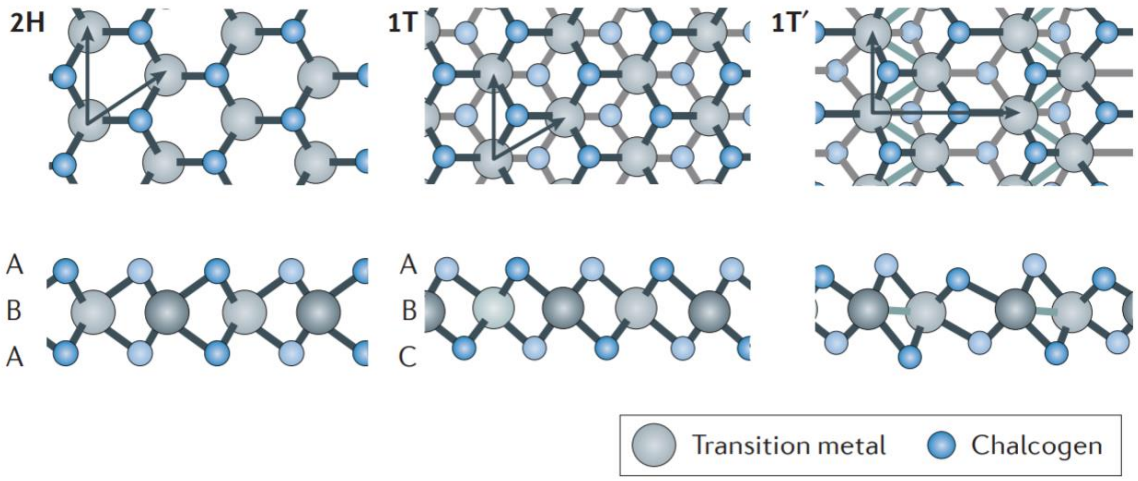

Figure 1.3: Crystal structure of transition metal dichalcogenides. Atomic structure of single layers of transition metal dichalcogenides (TMDCs) in their trigonal prismatic (2H), distorted octahedral (1T) and dimerized (1T′) phases. Lattice vectors and the stacking of atomic planes are indicated. Reprinted with permission from ref. [18]. Copyright Nature Publishing Group.

In 1T phase TMDC crystals, the X atoms are octahedrally coordinated around M atoms in rhombohedral stacking (ABC). If with a lattice distortion occurs along the in-plane axis,

the variation is termed as 1T' structure [19], [20]. Monolayer TMDCs in 1T and 1T' phase maintain inversion symmetry. In addition, TMDCs in 1T and 1T' phase are mostly semimetals or narrow bandgap semiconductors. Coupled with the strong spin-orbit interactions, monolayer 1T' crystals are predicted to host a non-trivial topological state with the quantum spin Hall effect [19].

Alternatively, in semiconducting 2H phase, transition metal M atoms are trigonally coordinated with chalcogen X atom layers in Bernal stacking (ABA). The inversion symmetry is broken in odd number of layers while restored in even number of layers due to AB stacking. Therefore, in its monolayer form, inversion symmetry is broken and the bandgap transitions from indirect in the bulk to direct in monolayers [14]. Meanwhile, large spin-orbital splitting manifests in both conduction band ($\sim$ 10 meV) and valence band ($\sim$ 100 meV) [21]. The semiconducting 2H phase has been associated with rich optical and electronic semiconductor characteristics such as the emergence of strong excitonic many-body effects [22]–[24]. More interestingly, the inversion symmetry breaking in 2H monolayer allows the presence of unique valley degree of freedom [25]–[27].

In a crystalline solid momentum space, a local minimum in the conduction band or local maximum in the valence band is defined as a valley. In addition to charge and spin, an electron can also have so-called valley degree of freedom or valley index that indicates which valley that the electron occupies. Valleytronics refers to using such valley degree of freedom to store and process information [28]. An ideal valleytronic material system has a band structure composed of two or more energy-degenerate but inequivalent valley states that can be manipulated to encode, process and store information. This requirement is typically satisfied by inversion symmetry breaking to lift degeneracy.

There are several unique parts for valleytronics compared with current electronics and spintronics technology. First, pure valley current can flow without net charge current, the Ohmic loss can be reduced and heat dissipation can be further reduced if intervalley scattering by phonon is not significant. Second, valley degree of freedom as a discrete index can be used for quantum information process. Third, such quantum index is quite robust and can exist as long as the crystal structure unchanged. Fourth, unlike conventional spintronics which utilize binary electron spin states, the valley degree of freedom is determined by crystal structure and electron orbitals. In principle, a system can have more than two valley indices. With multiple valley indices, multiple information channels can be established and boost the information transmission/processing speed. Finally, unlike spintronic applications, valleytronic platform does not necessarily require the presence of local magnetic field.

With all above advantages, it is quite appealing for fulfillment of valleytronics, an important branch of optoelectronics.

1.3 Uniqueness of 2D materials for optoelectronic applications

Compared with the bulk crystal, layered materials with reduced dimensions have three distinct features. Firstly, two-dimensional system has highly confined in-plane motion of quasiparticles. Secondly, enhanced interactions among quasiparticles due to weak dielectric screening. Finally, physical properties of layered materials can be easily tuned by electrical, mechanical and other external stimuli, facilitating the development of device applications such as versatile memory. In the following, I would go through above features in 2D materials and elaborate the unique physics and potential novel optoelectronic applications for 2D valleytronics as well as phase manipulation.

A. Highly confined in-plane motion of quasiparticles

Low-dimensional systems are realized by confining its particle's movement in a dot, line or plane. For instance, in layered materials, the van der Waals nature dominates interlayer interaction while strong covalent or ionic bond saturates within each layer. This strong anisotropy leads to highly confined electron motion within each layer as well as corresponding band structure. In such scenario, the density of possible quantum modes of the particle at a given energy (density of states, DOS) is quite different from that in bulk. In ideal 2D system with parabolic E-k dispersion ($E_k = \frac{(\hbar k)^2}{2m^*}$), the density of state is in the following fashion:

$$D(E) = \frac{d\Omega}{dE} \propto m^* E^0 \tag{1.2}$$

It is quite different from converging feature in 3D case at low energy limit (Fig. 1.4). Such nonconvergent density of states even for E→0 leads to several important theorems and findings in low dimensional systems such as Mermin-Wagner theorem and BKT phase transition.

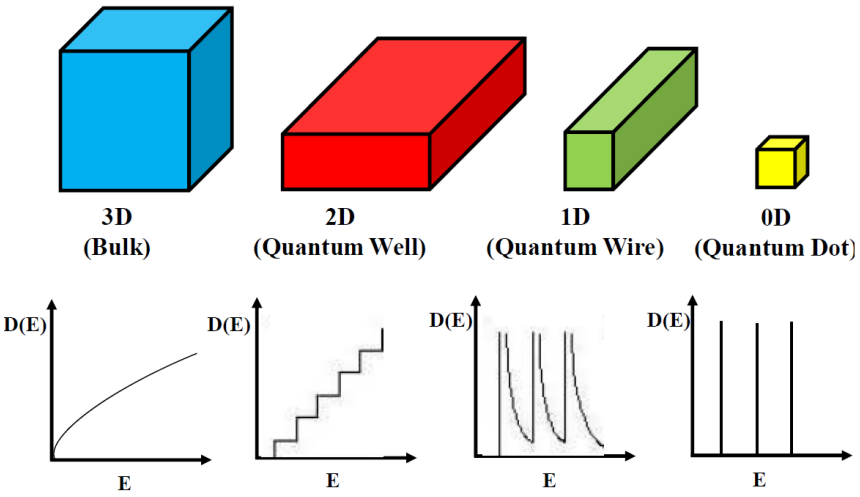

Figure 1.4: Schematic diagram of density of states for different dimensional systems. Reprinted with permission from ref. [29]. Copyright MDPI.

Besides, such highly confined motion not only results in discrete density of states plateau, but also has impact on physical properties of novel phase such as superconductivity formation, which originates from competition between electron-electron and electron-phonon interactions. For example, high in-plane critical magnetic fields up to 100 T for superconducting phases were discovered in ion-gated MoS_2 and intrinsic $NbSe_2$ ultrathin flakes [30]–[32]. In conventional superconductors, applying a sufficiently high magnetic field can destroy superconductivity via the coexisting orbital and Pauli paramagnetic mechanisms. The orbital contribution represents electron circulation and vortex formation induced by the magnetic field, while the paramagnetic contribution originates from spin realignment in Cooper pairs by an external magnetic field. However, in ultrathin-layered materials, carriers are strongly confined to only move in their host layer. Therefore, out-of-plane electron circulation induced by in-plane magnetic field is forbidden. On the other hand, Cooper pairs in ultrathin TMDC such as MoS_2 are formed by electrons with opposite spins locating at the K and K' valleys of the conduction band. The in-plane inversion symmetry breaking and large spin-orbit coupling in a MoS_2 monolayer lead to significant spin splitting in conduction band, which manifests as a Zeeman-like effective magnetic field B (~100 T) oppositely applied at the K and K' valleys (Fig. 1.5 inset). Antiparallel spins in the Cooper pairs are pinned by this large out-of-plane Zeeman field. Therefore, the temperature dependent resistance curve as well as superconducting transition temperature are barely affected by in-plane magnetic fields [31] (Fig. 1.5). Such Ising-like pairing prevents spin reorientation from an in-plane magnetic field up to 55 T in sample with optimized conditions at 1.5 K [30].

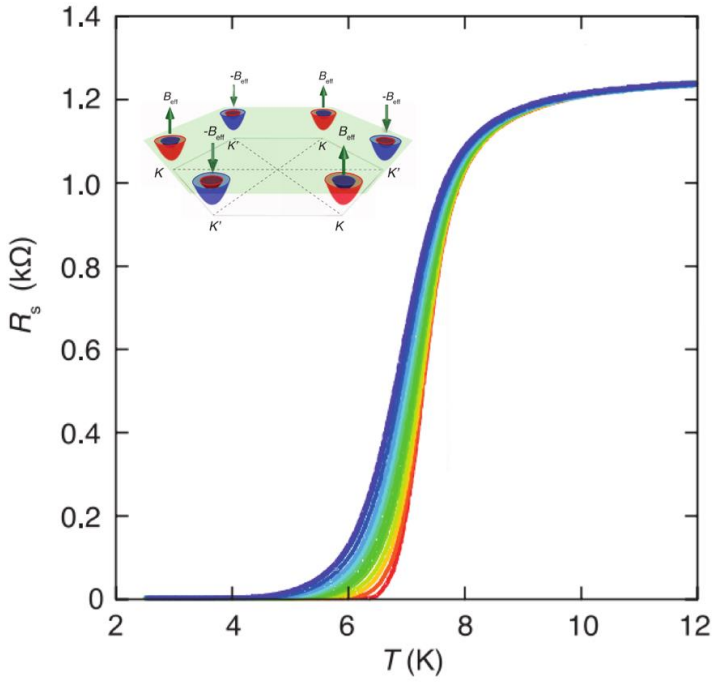

Figure 1.5: Temperature dependent resistance under a static in-plane magnetic field. The resistance curve and transition temperature are weakly dependent of in-plane B field up

to 11 T due to the effective Zeeman field pinning. The inset plots out the electron pockets in conduction band of monolayer MoS_2 and effective Zeeman field pinning. Because of strong spin-orbit coupling and inversion symmetry breaking, electron pockets with spin up (blue) and spin down (red) split oppositely at the K and K' valley. Such energy splitting indicates electrons in K and K' valley experience opposite effective magnetic Zeeman fields B_{eff} and $-B_{eff}$ (green arrows) and are immune to perturbation from external in-plane magnetic field. Reprinted with permission from ref. [31]. Copyright AAAS.

B. Enhanced quasiparticle interaction due to weak electrostatic screening

Electron-phonon and electron-electron interactions are main quasiparticle interactions in a crystal. The interplay of these two interactions dominate the electronic response (sometimes even influence structural reconfiguration) and lead to novel phenomena such as superconductivity, Mott insulator and excitonic effect.

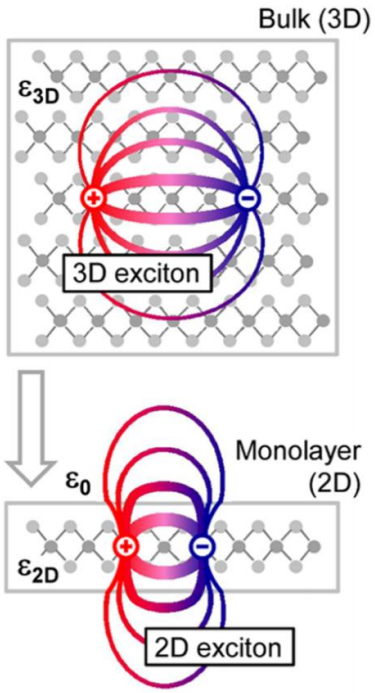

Figure 1.6: Real-space representation of electrons. The changes in the dielectric environment are indicated schematically by different dielectric constants ε_{3D} and ε_{2D} and by the vacuum permittivity ε_0. Reprinted with permission from ref. [24]. Copyright American Physical Society.

In typical bulk semiconductor crystals such as silicon, the large dielectric screening and small quasiparticle effective mass result in small exciton binding energies, only ~1-10s of meV [33]. Thus, the bound behavior of the exciton is insignificant compared to the thermal fluctuations unless cooled down to low temperatures. In contrast, the bound exciton states often dictate the optical properties of two-dimensional (2D) materials such as monolayer transition metal dichalcogenides (TMDCs). The strong Coulomb interaction in low-dimensions and reduced dielectric screening, compared to bulk crystals, naturally makes the excitons bound even at room temperature with a binding energy of hundreds of meV. The reduced dielectric screening can be understood based on Fig. 1.6. The schematic shows electric field line distribution between an electron-hole pair in a bulk crystal and an ultrathin film. In bulk crystal, the electric field lines penetrate through the large dielectric environment contributed by surrounding atoms. However, for a 2D crystal, significant portion of electric field lines penetrate into vacuum or air which has low dielectric constant about 1. Therefore, the quasiparticle interaction is enhanced with such reduced average screening.

C. Large tunability subject to external stimuli

The reduced dimensionality of these semiconductors enables the large tuning of optical properties via external stimuli such as applied electric fields and mechanical strain. This is a huge plus for fundamental phase transition physics exploration as well as tunable valleytronic devices.

The atomically-thin nature of TMDCs and its weak electric screening makes the carrier density easily tunable and high doping density from $10^{13}/cm^2$ to $10^{15}/cm^2$ achievable, using a FET structure based on solid or liquid capacitor. K. F. Mak *et al*. first observed that tuning the carrier density to high electron populations changes the absorption spectra (Fig. 1.7a) and the photoluminescence (PL) from the exciton to the tightly bound negative trions (X^-), a quasiparticle composed of two electrons and a hole [34]. The negative trion also possess a large binding energy (~ 20 meV), such that robust trion photoluminescence can be detected at room temperature (Fig. 1.7b). In addition, circularly polarized resolved gate-dependent PL showed helicity from emission of trions, which indicates such quasi particles can be optically created with valley and spin polarized holes. In parallel, J. S. Ross, *et al.* investigated the electrostatic gate effect on photoluminescence of positively charged (X^+), neutral (X^0) and negatively charged (X^-) excitons in a single layer of $MoSe_2$. Such large binding energy results from the enhanced Coulomb interaction due to the strong confinement and heavy effective masses [35]. Also, they found the extra charge binding energies for X^+ and X^- to be nearly same indicating the similar effective mass for electrons and holes, which is consistent with theoretical calculations. The exciton's large electrical tunability in oscillation strengths also modifies the nonlinear spectrum. K. L. Seyler, *et al.* show how the electrostatic doping via the transistor gate is able to change the SHG magnitude (Fig. 1.7c, 4d). The SHG amplitude at the A-exciton resonance varied about four times at room temperature (Fig. 1.7e) and over an order of magnitude at low temperature and nearly a factor of four at room temperature [36]. All of the above studies revealed the large electrical tunability on

excitonic spectroscopy in 2D TMDCs associated with carrier density dependent many-body Coulomb interactions.

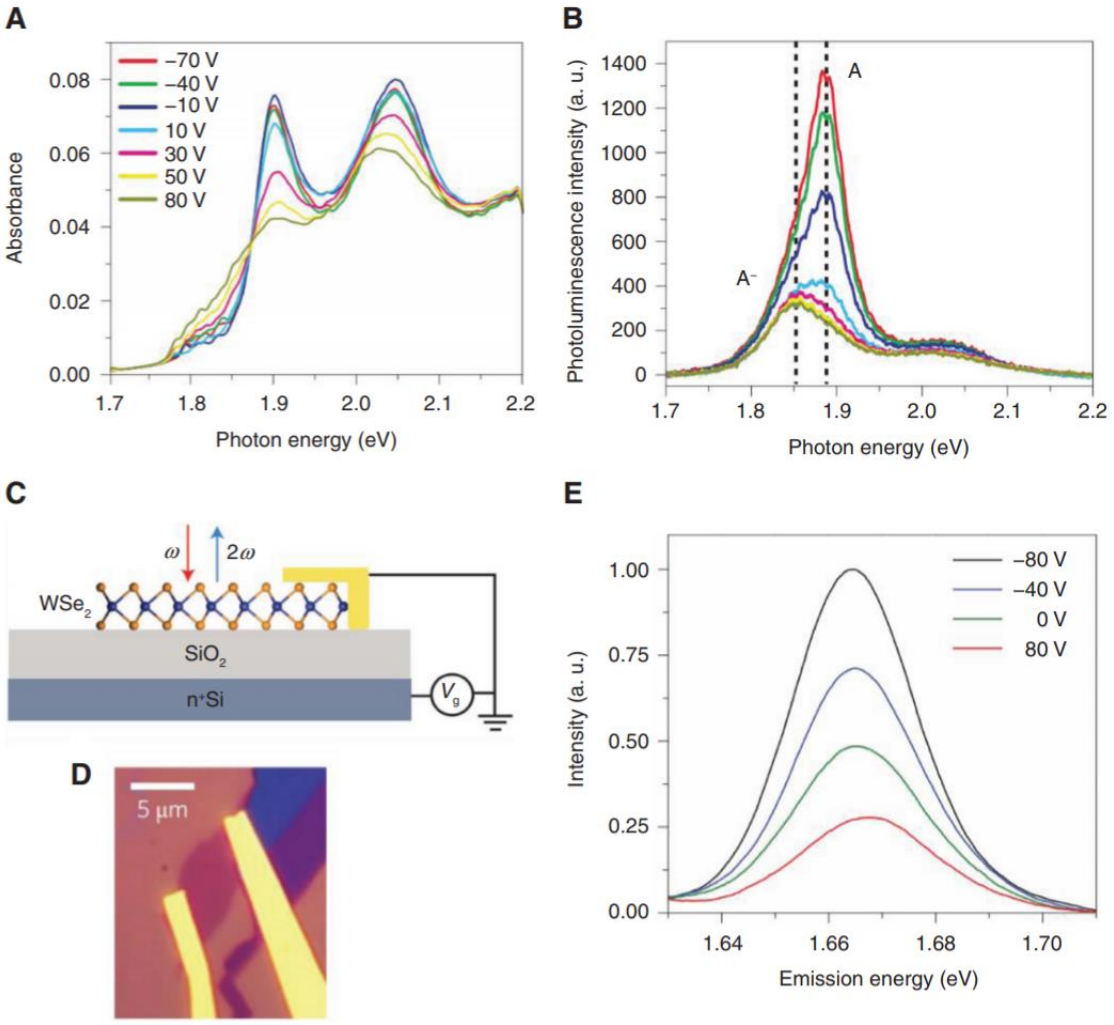

Figure 1.7: Electrical tuning of optical properties in 2D layered materials. **A,** Monolayer MoS_2 absorption spectra at different back-gate voltages in a FET device. The global absorption with significant "A" exciton (1.92 eV) and "B" exciton (2.08 eV) shows amplitude variation, peak shift, and linewidth change under different gate bias. **B,** Photoluminescence spectra of same device under different back-gate bias. Here "A−" is the trion. **C,** Schematic of a monolayer WSe_2 transistor for second harmonic generation. **D,** Microscope image of the transistor. The WSe_2 is the light purple area between two metal electrodes. **E,** SHG spectra on "A" exciton resonance under different gate bias at room temperature. The intensity increases about four times when the bias switches from 80 V to −80 V. (A–B) Reprinted with permission from ref. [34]. (C–E) Reprinted with permission from ref. [36]. Copyright Nature Publishing Group.

The large electrical doping tunablity in atomically thin materials also has a huge impact on the superconductivity phase transition. Researchers observed a superconducting dome for few layer MoS_2 in the temperature–carrier density phase diagram [37]. By fabricating top ionic-liquid and bottom solid gates on few layer MoS_2, they were able to modulate the carrier density up to $10^{14}/cm^2$ without any disorder generation, in contrast to permeant chemical doping. After injecting carriers into MoS_2 with different liquid-gate biases V_{LG}, they measured the four-terminal sheet resistance Rs as a function of temperature T down to 2 K. At gate biases $V_{LG} < 1$ V, they found a negative temperature derivative of Rs (dRs/dT), a signature for insulating states. While for $V_{LG} \geqslant 1$ V, the channel shows metallic transport with positive dRs/dT due to increasing doping density. The metallic behavior becomes more significant with further increase of V_{LG}, and finally the MoS_2 flake shows superconductivity at $V_{LG} = 4$ V. Varying both V_{LG} and V_{BG}, they mapped out log Rs in the carrier density n_{2D} and temperature T plane (Fig. 1.8). In this phase diagram, the superconducting temperature can be tuned and optimized by carrier density. More importantly, a clear dome-shape superconducting regime was observed. This type of dome regime is common in many other high-T_c superconductors like cuprates [38], [39], where transition temperature can be optimized by external parameters. Based on this similarity, achievements on one system may help exploration on the other.

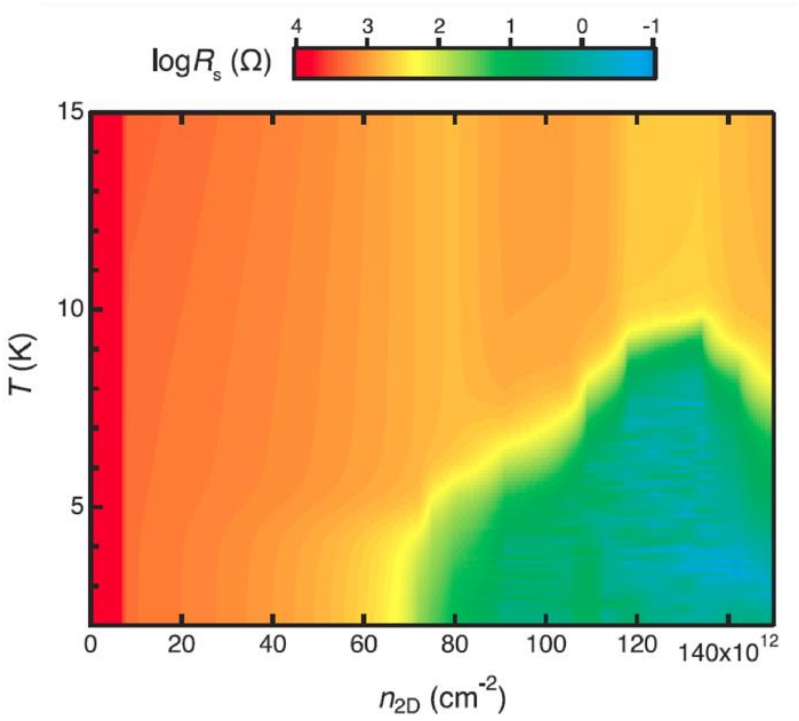

Figure 1.8: Phase diagram of gate-tuned MoS_2. The color represents the logarithm of the sheet resistance R_S, as indicated in the top color bar. By controlling temperature and carrier density, an insulating ($n_{2D} < 6.7 \times 10^{12}$ cm^{-2}), a metallic ($6.7 \times 10^{12} < n_{2D} < 6.8 \times 10^{13}$ cm^{-2}), and a domelike superconducting phase ($n_{2D} > 6.8 \times 10^{13}$ cm^{-2}) was observed.

Such significant dome shape shows the MoS_2 T_c can be tuned by carrier density with an optimal value of about 10 K. Reprinted with permission from ref. [37]. Copyright AAAS.

Later, researchers demonstrated such gate-induced superconductivity in MoS_2 persists down to a monolayer [40]. Strikingly, compared with 2-6 layers MoS_2, the maximum T_c in monolayers is suppressed, and a 'jump' from ~6–7 K to 2 K was seen. In addition, the out-of-plane critical magnetic field in monolayers is more than one order of magnitude smaller ($B_c \approx 0.05 - 0.1$ T, compared with 5–10 T for the 6 L device). The authors claimed such discrepancy cannot be solved even considering the factor of different density per layer. Although the mechanism for this layer dependence is not clear, the author claimed three factors may account for the observations: Firstly, stronger thermal and quantum fluctuations at the 2D limit which suppress the superconducting order [41], [42]. Secondly, enhanced Coulomb repulsion in the monolayer leads to a weaker strength of the effective attractive interaction and a reduced superconducting critical temperature [43], [44]. Thirdly, based on ab initio calculations [45]–[47], electrons added to the conduction band of MoS_2 monolayers initially fill states close to the K (and K') point and that for thick multilayers electron accumulation first occurs at the Q point, where strength of the electron–phonon interaction and the density of states are different. Nevertheless, such gate-induced superconductivity is unique to ultrathin-layered materials and exclusively unravel the critical role of electrons in superconducting transition without introducing any disorder and degrade transport performance, compared with conventional chemical doping.

The mechanical flexibility is another unique advantage for 2D materials [48]. With mechanical strain, the electronic band structure linked with the lattice constant changes accordingly. Therefore, optical properties, especially inter-band transitions, in TMDC are expected to vary. By putting atomically thin MoS_2 on flexible substrates, K. He *et al.* demonstrated the continuous tuning of the electronic structure when applying a uniaxial tensile strain. As large as 70 meV redshift per percent of applied strain for direct gap transitions has been observed by absorption and photoluminescence spectroscopy [49]. Similar observation has also been reported by H. J. Conley, *et al.*, where uniaxial tensile strain in the range 0−2.2% modifies the phonon spectra and electronic band structure of monolayer and bilayer molybdenum MoS_2 (Fig. 1.9a,b) [50]. Photoluminescence spectroscopy indicates an energy decrease of 45 meV per percent strain for single layer and 120 meV per percent strain for bilayer MoS_2 in the optical band gap (Fig. 1.9c). In addition, given different strain dependent response for carriers with different effective mass, a direct-to-indirect transition of the optical band gap accompanies a pronounced decrease in the photoluminescence intensity at an applied strain of ~1%. From the Raman spectroscopy, phonon modes soften with increased strain and break the degeneracy in the E' Raman mode of MoS_2.

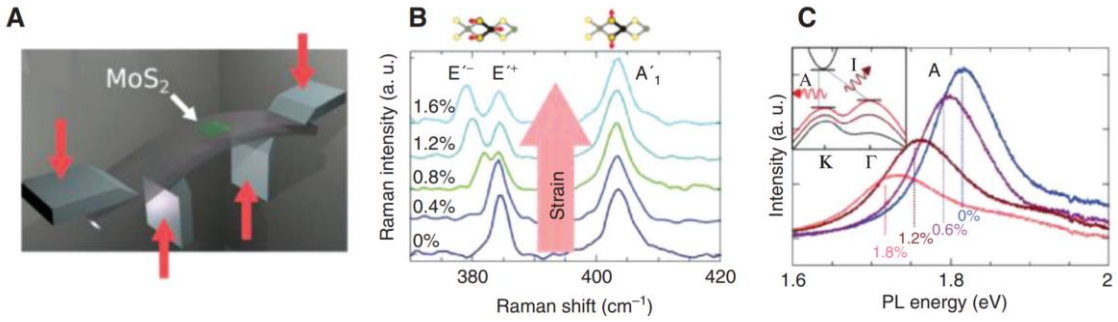

Figure 1.9: Mechanical tuning with strain. **A,** Schematic of the bending setup to strain MoS_2. Ultrathin MoS_2 flakes are clamped with titanium on a SU8/polycarbonate substrate that is strain-tunable. **B,** Raman spectrum as function of the in-plane strain in monolayer MoS_2. The out-of-plane oscillation A_{1g} mode shows almost no change under in-plane strain. In contrast, the in-plane oscillation E_{2g} displays peak shift and peak splitting into two modes with increasing strain. **C,** Photoluminescence of strained monolayer MoS_2. By applying strain, PL emission intensity decreases and peak position shifts to lower energy. The inset shows the competition between direct and indirect transition under strain MoS_2. Reprinted with permission from ref. [50]. Copyright American Chemical Society.

In summary, because of distinct electronic density of states, spatial confinement, and weak dielectric screening, it is expected that the 2D phase transitions reveal unconventional symmetry evolution such as formation of vortex-antivortex pair under enhanced Coulomb interactions. Meanwhile, such van der Waals crystal can be transferred to many substrates to explore interfacial physics or stacked to form artificial heterostructures for new crystal symmetry and functionality [51]–[53]. The 2D nature of layered materials enables large tunability in its physical properties with a number of external stimuli [54], which paves the way for exploration on non-thermal driven quantum phase transition and 2D optoelectronic applications.

1.4 Structure of the dissertation

Based on the discussion above, two-dimensional materials with specific crystal symmetry are unique research platforms for optoelectronics exploration, owning to their large tunability, highly confined in-plane carrier motion together with the strong quasiparticle interaction. Along this line, this dissertation presents five closely related works in the following sequence:

- Chapter 2: Nonlinear valley exciton optical selection rule in monolayer WS_2. Content comes from ref. [55].
- Chapter 3: Electrical valley generation based on spin-valley locking in monolayer WS_2. Content comes from ref. [56].
- Chapter 4: Ordering exploration in 2D polar crystals. Content comes from ref. [57] and [58].

- Chapter 5: Structural symmetry engineering in monolayer $MoTe_2$. Content comes from ref. [59].

2 Nonlinear valley exciton optical selection rule in monolayer WS_2

2.1 Introduction to generalized optical selection rule

The fundamental principles dictating allowed and forbidden optical transitions between energy states in a variety of physical systems are called optical selection rules. Such selection rules govern from hydrogen atoms to bulk crystals such as gallium arsenide. These rules are important for optoelectronic applications such as lasers, energy-dispersive X-ray spectroscopy, and quantum computation. Such requirements are originated from various symmetries present in the specific physical system. These symmetries include temporal translational, spatial translational, and rotational symmetry, and their corresponding laws of conservation of energy, momentum, and angular momentum according to Noether's theorem, as shown in Fig. 2.1. Strict derivations can be done and is summarized in well-known "Fermi golden rule". For example, in order to have significant transition probability, the photon energy should match the energy difference between initial and final states (Fig. 2.1(a)). Furthermore, in solid crystal where one electron travels in period lattice, the photon momentum should exactly compensate quasi-momentum mismatch between initial and final states (Fig. 2.1(b)). Typically, the quasi-momentum in crystal is on the scale of the inverse of lattice constant (~ nm), while typical visible photon wavevector is on the order of the inverse of hundreds of nm. Therefore, only when the quasi-momentums are almost the same for the initial and final states, one can expect significant transition probability given negligible photon wavevector. Finally, based on angular momentum conservation requirement, the angular momentum contributed by an electron's orbit and spin can be explored with suitable circular polarized light excitation (Fig. 2.1(c)). This is important to reveal the symmetry of electronic states in atoms, molecules and crystals, which has been widely used in atomic emission spectroscopy, controlling the polarization of semiconductor light-emitting diodes and lasers, and optically manipulating spin polarization in spintronics [60], [61].

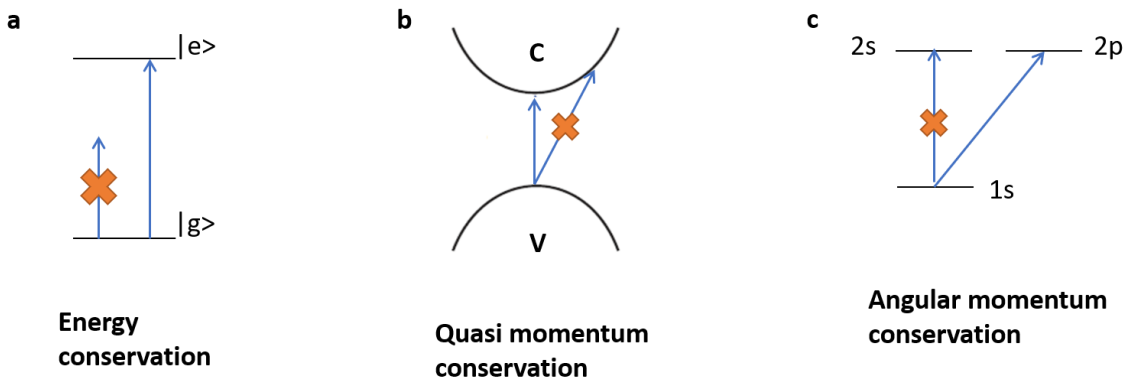

Figure 2.1: Optical selection rule based on conservation laws.

2.2 Unique valley and excitonic degree of freedoms in 2D TMDC

In conventional selection rule studies of solids such as bulk gallium arsenide and their quantum wells, it has long been thought that the angular momenta of Bloch electrons are inherited exclusively from their atomic orbits. On the other hand, the role of intercellular electron motion in selection rules received little attention due to the absence of corresponding physical candidates, which can contribute only when the physical system has inversion symmetry breaking and optical transitions off the center of the Brillouin zone [62]. However, the recent discovery of valley angular momentum (VAM) in transition metal dichalcogenide (TMDC) monolayers, which have a direct bandgap at the edge of the Brillouin zone and lack inversion symmetry [25], raise both fundamental and application interests to utilize such valley dependent intercellular electron motion. In the meantime, the weak dielectric screening in 2D materials results in strong excitonic effect even at room temperature. In the following, such unique valley and excitonic degree of freedom will be reviewed, which substantially determine the optical selection rules in layered TMDC.

Valley degree of freedom in 2D materials

The valley degree of freedom (DOF) is associated with energy valleys in momentum space. In a crystalline solid momentum space, a local minimum in the conduction band or local maximum in the valence band is defined as a valley. In addition to charge and spin, an electron can also have so-called valley degree of freedom or valley index that indicates which valley that the electron occupies. Valleytronics refers to using such valley degree of freedom to store and process information [28].

The history of research on valley DOF in 2D materials can be traced back to the discovery of graphene. Given graphene's honeycomb carbon lattice, its band structure takes the form in a hexagon Brillouin zone in the momentum space. At each corner (the K point), the minimum of the conduction band will touch the maximum of the valence band and forms a gapless Dirac cone, in which the carriers behave like massless Dirac

fermions. These “valleys” at the K point, are a degree of freedom that the electron has, in addition to charge and spin. Graphene’s Brillouin zone hosts two sets of valleys, at the K and –K points. Controlling which valley the electron resides in has the possibility to carry quantum information. However, graphene has had difficulty in generating a “valley population or current”, because of the presence of inversion symmetry. Inversion symmetric crystals like graphene, Berry curvature **Ω** and orbital angular momentum **m** must take on the same values under inversion, thus K and –K become indistinguishable. It is necessary to break the inversion symmetry of crystal to generate of a valley polarization to differentiate the ±K valleys [63].

In contrast, the inversion symmetry is breaking in transition metal dichalcogenides (TMDCs, group VIB: MoS_2, $MoSe_2$, WS_2, WSe_2) monolayers. These are layered van der Waals crystals with a trigonal prismatic crystal coordination. The transition metals are hexagonally arranged in a plane and sandwiched between two chalcogen layers. As shown in figure 2.2, These crystals are semiconductors with an indirect band gap in the bulk form that transitions to a direct band gap in the single layer at the ±K points [9].

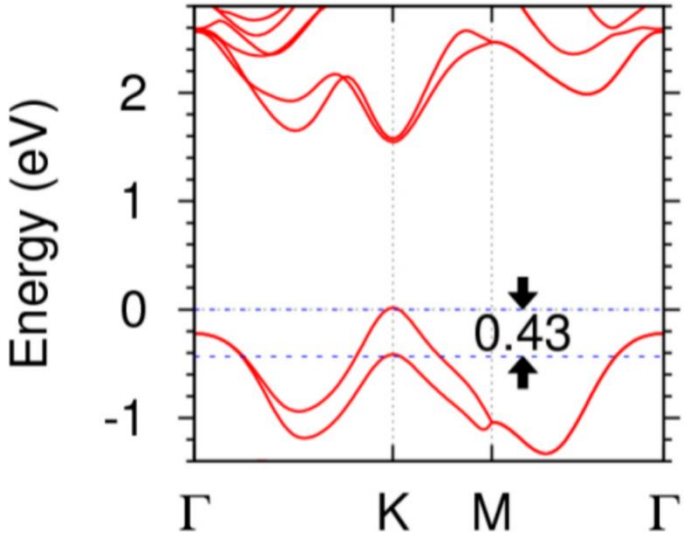

Figure 2.2: Band structure of monolayer TMDC. The direct band gap located at +K/-K points, which are the Brillion zone corners. Reprints with permission from [64]. Copyright Nature Publishing Group.

Early theoretical works pointed out nonzero Berry curvature associated with two sets of energy valleys in momentum space (K and K’ valleys), shown in figure 2.3. This is the direct consequence of angular momentum of Bloch electrons including contributions from not only individual atomic orbits but also the circulation of electrons from one atomic site to another throughout the crystal unit cell (Fig. 2.4) . The Berry curvatures have opposite sign thus distinguishable values at K and K’ valleys, thus Bloch electrons in adjacent valleys have valley angular momentum (VAM) with opposite signs and follow a valley-dependent optical selection rule in the linear spectrum. For example, in

MoS_2, three independent works showed that excitation of the K (–K) valley with σ– (σ+) light result in photoluminescence (PL) of the same polarization, generating a valley polarization through optical excitation [26], [27], [65].

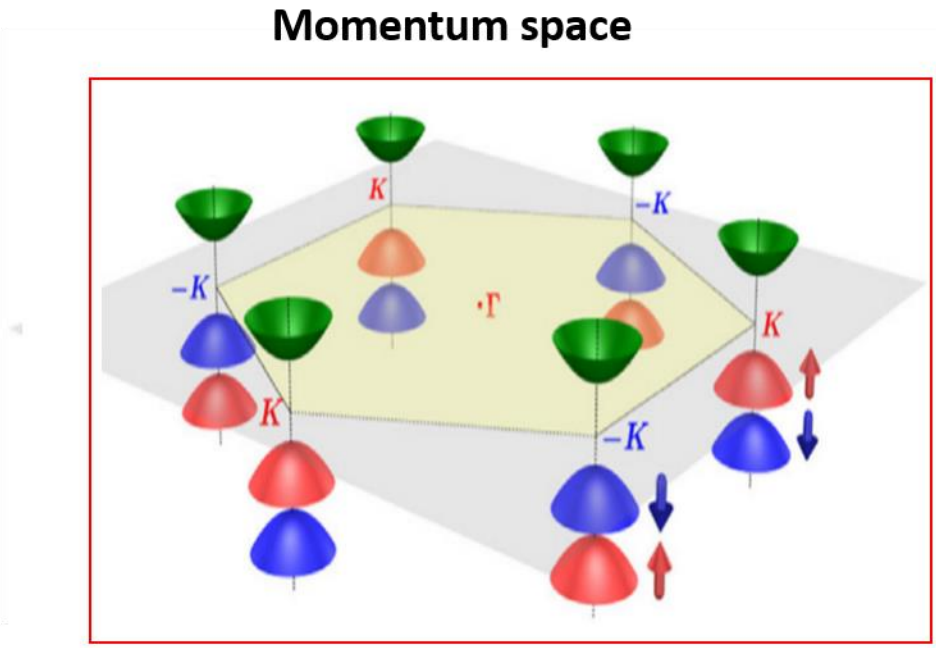

Figure 2.3: Valley dependent momentum space in monolayer TMDC. Reprints with permission from [66]. Copyright American Physical Society.

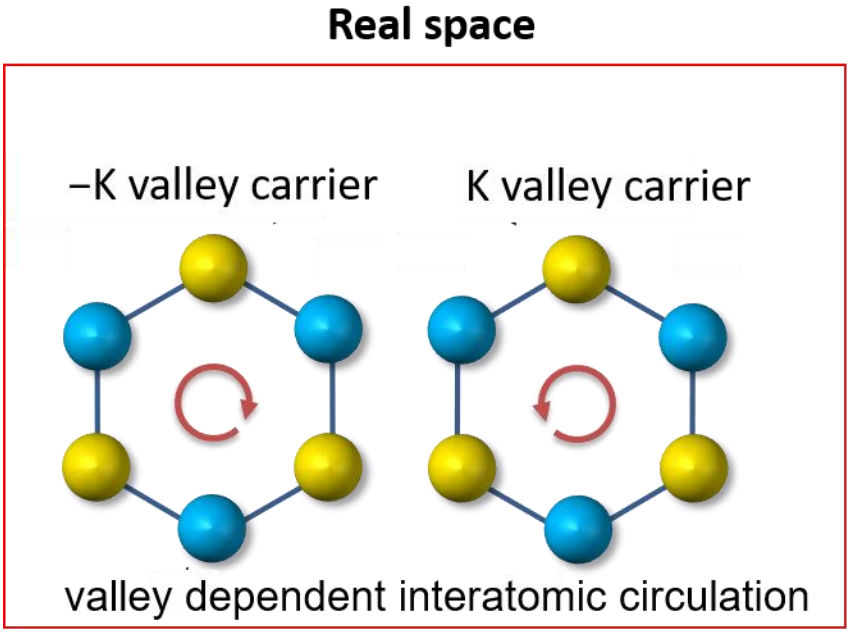

Figure 2.4: Valley dependent interatomic circulation in real space.

Excitonic effect in 2D materials

Another unique property discovered in monolayer TMDCs is giant excitonic effect. Excitons are hydrogen-like bound states formed by a negatively charged electron and a positively charged hole due to the Coulomb attraction. Typically, excitons result from the photo-excitation in semiconductors, as shown in figure 2.5. Excitons can exhibit spectrally narrow line-width and a large oscillator strength with enhanced light-matter interaction, allowing for efficient recombination and emission of light. The particle has its own internal fine structure with hydrogen-like excited energy states, potentially enabling future excitonic-carrier devices in quantum computation and excitonic circuits. In addition, as excitons are Bosonic particles, they can condensate to form Bose-Einstein condensates and exhibit superfluid-like transport.

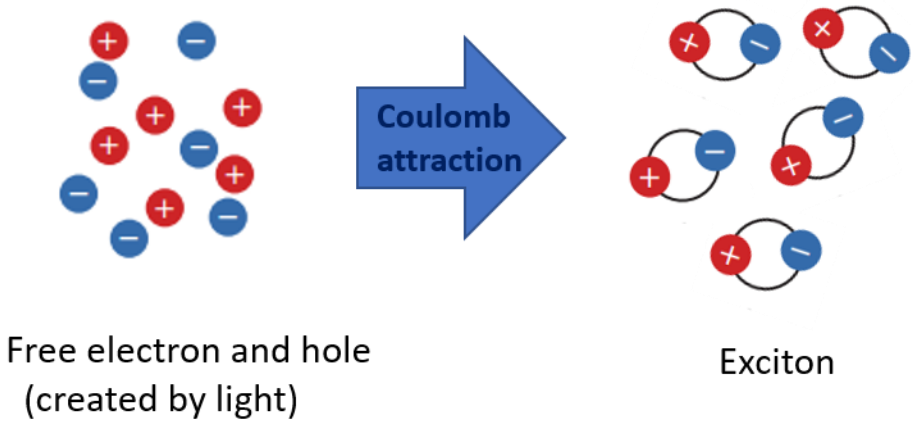

Figure 2.5: Exciton formation after photoexcitation.

While excitons clearly provide a rich platform for physics and devices, they are traditionally difficult to utilize. In typical bulk semiconductor crystals such as silicon, the large dielectric screening and small quasiparticle effective mass result in small exciton binding energies, only ~1-10s of meV. Thus, the bound behavior of the exciton is insignificant compared to the thermal fluctuations unless cooled down to low temperatures. In contrast, the bound exciton states often dictate the optical properties of low-dimensional materials such as monolayer transition metal dichalcogenides (TMDCs). The strong Coulomb interaction in low-dimensions and reduced dielectric screening compared to bulk crystals, naturally makes the excitons bound even at room temperature with several hundred meV binding energy [22](Fig. 2.6). In addition, the TMDCs' electronic "valleys" host the excitons and give rise to selection rules for the excitation and emission of light. These two-dimensionally confined excitons exhibit an extremely large binding energy and have their own selection rules.

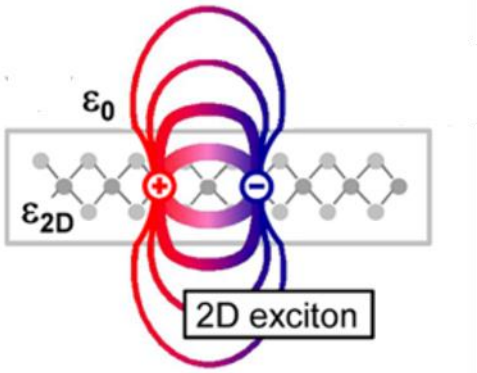

Figure 2.6: Giant excitonic effect in 2D materials with weak dielectric screening.

As the excitons are hydrogen-like, bound electron-holes in a Coulombic potential, they will form an excitonic series of higher energy states. In TMDCs, each excitonic state has a specific parity that the incident photons can excite. For these crystals where dipole-allowed interband transitions, one-photon states can only excite even parity excitonic states (termed "bright" excitons) and two-photon excitation can only excite odd parity states ("dark" excitons). These two-photon states do not appear in the linear one photon absorption. Therefore, it is possible to use the two-photon absorption and subsequent bright-state luminescence (two-photon luminescence, TPL) to determine the excitonic structure of TMDCs. Similar to the hydrogen atom, an exciton confined in a 2D plane also possesses an excitonic angular momentum (EAM) resulting from the orbital motion of the electron relative to the hole.

However, there has been little study of how the unique valley degree of freedom combined with the strong excitonic effect influences the nonlinear optical excitation. In the following, the discovery of nonlinear optical selection rules in monolayer WS_2 is presented [55], which is an important candidate for visible 2D optoelectronics because of its high quantum yield and large direct bandgap. I experimentally demonstrated this principle for second-harmonic generation and two-photon luminescence (TPL). Moreover, the circularly polarized TPL and the study of its dynamics evince a sub-ps interexciton relaxation (2*p* to 1*s*). The discovery of this new optical selection rule in a valleytronic 2D system not only considerably enhances knowledge in this area but also establishes a foundation for the control of optical transitions that will be crucial for valley optoelectronic device applications such as 2D valley-polarized THz sources with 2*p*–1*s* transitions, optical switches, and coherent control for quantum computing.

2.3 Importance of second harmonic generation and two-photon absorption

Typically, when laser irradiance is sufficiently intense, nonlinear optical response to the strength of the applied optical field can occur as a consequence of the modification of the optical properties of a material system. Since the first laser demonstration by Maiman in 1960, nonlinear optics has developed into an important subject of modern research. In this section, I would briefly overview two important nonlinear optical processes, which are two main approaches in my valleytronics study. One is second harmonic generation, the other is two-photon absorption.

In nonlinear optics, the optical response can often be described by expressing the polarization $\tilde{P}(t)$ as a power series in the field strength $\tilde{E}(t)$ as [10]

$$\begin{aligned}\tilde{P}(t) &= \varepsilon_0[\chi^{(1)}\tilde{E}(t) + \chi^{(2)}(\tilde{E}(t))^2 + \chi^{(3)}\big(\tilde{E}(t)\big)^3 + \cdots] \\ &= P^{(1)}(t) + P^{(2)}(t) + P^{(3)}(t) + \cdots . \end{aligned} \tag{2.1}$$

Here, $\chi^{(1)}$ refers to linear optical susceptibility, $\chi^{(2)}$ and $\chi^{(3)}$ are second-order, third-order nonlinear susceptibilities, respectively.

The optical second-harmonic generation (SHG) is the nonlinear frequency doubling process, which belongs to the generation of nonlinear polarization $P^{(2)}(t)$. Since its discovery in 1961, numerous applications based on SHG technique have been developed, including those in microscopic techniques [67].

One key feature for SHG process it that for it must vanish in centrosymmetric materials, which preserve inversion symmetry. This can be simply derivate it based on equation 2.1. Given the nonlinear polarization $P^{(2)}(t) = \varepsilon_0\chi^{(2)}(\tilde{E}(t))^2$ and the applied field is $E(t) = E_0\cos(\omega t)$. If inversion operation is applied, then the sign of both the applied electric field $\tilde{E}(t)$ and the induced polarization $P^{(2)}(t)$ must be changed. However, if the system has inversion symmetry, the intrinsic optical susceptibility should be unchanged under inversion operation. This leads to

$$P^{(2)}(t) = \varepsilon_0\chi^{(2)}(\tilde{E}(t))^2 \tag{2.2}$$

$$-P^{(2)}(t) = \varepsilon_0\chi^{(2)}(-\tilde{E}(t))^2 \tag{2.3}$$

In order to satisfy above relationships, the second-order susceptibility must be zero. Such feature makes SHG a very sensitive and non-destructive method for study on crystal symmetry, grain boundaries[68], piezoelectric and ferroelectric materials [69], which has advantages over transmission electron microscopy and atomic-force microscopy (AFM) based techniques due to the simplicity of sample preparation.

In contrast, two-photon absorption is another nonlinear optical process in all materials. The unique part is that this process allows the transition between states with same parity rather than parity change in one-photon process. In details, two-photon absorption involves two steps. In the first step an electron is raised into a virtual state by absorption of a photon of frequency ω_1 ; in the second it transfers into the final state with absorption of a second photon of frequency ω_2 (ω_2 can be equal to ω_1, if same laser source is used for TPA). For two-photon processes, distinct selection rules apply than that for one-photon processes. Briefly speaking, for a one-photon transition, the selection rule which applies is that the quantum number I, representing for parity, must change by ± 1. Two-

photon transitions are made up of two one-photon transitions. The selection rules are then $\Delta I = 0$ or $\Delta I = 2$. Therefore, transitions which cannot be observed in the normal absorption spectrum can thus be measured by two-photon absorption, which is quite useful to probe excitonic fine structures in semiconductors and molecules [70].

2.4 Generalized valley exciton optical selection rule

The three-fold rotational symmetry in monolayer WS_2 requires total angular momentum conservation during light–matter interactions, in which the VAM, EAM, lattice angular momentum, and photon spin angular momentum are exchanged with each other. Induced by the local atomic orbital angular momentum and nontrivial Berry curvature distribution, the VAM has an out-of-plane component in both the conduction ($\tau\hbar = 1\hbar$ or $-1\hbar$ at K′ or K valleys, respectively) and valence ($\tau\hbar = 0\hbar$ at K′ or K valleys) bands. Meanwhile, the relative electron–hole motion is confined to a 2D plane, resulting in an exciton wavefunction in the form of $R_{n,l}(\rho)e^{il\varphi}$ with only an out-of-plane $l\hbar$ EAM, where φ is the azimuthal angle and ρ is the electron–hole distance [71], [72]. The out-of-plane VAM and EAM are combined collinearly. In addition, the crystal transforms the impinging angular momentum into a modulus of three by absorbing the excess angular momentum into the lattice, in a manner similar to the Umklapp process in phonon scattering [73], [74]. As a result, under normally incident light, the conservation of out-of-plane angular momentum yields the following optical selection rule for the unique VAM and EAM in monolayer WS_2:

$$\Delta m\hbar = \Delta\tau\hbar + \Delta l\hbar + 3N\hbar \tag{2.4}$$

Upon absorption of incident light, the spin angular momentum of the photons, $\Delta m\hbar$, changes the angular momentum of the electrons in the valley ($\Delta\tau\hbar$, where τ=+1 (–1) for the –K (+K) valley), the angular momentum of the excitons with quantum number l ($\Delta l\hbar$), and the change in the angular momentum of the crystal lattice ($3N\hbar$, resulting from the symmetry of the crystal). Although strong spin-orbit coupling is present, the spin of the electron does not flip under the dominant electric dipole transition. Therefore, the unchanged out-of-plane spin angular momentum makes no contribution to equation (2.4). One can easily verify that the one-photon excitations ($m = \pm1$ for $\sigma_\pm$ light) to the 1_s excitonic level (l=0) simply yields the excitation of the K (–K) valley with σ_- (σ_+) light.

As for two-photon process, both the TPL and SHG processes exhibit a valley-exciton locked selection rule as described by equation (2.4), meaning that excitonic resonant two-photon processes occur only within specific valleys under pure circular polarization excitation (Fig. 2.7). For example, the resonant 1*s* second harmonic generation (SHG) is where two-photons are pumped at the energy of the 1*s* exciton level. If there is a resultant σ_- emission, from the K valley ($\Delta\tau\hbar = -\hbar$), with an exciton angular momentum as $0\hbar$ (as this is the 1*s* state), this can only occur when:

$$2(+1)\hbar = -1\hbar + 0\hbar + 3(1)\hbar \tag{2.5}$$

Indicating this requires the absorption of two photons with σ_+ emission to be able to generate a σ_- emission at the K valley. This is due to the fact that SHG is a virtual process, and the SH photon produced is from the virtual exciton at the 1*s* level. Therefore, the SHG emission is always of the opposite circular polarization than the two incident photons (Fig. 2.7a).

As for the TPL process, a similar example can be made. If the excitation is resonant with the 2*p* state with an excitation of σ+ then:

$$2(+1)\hbar = +1\hbar + 1\hbar + 3(0)\hbar \tag{2.6}$$

It can be seen that the TPL process therefore does not involve the crystal lattice contribution and therefore the TPL process has the same polarization compared to the excitation polarization (Fig. 2.7b).

Elucidating the selection rules for linear and nonlinear optical processes allows for the full prediction and control of the valley excitations in these TMDC crystals and has potential to enable valleytronic devices based on photon polarizations. In the following, experimental demonstrations of such nonlinear valley exciton selection rules are shown.

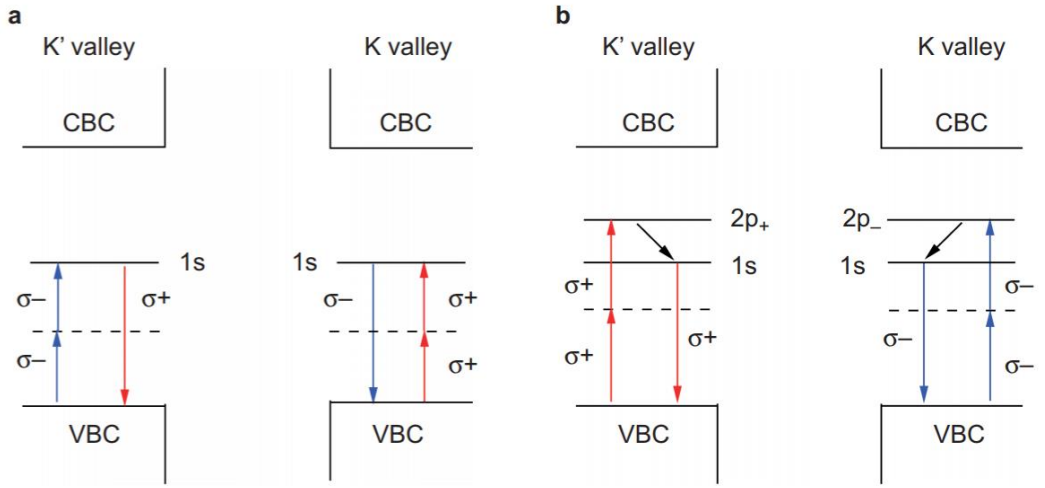

Figure 2.7: Schematics of optical selection rules based on valley-exciton locking. **a,** 1*s* exciton-resonant SHG in K′ (or +K) and K (or -K) valleys. Pumped by a σ_+ (or σ_-) polarized fundamental photon, an electron in the valence band at a K (or K′) valley reaches a virtual state. Within the lifetime of the virtual state, a second σ_+ (or σ_-) photon pumps the electron from the virtual state to the real 1*s* state in the K (or K′) valley. Immediately, a second-harmonic photon with a σ_- (or σ_+) polarization is emitted. **b,** 2*p* exciton-resonant TPL in K′ and K valleys. Under two-photon excitation by σ_+ (or σ_-) polarized photons, the system transitions from the ground state to the real $2p_+$ (or $2p_-$) state with a change of $+1\hbar$ (or $-1\hbar$) in the EAM at a K′ (or K) valley through an intermediate virtual state. The 2*p* exciton relaxes to the 1sexcitonic state and emits a σ_+ (or σ_-) photon. The conduction band continuum and valence band continuum are labeled as CBC and VBC, respectively. The solid lines represent real

excitonic states, and the dashed lines represent virtual states. Red indicates σ_+ polarization; blue indicates σ_- polarization.

2.5 Sample preparation, experimental setup and basic characterization

Monolayer WS_2 samples were mechanically exfoliated onto 275 nm SiO_2/Si substrates from chemical vapor transport synthetic crystal flakes (2D Semiconductors Inc., Scottsdale, USA). The exfoliated monolayers were typically 5–10 micrometers in size and were characterized using tools such as atomic force microscopy and Raman and photoluminescence spectroscopy (Fig. 2.8).

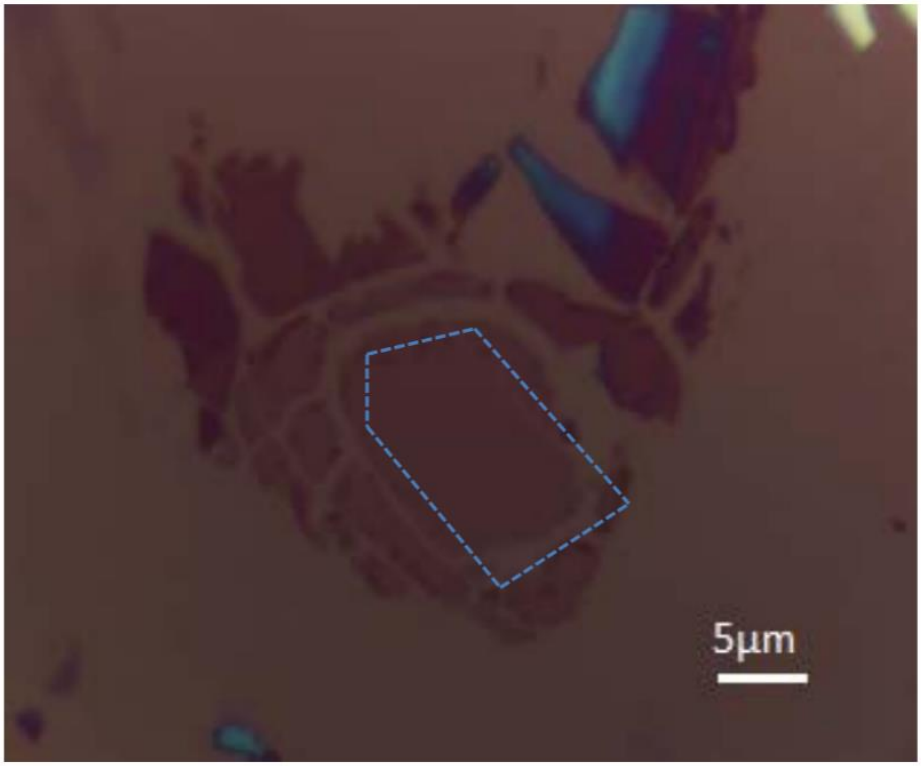

Figure 2.8: Typical exfoliated monolayer WS_2 flakes.

The excitation light was extracted using an optical parametric oscillator (Inspire HF 100, Spectra Physics, Santa Clara, USA) pumped by a mode-locked Ti:sapphire oscillator. The laser pulse width was approximately 200 fs, and the repetition rate was 80 MHz. The excitation laser was linearly polarized by a 900–1300 nm polarizing beamsplitter. The transmitted *p*-polarized laser light was converted into circularly polarized light via a broadband Fresnel Rhomb quarter-wave retarder. The low-temperature experiment was performed in a continuous-flow liquid helium cryostat equipped with a 50x objective with a long working distance. The emission signal was detected in the backscattering

configuration, analyzed using the Fresnel Rhomb quarter-wave retarder followed by a visible-range polarizer, and finally collected by a cooled CCD spectrometer. For time-resolved one-photon and two-photon photoluminescence spectroscopy, the signal passing through a bandpass filter with a bandwidth of 30 meV was collected by a Hamamatsu synchroscan streak camera with an overall time resolution of 2 ps. The transmissivity of the optical system was carefully calibrated to evaluate the absolute power level at the focusing plane. The emission spectra were normalized to the square of the focused power, as the excitation was limited to the unsaturated regime. The laser pulse width was measured using a home-built autocorrelator at the focus throughout the scanning range.

A typical light emission spectrum under excitation at 1090 nm (1.14 eV) and 20 K by an ultrafast laser is shown in figure 2.9. One emission peak, at 2.28 eV, is assigned to SHG. The other two peaks observed at 2.09 eV and 2.05 eV correspond to the neutral and charged exciton emissions. The charged exciton emission is dominant and was selected as our TPL signal. These excitonic emitted photon energies are nearly two times higher than that of the excitation photon, and therefore, they can originate only from twophoton absorption. This conclusion is further confirmed in the inset to figure 2.9. Both the TPL and the SHG exhibit a quadratic power dependence, indicating their two-photon nature.

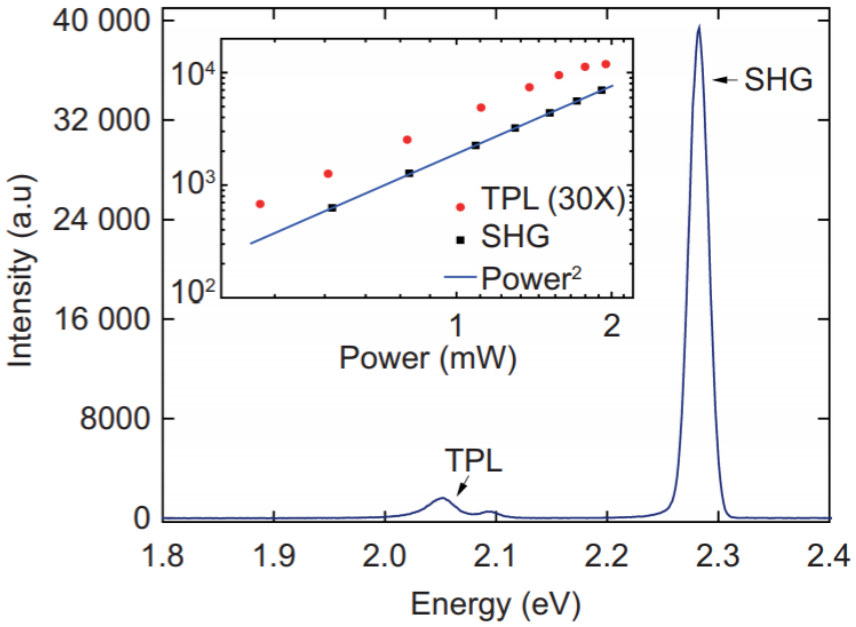

Figure 2.9: Typical emission spectrum of monolayer WS_2. The sample is pumped by a 1.14 eV laser pulse at 20 K. The peaks at 2.09 eV and 2.05 eV correspond to the 1*s* state of "A" neutral exciton and corresponding charged exciton (trion) created *via* TPL. The inversion symmetry breaking in monolayer WS_2 results in an SHG signal at 2.28 eV. In the inset, the power dependences of the TPL and SHG emissions are plotted, exhibiting quadratic behavior.

2.6 Valley exciton selection rule in nonlinear optical process: SHG and TPL

According to equation (2.5), SHG emissions carry the opposite helicity from that of the incident light, whereas TPL emissions display the same helicity. We first experimentally examined the optical selection rule for SHG. An excitation energy scan of the SHG signal revealed a resonance at 2.09 eV (Fig. 2.10a), indicating exciton-enhanced SHG due to the 1s state. The magnitude of the SHG signal at the 1*s* resonance is enhanced by nearly one order of magnitude compared with that under non-resonant excitation. We then measured the SHG under σ_+ excitation at the 1*s* resonance (Fig. 2.10b). The SHG helicity, defined as $\frac{I_{\sigma_+} - I_{\sigma_-}}{I_{\sigma_+} + I_{\sigma_-}} \times 100\%$, was found to be -99% at an excitation energy of 1.045 eV. The negative sign here indicates that the SHG has the opposite circular polarization from that of the fundamental light. Determined by the selection rule, such a high helicity value is preserved because SHG is an instantaneous process and free of any intervalley scattering processes. The observations of nearly 100% negative helicity and intensity resonance in SHG are well consistent with the proposed valley-exciton locked selection rule.

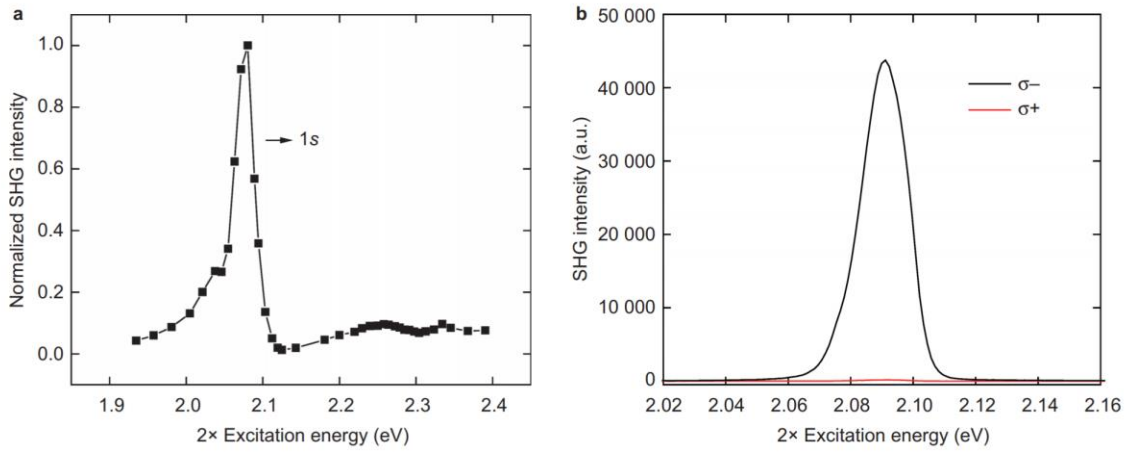

Figure 2.10: Experimental observation of the SHG selection rule in monolayer WS_2. **a**, SHG intensity (black dots) versus SHG excitation energy in a scan from 0.97 eV to 1.19 eV. A dominant SHG intensity peak is observed at a pump energy of 1.045 eV, which is attributable to the 1*s* resonance. **b**, Polarization-resolved SHG measurements for σ+ (red curve) and σ− (black curve) detection under pumping by σ+. A negative helicity of $P = -99.0\% \pm 0.1\%$ was observed from multiple repeated measurements. The excitation energy was 1.045 eV. The significant negative helicity at the 1*s* resonance confirms the existence of a rigorous selection rule for SHG. The measurement was done at 20 K

In contrast to the SHG selection rule at the 1*s* resonance, TPL displays a completely opposite valley-dependent selection rule at the 2*p* resonance. In an excitation energy scan (Fig. 2.10a), a dominant resonance was observed at 1.13 eV, corresponding to the 2*p* excitonic peak. Compared with the 1s excitonic level, the 2*p* exciton has a greater linewidth (80meV) and an asymmetric shape. To test the selection rule, we measured the TPL spectrum under σ_+ light excitation (Fig. 2.10b). The TPL helicity was measured to be 29.6% at the excitation energy (1.13 eV) and had the same sign as that of the incident light. The helicity changed sign when the monolayer was pumped with σ_- light. More interestingly, we observed a TPL resonance in the emission helicity at the 2*p* peak (Fig. 2.10b inset), confirming our theory that the EAM imposes an additional selection rule on the optical transition. The relatively low helicity value observed here is due to the strong intervalley scattering upon the injection of such high energies [75]. Away from the 2*p* resonance peak, we always observed nonzero TPL with lower energy excitation, as shown in figure 2.10a, indicating the presence of several non-excitonic states with *p* components below the 2*p* state. This background cannot originate from the re-absorption of the SHG emission because the emission helicity is positive.

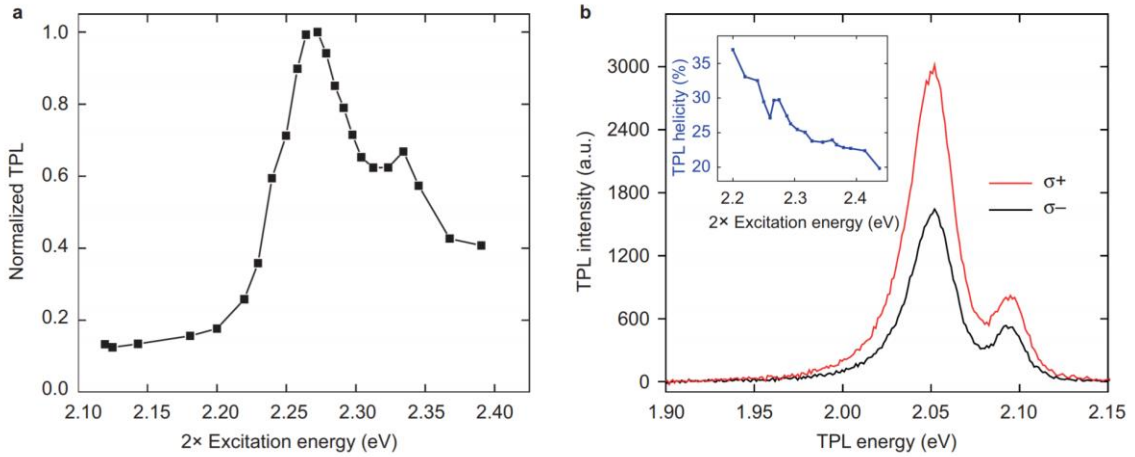

Figure 2.11: Experimental observation of the TPL selection rule in monolayer WS_2. **a**, TPL intensity versus TPL excitation energy in a scan from 1.06 eV to 1.19 eV. A dominant TPL intensity peak resonance is observed under 1.13 eV laser pulse excitation, which is attributable to the 2*p* resonance. **b**, Polarization-resolved TPL measurements for σ_+ (red curve) and σ_- (black curve) detection under σ+ light excitation. A circular polarization of P = 29.6% ± 0.5% was observed based on multiple repeated measurements. The excitation energy was 1.13 eV. The inset plots the TPL helicity versus the TPL excitation energy for a scan of the same range under excitation by σ+ polarized light. A helicity resonance is observed at the 2*p* excitonic level. Away from the 2*p* resonance, the TPL helicity decreases with increasing excitation energy due to the energy-dependent intervalley scattering. The measurement was done at 20 K.

2.7 Valley exciton and interexciton dynamics

Subsequently, we further examined the valley-exciton locked selection rule by performing time-resolved TPL measurements. After the initial two-photon absorption and the formation of 2*p* valley excitons, two subsequent processes occur: the 2*p* excitons relax to 1*s* excitons, and these 1*s* excitons recombine. If the populations in the K(or -K) and K'(or +K) valleys are unbalanced, intervalley scattering will occur (Fig. 2.12).

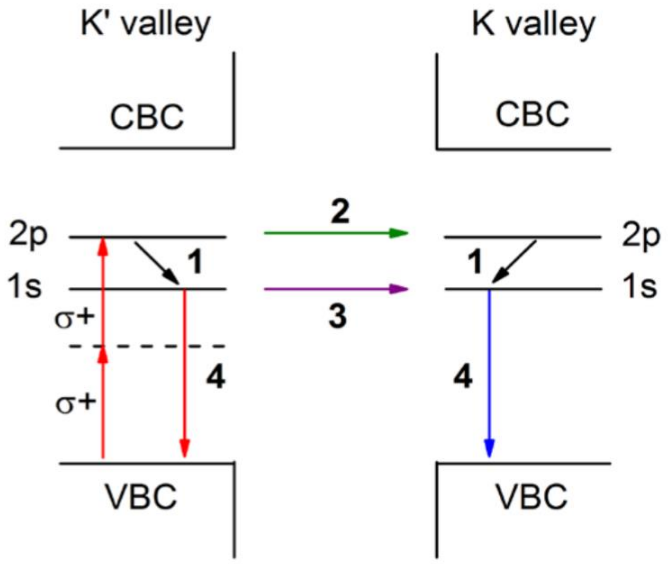

Figure 2.12: Schematic representation of valley exciton dynamics. With initial 2*p* exciton pumping at K' valley, the 2*p* exciton can either relax to 1*s* excitonic level (process "1") or be scattered to K valley during relaxation (process "2"). In the following, population of 1*s* exciton in both valleys decays mainly due to nonradiative recombination (process "4"). Meanwhile the intervalley scattering at 1*s* excitonic level further tends to balance the exciton population in K and K' valleys (process "3").

Here, we conducted time-resolved TPL measurements at the 2*p* resonance, and the signal was detected by a synchroscan streak camera with an overall time resolution of 2 ps. Under linearly polarized excitation light, the intervalley scattering has no net contribution because the populations in both types of valleys are equal. Therefore, the time-resolved TPL trace includes only relaxation and recombination (Fig. 2.13a). The rising edge after excitation is predominantly associated with the relaxation process from 2*p* to 1*s*, whereas the recombination process is reflected by the decaying portion of the curve. To capture the essence of the dynamics, we used a three-level rate equation based on the valley exciton population dynamics schematics, shown in figure 2.12. Since no excitons are created in higher states in this experiment, we can write simple rate equations only for the

1*s* and 2*p* exciton states. Here, 2*p* exciton cannot couple to light field to directly return to ground state and we assume 2*p* can only decay to 1s exciton without other decay channels. Since there is an energy splitting between 2*p* and 1*s* states, in principle, there can be two rates: $\frac{1}{\tau_{2p\to1s}}$ for 2*p* to 1*s* decay and $\frac{1}{\tau_{1s\to2p}}$ for 1*s* converts to 2*p*. However, due to Boltzmanian occupation factor, $\frac{1}{\tau_{1s\to2p}} = e^{-(E_{2p}-E_{1s})/k_BT}\frac{1}{\tau_{2p\to1s}}$, the rate for 1*s* exciton to convert to 2*p* is 4 orders smaller than 2*p* decay to 1*s*. Therefore, we only consider $\frac{1}{\tau_{2p\to1s}}$ in the following model. In polarization resolved analysis, we consider intervalley scattering both in 2*p*-1*s* relaxation and 1s recombination. The rate equation for the 2*p* and 1*s* exciton populations at the K and K' valleys after laser pulse excitation can be written as

$$\frac{dn_{2p,K'}}{dt} = -\frac{n_{2p,K'}}{\tau_{2p-1s}} - \frac{(n_{2p,K'}-n_{2p,K})}{\tau_{inter(2p-1s)}} \tag{2.7}$$

$$\frac{dn_{2p,K}}{dt} = -\frac{n_{2p,K}}{\tau_{2p-1s}} + \frac{(n_{2p,K'}-n_{2p,K})}{\tau_{inter(2p-1s)}} \tag{2.8}$$

$$\frac{dn_{1s,K'}}{dt} = +\frac{n_{2p,K'}}{\tau_{2p-1s}} - \frac{n_{1s,K'}}{\tau_{rec}} - \frac{(n_{1s,K'}-n_{1s,K})}{\tau_{inter(1s)}} \tag{2.9}$$

$$\frac{dn_{1s,K}}{dt} = +\frac{n_{2p,K}}{\tau_{2p-1s}} - \frac{n_{1s,K}}{\tau_{rec}} + \frac{(n_{1s,K'}-n_{1s,K})}{\tau_{inter(1s)}} \tag{2.10}$$

Here $\tau_{2p-1s}^{-1}, \tau_{inter(2p-1s)}^{-1}, \tau_{inter(1s)}^{-1}, \tau_{rec}^{-1}$ are the 2*p*→1*s* relaxation rate, the intervalley scattering rate during relaxation, the intervalley scattering rate of 1*s* exciton and nonradiative recombination rate. The radiative rate is ignored because of low quantum yield (~1%) in our sample. With linear polarization excitation, populations in K and K' valleys are equal and only relaxation and recombination are considered. By solving the equation with initial condition: $n_{2p,K'}(t=0) + n_{2p,K}(t=0) = n_0$, $n_{1s,K'}(t=0) + n_{1s,K}(t=0) = 0$, the time function of total 1*s* exciton population is

$$n_{1s}(t) = n_{1s,K'}(t) + n_{1s,K}(t) \sim (e^{-\frac{t}{\tau_{rec}}} - e^{-\frac{t}{\tau_{2p-1s}}}) \tag{2.11}$$

Under circular polarization excitation, the time function of net 1*s* exciton valley population is

$$n_{1s,K'}(t) - n_{1s,K}(t) \sim (e^{-\frac{t}{\tau_{rec}}-\frac{2t}{\tau_{inter(1s)}}} - e^{-\frac{t}{\tau_{2p-1s}}-\frac{2t}{\tau_{inter(2p-1s)}}}) \tag{2.12}$$

To extract above lifetimes, we convolute expressions in (2.11) and (2.12) with IRF and then fit the measured time resolved TPL trace with lifetime parameters.

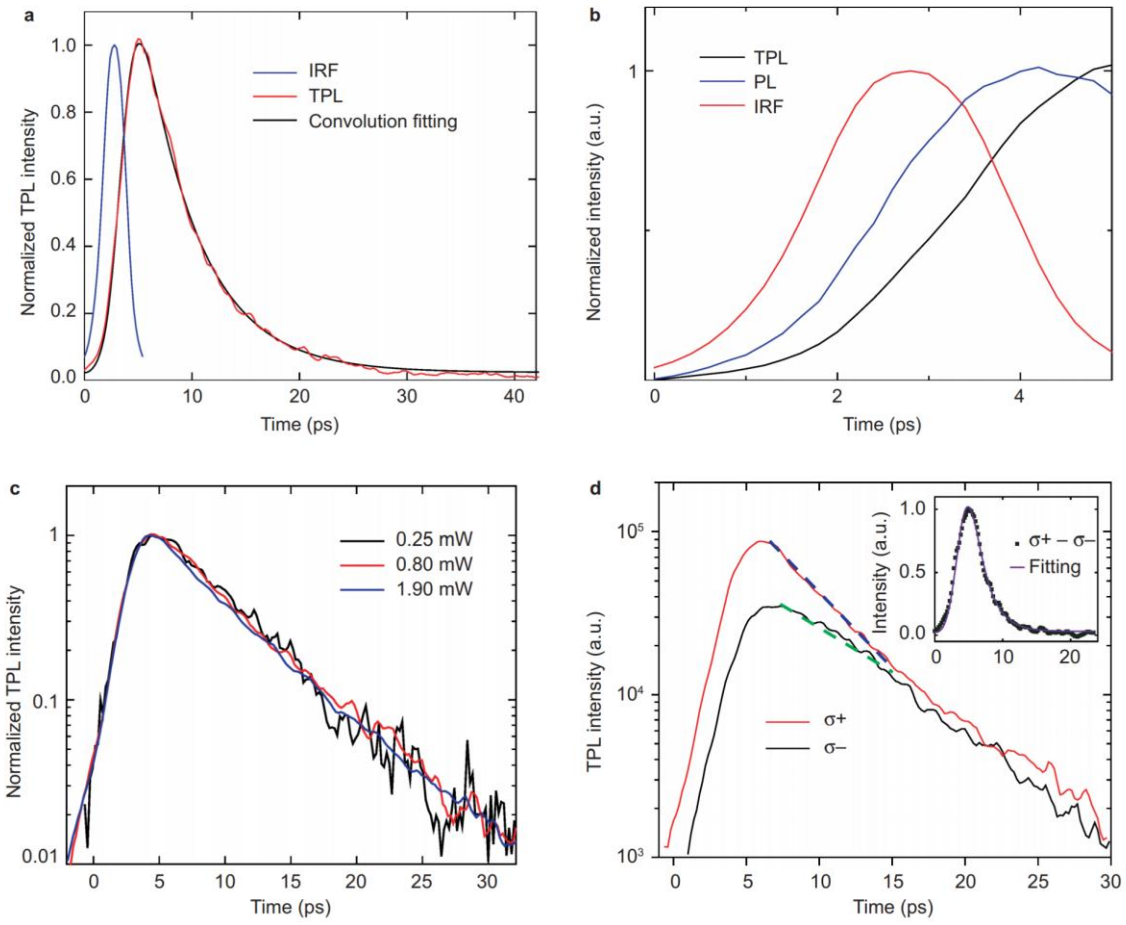

Figure 2.13: Time-resolved valley exciton dynamics in monolayer WS_2 at 20 K. **a**, Time trace of the TPL (red curve) excited by a linearly polarized laser pulse at 1.13 eV. Compared with the instrument response function (IRF), presented as the blue curve, the TPL time trace exhibits observable rising and decaying features. Based on our three-level rate equation model, the results of convolution fitting (black curve) indicate an interexciton relaxation time τ_{2p-1s} of 600 ± 150 fs and a recombination time τ_{rec} of 5.0 ± 0.2 ps. **b**, Relaxation dynamics comparison. The time-resolved relaxation curves (rising features) for two-photon-induced PL (TPL, black curve) and one-photon-induced PL (blue curve) are plotted. The one-photon-induced PL, excited near the resonance at 2.10 eV, exhibits a sharper rising feature compared with that of the TPL excited at the 2*p* resonance (2.26 eV). This difference confirms that the relaxation of the 2*p* exciton requires a longer time because of the larger energy gap. Here, the red curve represents the IRF. **c**, Power-dependent time-resolved 2*p* resonant TPL. TPL time traces recorded under pumping by a laser pulse at 1.13 eV with different incident powers. The power was varied over one order of magnitude, resulting in a change in the exciton population of two orders of magnitude. No significant change in the dynamics is observed in this power range, thereby excluding exciton–exciton annihilation. **d**, Polarization-resolved time traces of the TPL excited by σ_+ polarized light at 1.13 eV. Because of the selection rule and intervalley scattering, the σ_+

emission (red curve) displays a greater intensity and more rapid decay than does the σ_- emission (black curve). The blue and green dashed lines are guides for the eye. The inset shows the convolution fit (purple curve) for the time-resolved valley exciton population ($\sigma_+ - \sigma_-$, black dots). The intervalley scattering times during relaxation, $\tau_{\text{inter}(2p-1s)}$, and recombination, $\tau_{\text{inter}(1s)}$, are estimated to be 3 ± 1 ps and 8.3 ± 0.5 ps. The error ranges were obtained from fitting to the results of multiple repeated measurements. PL, photoluminescence.

Typically, a process no shorter than one tenth of the system's time resolution can be extracted by applying convolution fitting with the instrument response function (IRF) [76]. In this manner, we can infer that the interexciton relaxation time is τ_{2p-1s} = 600 ± 150 fs and that the recombination time is τ_{rec} = 5.0 ± 0.2 ps. Regarding the sub-ps 2*p*–1*s* relaxation, which is reported here in 2D TMDC for the first time, it was further verified by time-resolved PL measurements under near-resonance one-photon excitation (Fig. 13b). The rising feature in this curve is much sharper compared with that under 2*p* resonant two-photon excitation, which indicates more rapid relaxation because of a smaller energy gap. Indeed, our fit shows that the relaxation time to the 1*s* exciton edge in this case is less than 200 fs (the fastest process can be extracted from convolution fitting). This confirms our observation of a measurable sub-ps 2*p*–1*s* relaxation due to the large energy gap between the 2*p* and 1*s* excitonic levels. Excited carrier relaxation can typically follow three possible pathways: carrier–carrier scattering, carrier–phonon scattering, and radiative emission. Carrier–carrier scattering is predominantly dependent on carrier density. However, as we varied the pump intensity, no significant change in the dynamics was observed (Fig. 13c). Therefore, carrier–carrier scattering is unlikely to account for the sub-ps relaxation here. Meanwhile, radiative emission from the 2*p*–1*s* transition can be excluded because the transition rate is not expected to be as fast as the sub-ps level. Given the comparable densities of states and transition matrix amplitudes calculated using the GW method [22], [72], one should expect the 2*p*–1*s* transition time to be similar to the 1s exciton radiative lifetime. Because the radiative lifetime of the 1s exciton is approximately 100 ps in our case (the quantum yield is 5%, and the lifetime of the nonradiative decay is 5 ps, as shown in Fig. 13a), the sub-ps relaxation we observed cannot be radiative decay. Therefore, it is very likely to be attributable to exciton–phonon scattering. This is further confirmed by the broader linewidth of the 2*p* exciton. Under the assumption that the 2p–1s relaxation is accomplished via optical phonon cascade scattering, each phonon scattering event requires around 130 fs (the energy gap between the 2*p* and 1s levels is 220 meV, and the dominant optical phonons observed via Raman spectroscopy have energies of 44 meV for the E_{2g} mode and 51 meV for the A_{1g} mode). According to the uncertainty principle, this corresponds to an additional linewidth broadening of greater than 30 meV. compared with the 1s exciton. This is consistent with our observation, which indicates 40 meV of additional broadening. It is suspected that a 1s hot exciton with some kinetic energy is generated after a 2*p* exciton collides with a phonon and cascades to the 1s exciton edge. The rapid recombination observed at the 1*s* exciton edge (τ_{rec} = 5.0 ± 0.2 ps) is likely attributable to nonradiative recombination, such as defect trapping or a phonon-assisted process [77]. This is confirmed by the quantum yield measurement [36], which indicates a quantum yield of approximately 5%.

We carefully checked that the nonradiative channel is not dependent on the excitation power (Fig. 2.13c), which excludes any exciton–exciton annihilation mechanism [78]. For σ_+ two-photon excitation at the 2*p* resonance, the dynamical curves for emission at the different polarizations are shown in figure 2.13d. The σ_+ TPL from the K' valleys exhibits a higher intensity than that of the s2 TPL from the K valleys, which again confirms the valley-exciton locked selection rule. Compared with σ_+ emission, the σ_- emission always undergoes slower decay until the populations in the two types of valleys are equal. This difference in the decay trend results from intervalley scattering, which tends to equalize the exciton populations in the two valleys. From convolution fitting with the IRF and recombination time, we can estimate the lifetimes of intervalley scattering during relaxation, $\tau_{inter(2p-1s)}$, and recombination, $\tau_{inter(1s)}$, to be 3 ± 1 ps and 8.3 ± 0.5 ps, respectively (Fig. 2.13d inset). The exchange interaction between the electron and hole can induce both a spin flip and a momentum change via Coulomb potential scattering. Recent calculations show that this process can occur in the picosecond range and becomes more efficient when the exciton carries more energy [79], which may account for the rapid depolarization observed in our measurements.

2.8 Conclusion and perspectives

In summary, we discovered nonlinear optical selection rules based on valley-exciton locking in monolayer WS_2, an important 2D material with direct bandgap in visible regime. This important finding reveals that the EAM and VAM combined fundamentally determine the nonlinear optical transitions in TMDC monolayers. These new selection rules together with the observed interexciton dynamics offer important guidance for the manipulation of exciton and valley degrees of freedom in 2D TMDC. For example, the well-defined excitonic levels located in distinguishable valleys could encode quantum information. Quantum coherent control utilized excitonic 2*p*, 1*s* and ground state can be designed. Similar to such control demonstrated in atom systems, two channels to access 1*s* excitonic level are established coherently. One is through directly pump ground level with photon energy resonant with 1*s* excitonic level, while the other is through TPA to access 2*p* state first. Then an additional IR drive field, with photon energy resonant with 2*p*-1*s* energy difference, is applied to control 1*s* excitonic population by coherent interference with the first channel. Such scheme provides unique ultrafast optical modulation of 2D valley excitons population and phase, which is the essential step towards valleytronics. Our finding also potentially leads to the design of THz sources with 2*p*–1*s* transitions, optical switches and quantum interference control based on this 2D material [80]–[82].

3 Electrical generation and manipulation of valley carriers in monolayer WS_2

In previous chapter, I discussed generalized optical selection rule for nonlinear optical process in 2D TMDCs with the presence of both valley degree of freedom and excitonic fine structure. Such finding together with previous optical circular dichroism works pave the way for optical generation and manipulation in valleytronics. However, for device scaling and integration purpose, electrical control of valleytronics is in urgent need. In this chapter, I would introduce our work on electrical generation and manipulation of valley carriers in monolayer WS_2 [56].

3.1 Introduction to valley carrier generation for future valleytronics

Currently, manipulation of electronic charge and spin for information processing is widely applied. It is now expected that such valley degree of freedom can be used to encode and process information, which leads to conceptual applications known as valleytronics. A typical valleytronic material system should have at least two degenerate but inequivalent valleys (local energy extrema) in momentum space that can be manipulate to encode, process and store information.

There are several unique parts for valleytronics compared with current electronics and spintronics technology. First, pure valley current can flow without net charge current, the Ohmic loss can be reduced and heat dissipation can be further reduced if intervalley scattering by phonon is not significant. Second, valley degree of freedom as a discrete index can be used for quantum information process. Third, such quantum index is quite robust and can exist as long as the crystal structure unchanged. Fourth, unlike conventional spintronics which utilize binary electron spin states, the valley degree of freedom is determined by crystal structure and electron orbitals. In principle, a system can have more than two valley indices. With multiple valley indices, multiple information channels can be established and boost the information transmission/processing speed. Finally, unlike spintronic applications, valleytronic platform does not necessarily require the presence of local magnetic field. With all above advantages, it is quite appealing for fulfillment of valleytronics.

In the emerging monolayer transition metal dichalcogenides (TMDs), the electronic properties at the band edge are dominated by the two inequivalent valleys that occur at the +K (or K') and −K (or K) points at the edges of the Brillouin zone. The electrons in the +K valley can be labelled as valley-pseudospin up, and the electrons in the −K valley can be labelled as valley-pseudospin down. Carriers in +K and −K valleys are subject to opposite Berry curvatures. A valley magnetic moment also arises from the orbital angular momentum contributed by both local atomic orbitals and interatomic phase winding. Composite quasiparticles like excitons are also associated with the valley degree of freedom. The unique part of these excitons is that valley pseudospin associated can be optically excited and read by circularly polarized light [25]. In other words, researchers

discovered a valley-dependent optical selection rule that right circularly polarized light excites exciton in the +K valley, while left circularly polarized light create exciton in the −K valley. This selection rule has been widely proved in various monolayer TMDs. It is very important for the early development of this field because researchers can simply apply circularly polarized light to preferentially inject excitons into one valley, generating a difference in the population of the two valley excitons.

On the other hand, electrically controlling the flow of charge carriers is the foundation for modern electronics. To realize valleytronic applications, it is necessary to electrically control the valley DOF, which remains the critical challenge to date. In the following, experimentally demonstration of electrically valley generation and control based on unique spin-valley locking relationship will be shown [83]. Valley polarization is achieved through spin injection via a diluted ferromagnetic semiconductor and measured by the electroluminescence helicity using the unique spin-valley locking in TMDC monolayers. Such a direct electrical generation and control of valley carriers opens up new dimensions in utilizing both spin and valley for next-generation electronics and computing.

3.2 Spin-valley locking relationship in monolayer TMDC

The inversion symmetry breaking together with spin-orbit coupling leads to coupled spin and valley physics in TMDC monolayers, which allows access to the charge carrier's valley DOF via spin injection. The TMDC monolayer possesses direct energy gaps located at the nonequivalent K and K' valleys in the reciprocal space. At these valleys, the *d* orbitals of heavy transition metal ion accompany with strong spin-orbit interaction introduce a large energy split in the valence bands. For example, the split can be up to ~ 440 meV in a tungsten disulfide monolayer [22], [24]. The spin projection S_z along the c-axis of the monolayer crystal is well defined and the two split bands are of spin up and spin down. Meantime, the preserved time-reversal symmetry enforces the opposite spin splitting at the two distinct valleys, which leads to so-called spin-valley locking relationship (Fig. 3.1). The unique locking relationship and the large valence band splitting are expected to strongly suppresses the spin and valley scattering, leading to a long valley-spin lifetime in TMDC monolayers [25]. This is because that the intra-valley scattering is unlikely due to the large valence-band edge splitting, while intervalley scattering involves a simultaneous spin flip, which is suppressed due to the large momentum mismatch. In the presence of such relationship, the goal to achieve electrical valley generation can be fulfilled by electrical spin injection.

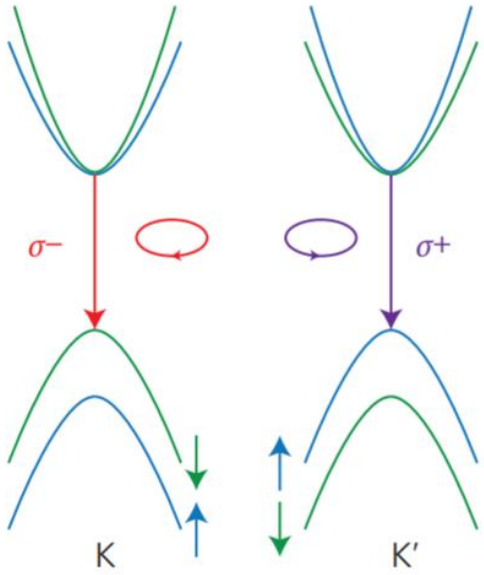

Figure 3.1: Electronic structure at the K and K' valleys of monolayer WS_2. K and K' represent the two distinct momentum valleys in the reciprocal space of a TMDC monolayer. The spin degeneracy at the valence band edges is lifted by spin–orbit interactions. Electrical excitation and confinement of the carriers in one set of the two non-equivalent valleys are achieved through the manipulation of the injected carrier spin polarizations, due to the spin–valley locking in monolayer TMDCs. Optical selection rules give rise to opposite circularly polarized light emissions at different excited valleys.

3.3 Design and working principle of electrical valley injection

Electrical spin injection refers to injection of spin-polarized carrier electrically from one material into the other in contact. Typically, the source is a magnetic metal or semiconductor while the drain or acceptor can be nonmagnetic materials.

The injection efficiency is substantially influenced by the interfacial scattering, intrinsic resistance mismatch and spin polarization anisotropy alignment [84]. Because monolayer WS_2 is semiconductor and the direction of valley-locked hole spin is along out-of-plane direction. It is suitable to have semiconducting spin injection source with out-of-plane easy axis. Following this criteria, p-type (Ga,Mn)As thin film is chosen as ferromagnetic contact. Firstly, as a semiconductor, (Ga,Mn)As can effectively reduce resistance mismatch and enhance spin injection efficiency [85]. Secondly, the magnetic anisotropy of (Ga,Mn)As can be controlled by strain. With suitable strain control, high quality (Ga,Mn)As thin film with out-of-plane magnetization can be grown [86].

The ferromagnetic (Ga, Mn)As semiconductor naturally serves as a spin aligner and allows spin-polarized hole injection. The Curie temperature and coercivity at 5 K of (Ga, Mn)As film with an effective Mn concentration of 5.9 % are about 150 K and 200 Oe.

The in-plane tensile strained (Ga, Mn)As film is perpendicularly magnetized (Fig 3.2).

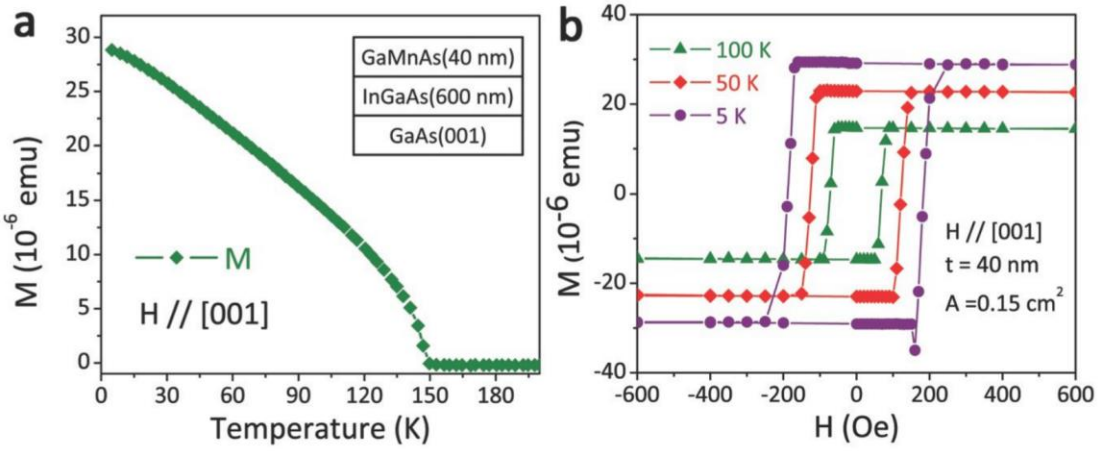

Figure 3.2: Magnetism characteristics measured by SQUID magnetometer. a, Temperature dependence of the remnant magnetization measured along the [001] direction, indicating the T_C of 150 K. b, Magnetic hysteresis loops measured at different temperature with magnetic field perpendicular to the sample surface, implying that the magnetic easy axis is perpendicular to the sample surface in the whole temperature range under T_C.

By applying an external magnetic field, we polarize the injected holes from (Ga, Mn)As film that match in one of these two distinct valleys (K and K'). The physical process for electrical valley generation in our device is elaborated below: Firstly, under a certain bias, spin polarized hole carriers are injected from p-type (Ga,Mn)As ferromagnetic electrode into monolayer WS_2. The spin orientation is determined by magnetization direction of (Ga,Mn)As, which can be controlled by external magnetic field. After spin-polarized hole carriers are injected into monolayer WS_2, they tend to occupy a specific valley due to spin-valley locking relationship. Because of n-type semiconducting WS_2 and valley dependent optical selection rule, circularly polarized electroluminescence emits at the heterojunction between the p-type (Ga, Mn)As and the n-type monolayer WS_2 at forward bias. The helicity of this signal reflects the unbalanced spin injected carrier population at K and K' valleys, which can infer valley injection efficiency with some dynamic constants. In other words, the momentum of the populated valleys is uniquely determined by the spin polarization of the injected holes. Subsequently, the electroluminescence from the heterojunctions is therefore expected to be valley-polarized, governed by the injected spin polarization due to the unique spin-valley locking (Fig.3.3).

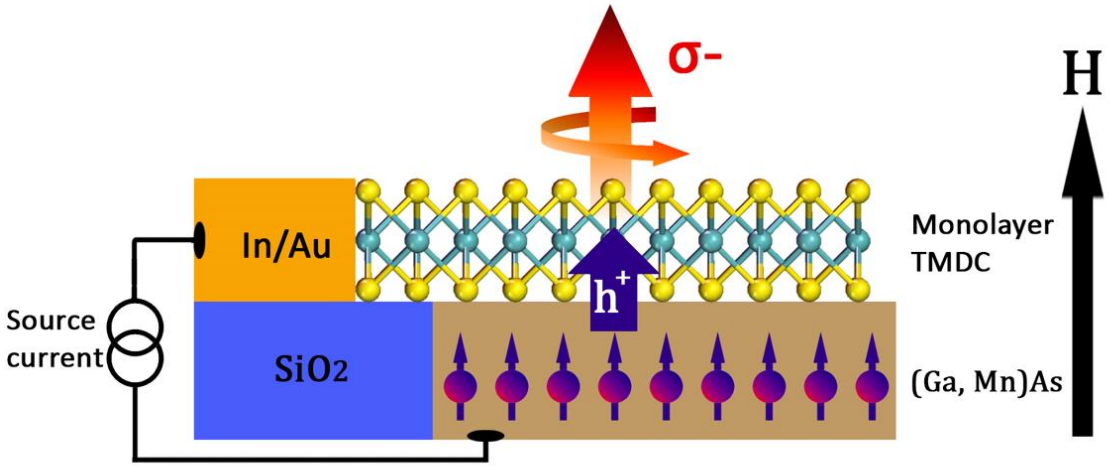

Figure 3.3: Schematic of the monolayer TMDC/(Ga,Mn)As heterojunction. (Ga,Mn)As was used as a spin aligner under an external magnetic field. The valley polarization can be directly determined from the helicity of the emitted electroluminescence as a result of the recombination between the electrically injected spin-polarized holes and the selected degenerate electrons in TMDC monolayers.

3.4 Sample preparation and basic characterization

The (Ga, Mn)As is lithographically defined into a mesa shape, and an exfoliated WS_2 monolayer is mechanically transferred to the edge of the mesa. To prevent substrate leakages, a thin film of SiO_2 is deposited and patterned to provide good electric isolation between the monolayer and the substrate. An In/Au (10/80 nm) electrode is then introduced to form an ohmic contact on monolayer WS_2. A site-specific dry transfer technique was applied to precise allocate the exfoliated monolayer WS_2 with a clean interface between the monolayer and the ferromagnetic semiconductor (Fig. 3.4). When a forward bias is applied on the (Ga, Mn)As, with the In/Au electrode grounded, the injection of holes from (Ga, Mn)As across the junction gives rise to efficient radiative recombination due to the direct band-gap of monolayer WS_2. The corresponding electroluminescence has been used as a reliable way to study optical transitions in monolayer TMDCs [87]–[89]. The electrical valley polarization can be directly determined from the helicity of the emitted electroluminescence as a result of the valley-resolved recombination between the electrically injected spin-polarized holes and the selected unpolarized electrons in monolayer TMDC due to preservation of valley-dependent selection rules.

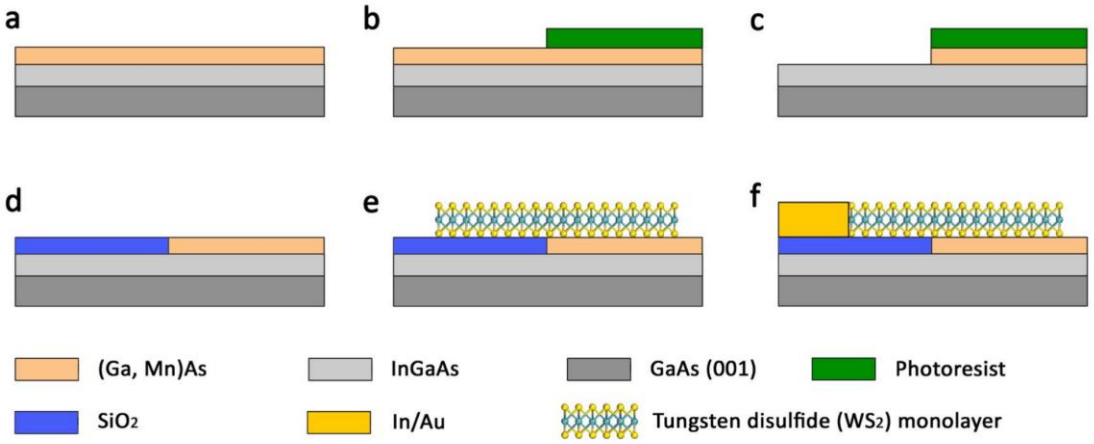

Figure 3.4: Device fabrication. **a,** MBE growth of perpendicularly magnetized (Ga, Mn)As film on InGaAs buffer layer. **b,** UV lithographically patterned photoresist on (Ga, Mn)As. **c,** Wet etching (Ga, Mn)As film by solution of H_3PO_4:H_2O_2:H_2O=1:1:38 with a etching rate about 2 nm/s. **d,** Electrical isolation thin film SiO2 defined by a electron-beam evaporation deposition and followed by a lift-off process. **e,** A site specific dry transfer method used to place the monolayer WS_2 onto the interface between SiO_2 and (Ga, Mn)As films. **f,** Ohmic contact (In/Au) of monolayer WS_2 defined by EBL, followed by thermal evaporation and lift-off processes, on the SiO_2 film.

A representative current-voltage characteristic of the heterojunction of n-WS_2/p-(Ga, Mn)As shows clear rectifying behavior for a bias voltage between –1.5 V to +1.5 V (Fig. 3.5a). The electroluminescence is localized at the edge of heterojunction (inset of Fig. 3.5a), as the largest voltage drop naturally occurs across the heterojunction. The devices were mounted in an optical cryostat where the electroluminescence is captured by a 50× (N.A.= 0.55) long working distance objective. When the injection current exceeds the rectifying threshold, strong electroluminescence resonance peaked at 1.97 eV (A exciton) is clearly observed (Fig. 3.5b). The electroluminescence intensity increases with the carrier injection rate, and the central emission wavelength and linewidth have a slight red shift and broadening, respectively, at a higher injection current due to Joule heating. No defect-related emission is observed, indicating the high quality of the monolayer WS_2. The electroluminescence spectra do not show a measurable B exciton complex in the monolayer WS_2/(Ga, Mn)As junction. The strong suppression of the B exciton emission in a WS_2/(Ga, Mn)As heterojunction, conducive to the electrical valley confinement, is a result of the large valence band splitting (~440 meV) of monolayer WS_2. The large valence band offset between monolayer WS_2 and (Ga, Mn)As causes the collapse of the electron barrier in the heterojunction, while the hole barrier height and injection capability remain unaffected under the large forward bias. Therefore, a band bending is expected in the quasi-neutral region, and the conduction is largely dominated by the series resistance of monolayer WS_2. The large valence splitting prevents the high-energy holes from populating the B exciton band, resulting in only the A exciton complex being observed in the electroluminescence spectra (Fig 3.5b). In contrast, the valence splitting

of monolayer MoS_2 and $MoSe_2$ are much smaller, approximately 160 meV and 180 meV [35], [90], which allows a certain population of the B exciton emissions in the monolayer MoS_2 and $MoSe_2$ based heterojunctions. Because A and B excitons possess opposite spin indices at different valleys (K and K'), the isolation of A and B excitons allows us to spectroscopically detect the valley population by observing the valley-polarized electroluminescence via manipulating the spin indices of charge carriers.

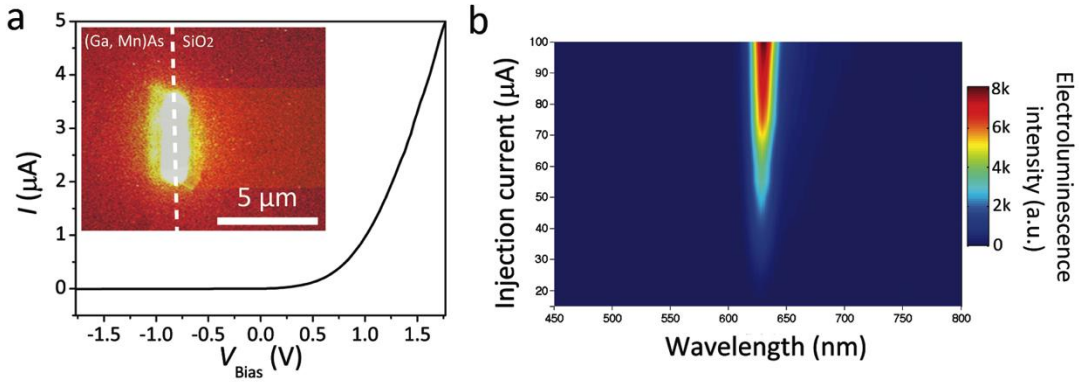

Figure 3.5: Electroluminescence of the monolayer WS2/(Ga,Mn)As heterojunctions. **a**, Electrical characteristics of the WS_2 diode, showing clear rectifying behaviour for bias voltage between −1.5 to +1.5 V. Inset: Surface plot of the electroluminescent emission overlaid with the scanning electron micrograph image at a forward bias of 5 V. The electroluminescence is localized at the edge of heterojunction. By applying an in-plane bias voltage, the largest voltage drop naturally occurs across the heterojunction edge due to the semiconducting characteristics of monolayer WS_2. The white dashed line indicates the interface between the SiO_2 and (Ga,Mn)As film. **b**, Electroluminescence intensity of the WS_2/(Ga,Mn)As heterojunction as a function of injection current and emission photon wavelength. The strong electroluminescence resonance peak at 1.97 eV (A exciton) is clearly observed and increases with the carrier injection rate. No B exciton and defect-related emission features are observed.

3.5 Electrical injection and manipulation of valley carrier

The degree of valley polarization from a heterojunction of a TMDC monolayer and ferromagnetic semiconductor is determined from the polarization helicity of the electroluminescence. A Helmholtz coil with a maximum magnetic field of 400 Oe normal to the sample surface was used to polarize the hole carriers in the ferromagnetic semiconductor. The injection of spin-polarized holes leads to the carrier population in a specific momentum valley due to the unique spin-valley locking in monolayer TMDCs, giving rise to circularly polarized light emissions. When injecting spin-up holes with magnetic field pointing outwardly towards the sample, the K valley is populated (inset of Fig. 3.6a), leading to right circularly polarized light emissions, and vice versa. Because the B excitonic feature in n-WS_2/p-(Ga, Mn)As heterojunction is substantially suppressed,

we focus on the A excitonic feature. Under an outward magnetic field perpendicular to the surface, we present the polarization-resolved electroluminescence spectra (σ− and σ+ components) of monolayer WS_2-based heterojunction at 15 μA (Fig. 3.6a). The electroluminescence helicity ρ,

$$\rho = (I_{\sigma-} - I_{\sigma+})/(I_{\sigma-} + I_{\sigma+}) \times 100\% \quad (3.1)$$

is found to be as large as 16.2% at the peak, indicating the strong valley polarization in monolayer WS_2/(Ga, Mn)As heterojunction as a result of spin-polarized hole injections. Here $I_{\sigma-}$ and $I_{\sigma+}$ are the energy-integrated intensities of the right and left circularly polarized electroluminescence, respectively. We observe a decrease in the electroluminescence helicity when increasing the injection current. Meanwhile, the local temperature increases due to the Joule heating at high injection current. Further studies are needed to clarify these issues. When an inward magnetic field is applied, an opposite electroluminescence helicity of $\rho = -14.8\%$ is observed as the reversed magnetic field allows injection of the opposite (spin-down) holes and population of the opposite valley, K' (Fig. 3.6b).

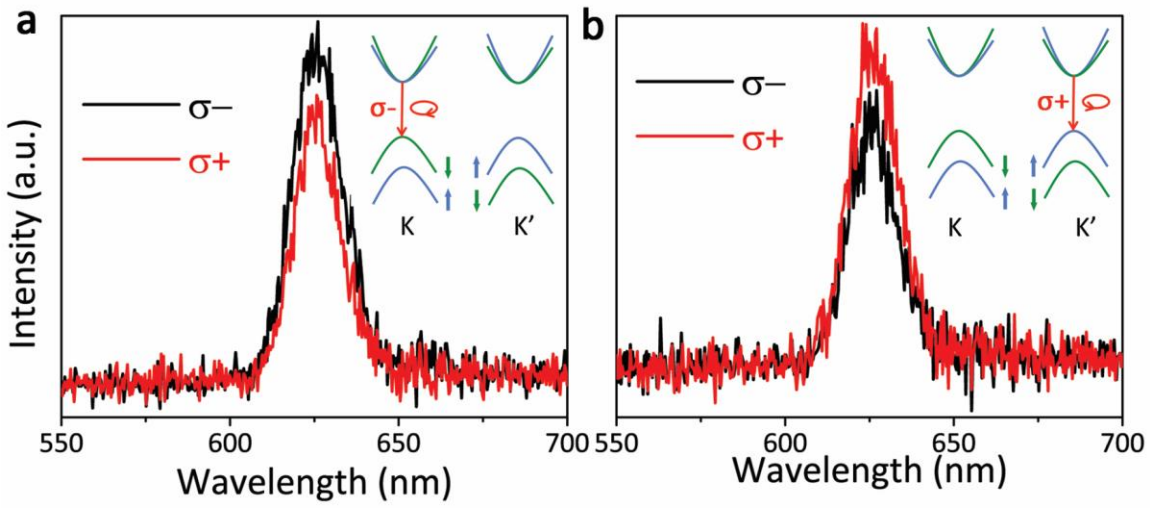

Figure 3.6: Electrical control of valley polarization in monolayer WS_2. Spectra of **a**, $\sigma-$ and $\sigma+$ resolved electroluminescence polarized under an outward magnetic field of 400 Oe perpendicular to the surface with a current of 15 μA. The electroluminescence helicity, $\rho = (I_{\sigma-} - I_{\sigma+})/(I_{\sigma-} + I_{\sigma+})$, is found to be as large as 16.2% at the peak, indicating strong valley polarization in the monolayer WS_2/(Ga,Mn)As heterojunction as a result of spin-polarized hole injections. Inset: Schematic representation of electrical excitation and emission processes. The K valley is populated by spin-up hole injection from spin-polarized (Ga,Mn)As due to spin–valley locking, resulting in σ_- light emission as a result of the optical selection rules. **b**, Spectra of σ_- and σ_+ resolved electroluminescence polarized under an inward magnetic field of 400 Oe perpendicular to the surface. An opposite electroluminescence helicity of $\rho = -14.8\%$ is observed.

Inset: schematic representation of electrical excitation and emission processes. The reversed magnetic field allows injection of the opposite (spin-down) holes and populating the inversed valley, K', resulting in σ_+ light emission.

The electrical generation of valley polarization is further confirmed by detailed magnetic field dependence of the electroluminescence helicity, which shows clear squared hysteresis (Fig. 3.7), agreeing with the SQUID magnetometer and anomalous Hall effect measurements. To confirm that the observed electroluminescence polarization is not due to magnetic circular dichroism (MCD) of the (Ga, Mn)As film or the Zeeman effect from the applied magnetic field, we performed polarization-resolved magneto photoluminescence of monolayer WS_2 on the (Ga, Mn)As film. Under a small magnetic field magnitude of 400 Oe, the circular polarization of the exciton photoluminescence is not dependent upon the magnetic field. The experimentally observed helicity of valley-polarized electroluminescence is limited by the efficiency of the spin-polarized carrier injection as well as the spin and valley scattering processes in the heterostructure. The major spin depolarization processes in the ferromagnetic semiconductor include the non-perfect spin polarization and the spin scattering during the electrical transport. In addition, the valley scattering and depolarization of electrically populated holes at non-zero temperature contribute to reduce the contrast of the valley population.

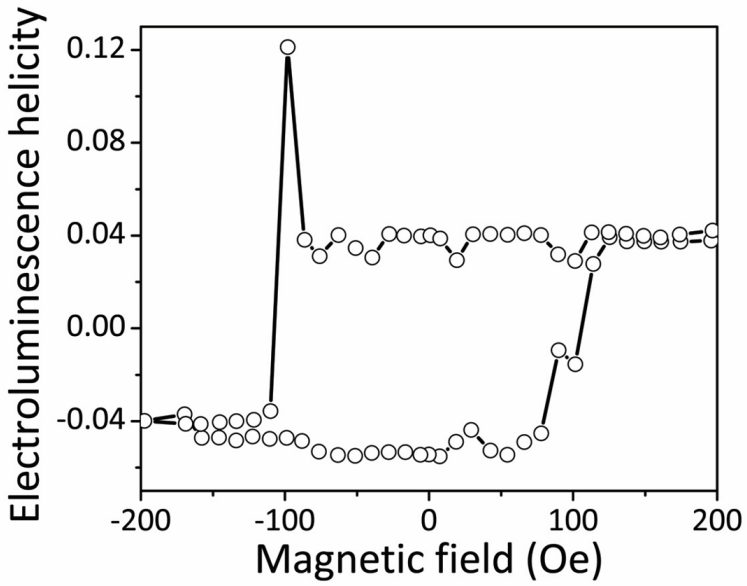

Figure 3.7: Out-of-plane magnetic field dependence of electroluminescence helicity. This measurement was done on a new device operated at 10 K with a current of 30 μA. The helicity of the electroluminescence has a hysteresis loop that agrees with the SQUID magnetometer and anomalous Hall effect measurement. The clear squared hysteresis of electroluminescence helicity confirms the electrical generation of valley polarization. Spin switching causes a zero-intensity difference in the σ_- and σ_+ light emission. As the lock-in amplifier cannot detect the signal, a large outlier occurs at −100 Oe.

3.6 Injected valley carrier dynamics and spin injection efficiency estimation

In order to accurately extract the electrical valley generation efficiency across the monolayer heterojunction, we examine the valley dynamics by time-resolved polarization measurements in monolayer WS_2 on (Ga, Mn)As, using a synchroscan streak camera. Figure 3.8a displays the total photoluminescence ($\sigma_- + \sigma_+$) intensity dynamics following a σ+ polarization from a femtosecond excitation laser pulse with an energy of 2.21 eV, tracing the exciton relaxation and recombination processes. Based on a two-level rate equation, we can infer an effective exciton lifetime (τ) of 2.5 ps (determined from two exciton lifetimes of 2.9 ps and 20.0 ps, from convolution fitting with the incident laser pulse). In addition, the time-resolved σ+ emission from the K' valley displays higher intensity than that of σ− emission from the K valley (Fig. 3.8b), confirming the valley-contrasting selection rule. Compared with the σ_+ emission, the σ_- emission always shows slower decay until populations in two valleys are equal. This difference between two decay trends results from inter-valley scattering, which tends to equalize the exciton populations in the two valleys. From convolution fitting with the incident laser pulse and recombination time as obtained above, we estimate the lifetime of inter-valley scattering (τ_K) to be 2.5 ps (inset of Fig. 3.8b). The valley dynamics do not change under a magnetic field from −400 to 400 Oe, which further confirms the valley polarization arises from the initial spin polarized injection from (Ga, Mn)As. According to rate model and the knowledge of valley carrier dynamics[91], we can estimate the initial electrically generated valley polarization ρ0. The degree of electroluminescence polarization ρ depends on the steady values of the valley exciton densities, N_K and $N_{K'}$ as

$$\rho = (N_K - N_{K'})/(N_K + N_{K'}) = \rho_0/(1 + 2\,\tau/\tau_K) \tag{3.2}$$

where τ is the exciton lifetime at both K and K' valley and $\tau_K^{-1}$is inter-valley scattering rate. Given the measured electroluminescence polarization of ~15%, a significant portion (~ 45%) of the overall valley generation efficiency remains intact across the monolayer heterojunction, consistent with previous studies using (Ga, Mn)As as spin aligner [92].

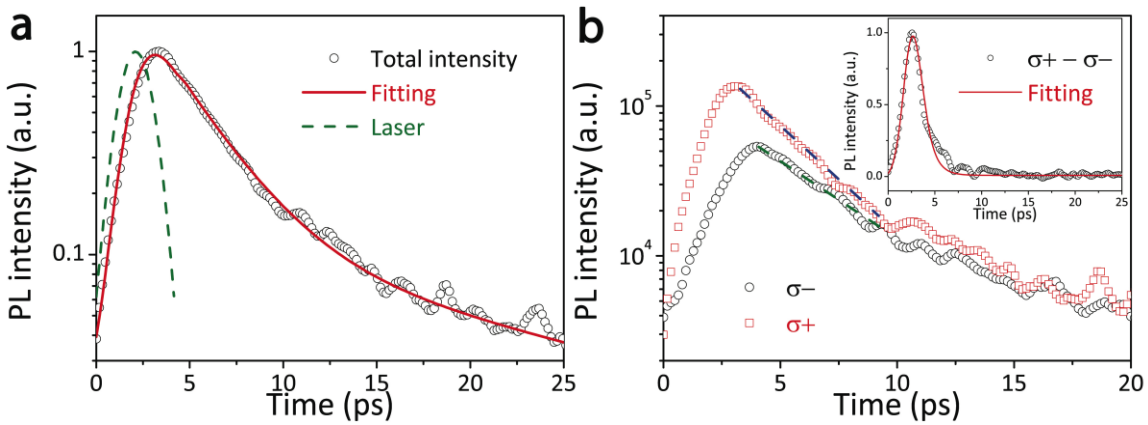

Figure 3.8: Valley dynamics measurement in monolayer WS_2 on (Ga,Mn)As. **a**, Time-resolved total photoluminescence using a σ_+ polarization femtosecond excitation laser pulse with an energy of 2.21 eV. Convolution fitting with the laser pulse (green dashed line), yields two exciton lifetimes of 2.9 ps and 20.0 ps. **b**, Time-resolved σ_+ and σ_- photoluminescence components excited by a σ_+ polarized laser. Blue and green lines indicate the different decay rates for these two components. Inset: Convolution fitting (red curve) for the time-resolved valley exciton population ($\sigma_+ - \sigma_-$, black circles). The intervalley scattering time is estimated to be 2.5 ps.

3.7 Conclusion and perspective

The electrical generation and control of valley population is at the heart of emerging valleytronics. We experimentally demonstrate the first electrical valley polarization with spin injection from a ferromagnetic semiconductor, which is confirmed through the observed valley-polarized light emission. The electrical control of the valley DOF opens the door towards a new paradigm of electronics that manifests all three DOFs: charge, spin and valley for information processing and computing.

In current work, external magnetic field and ferromagnetic electrode are in need to achieve electrical valley generation. Recently, researchers utilized strain to break monolayer crystal three-fold symmetry, which lead to nonzero magnetoelectric coefficient. With strain along specific orientation, the Berry curvature maximum will be no longer overlap with band extreme. By applying an in-plane bias (or current), valley magnetization can be generated [93]. This method does not require external magnetic field. However, external strain is in need and generation efficiency needs to be quantified. In the near future, high efficient electrical valley generation without external magnetic field is one of the most important research directions towards the practical application of valleytronics.

4 Out-of-plane dipole and ferroelectricity in 2D layered polar materials

In previous chapter, I mainly focused on unique valley degree of freedom in 2D TMDCs, whose properties are closely linked with crystal inversion symmetry breaking and three-fold rotation symmetry. I demonstrated generalized optical selection rule for nonlinear optical process in 2D TMDCs and electrical generation and manipulation of valley carriers in monolayer WS_2. In this chapter, I would discuss another crystal symmetry breaking, that is out-of-plane mirror symmetry breaking in 2D materials. Such symmetry breaking leads to 2D polar materials, a new class of crystal display appealing phenomena such as intrinsic Rashba spin splitting, out-of-plane dipole emission and ferroelectricity [57], [58].

4.1 Introduction to 2D layered polar material

A polar material possesses at least one polar axis along which two directional views are geometrically or physically different. A polar axis can occur only in non-centrosymmetric structures [94]. In polar crystal, it is not allowed for a mirror plane or twofold axis perpendicular to the polar axis, because they will make both directions of the axis equivalent. Such polar compounds are of great interest in material science and engineering because of their interesting physical properties, such as piezoelectricity, pyroelectricity, ferroelectricity, and especially second-order nonlinear optical (NLO) properties [95]. In addition, their polar property could enable polar electromagnetic force which is an important intergradient for chemical reactions, catalytic process and molecular self-assembly [96].

Compared with bulk, 2D polar crystals with reduced dimensionality are expected to be a fundamentally unique system to explore with distinct features such as enhanced many body interactions due to quantum confinement and weak dielectric screening. In addition, the interfacial physics is rich in heterostructures. Finally, large electrical and mechanical tunablity make 2D thin films very appealing for applications. For example, several percent strain can be applied in 2D thin films without breaking down which is about 1-2 orders higher threshold than that in bulk materials. Such high strain is comparable with the application of 1–10 GPa of pressure, which is equivalent that at a depth of 30–40 km below the surface of the Earth [95].

However, the limit of 2D thickness cannot be achieved easily in conventional polar crystals with dangling bond surface because structure reconstruction or chemical reaction tend to occur and remove out-of-plane dipoles [97]. For example, ZnO is a three-dimensional crystal which exists in four different forms: Wurtzite, Zinc blende, hexagonal boron-nitride and rock salt structures [98], [99]. Among them, only Wurtzite

and Zinc blende structures are inherently polar in bulk form. However, in ultrathin ZnO down to several nm, the tetrahedral configuration in either Wurtzite or Zinc blende leaves unpaired sp^3 bond at the terminal layer, which significantly lifts total energy and makes the thin film unstable [100]. Rock salt structure was only observed at a high pressure [101]. Meanwhile, theory and experiments have shown that only hexagonal boron-nitride structure with sp^2 trigonal coordination is thermodynamically stable at the monolayer limit [102], [103], which is non-polar in the out-of-plane direction (Fig. 4.1). Such surface instability, that is Tasker type III instability, also holds true for ionic out-of-plane polar materials, and forces the reconstruction of many traditional polar crystals such as ZnO into out-of-plane non-polar conguration at two-dimensional limit [97].

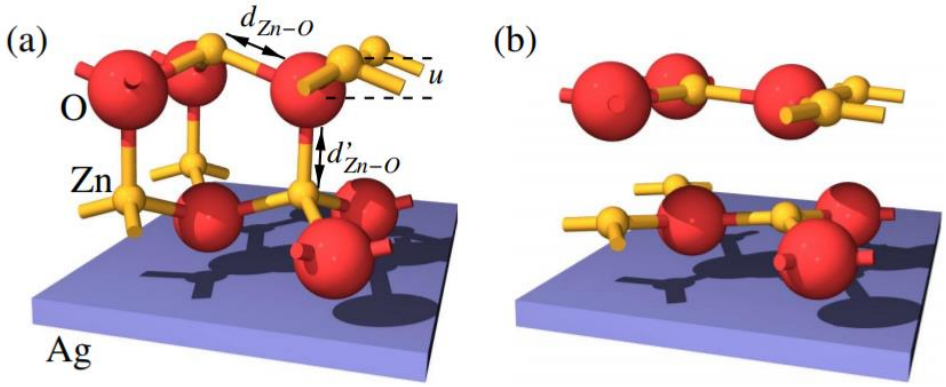

Figure 4.1: ZnO calculated stable structures in bulk and in ultrathin film forms. The bulk ZnO (wurtzite) structure **(a)** and the experimentally derived structure model for the first two monolayers **(b)**. Small and large balls represent Zn and O atoms, respectively. Reprinted with permission from ref. [104]. Copyright American Physical Society.

In contrast, 2D layered van der Waals materials such as monolayer MoS_2 are chemically stable and free of dangling bonds at its top and bottom surfaces. However, all available 2D layered materials are out-of-plane symmetric. To enable the vertical dipoles and piezoelectrics, out-of-plane symmetry has to be broken. In the following, the chapter firstly focuses on the creation and characterization of first monolayer polar crystal MoSSe [105]. In the second part, very recent discovery of 2D ferroelectricity in another polar layered material In_2Se_3 will be discussed. Such asymmetric ultrathin films provide unique opportunity to realize the ultrathin piezoelectric/ferroelectric material with intrinsic out-of-plane electromechanical coupling. Such systems have intrinsic Rashba spin splitting for spin transport [106], as well as unique Janus surfaces for asymmetric catalytical reactions [96].

4.2 Introduction to Janus monolayer MoSSe

The two-dimensional (2D) transition metal dichalcogenide (TMD) monolayer such as MoS_2 and WS_2 discussed in previous chapters have attracted significant attentions. The lack of inversion symmetry in a TMD monolayer results in distinguishable Berry curvatures at two sets of Brillouin zone edges, which leads to valley dependent optical selection rules for interband transitions. Meanwhile, the strong spin-orbit coupling (SOC), originated from the *d*-orbitals of the Mo or W atoms, makes it an interesting platform with coupled spin and valley physics. However, monolayer TMDCs exhibit the mirror symmetry (D_{3h}) and thus are non-polar perpendicular to the layer plane, which eliminate several important intrinsic properties in 2D layered materials. For instance, intrinsic Rashba splitting is absent, a phenomenon which allows to manipulate the spin by electric fields rather than using magnetic fields. Calculations have predicted that the mirror symmetry of polar MoSSe monolayer is broken (C_{3v}), leading to an out-of-plane dipole with appreciable Rashba splitting at the Γ point [107]. This type of polar TMD monolayers (with the formula MXY, where M = Mo or W and X, Y = S, Se or Te) possess interesting and rich physics and likely with many potential applications associated with its vertical dipoles. Unfortunately, such crystals do not exist in nature and hence a synthetic approach is required. Here, a strategy to synthesize the polar MoSSe monolayer is achieved. The MoSSe monolayer is stable and shows distinctly different electronic and phonon structures compared with MoS_2 or $MoSe_2$. Second harmonic generation (SHG) experiments further proves the presence of pronounced out-of-plane optical dipoles [57].

4.3 Creation and basic optical characterization of Janus monolayer MoSSe

Given monolayer MoSSe does not exist in nature, specific chemical synthesis is in need. The synthesis of a Janus MoSSe monolayer is illustrated in Fig. 4.2. To start, single crystalline triangular MoS_2 monolayers on c-plane sapphire substrates were prepared using chemical vapor deposition. Then by applying a remote hydrogen plasma, the top-layer sulfur atoms were stripped off and replaced with hydrogen atoms. The subsequent thermal selenization allows Se to replace H atoms, forming a structurally stable Janus MoSSe monolayer in which the Mo atoms are covalently bonded to underlying S and top-layer Se atoms.

The optical images for the monolayer at each stage are displayed, where the stripped MoS_2 (MoHS) remains its triangular shape. The atomic force microscope images reveal an apparent change in the cross-sectional height from 1.0 nm for pristine MoS_2 to 0.7-0.8 nm for MoHS and to 1.1 nm for Janus MoSSe. The reduced thickness after H_2-plasma indicates the success in S-stripping. It is found that the plasma power needs to be at optimum values such that we can break the surface Mo-S bonds but still preserve the underlying 2D Mo-S structure; in this respect, the remote plasma produced from light molecules works better than that from heavy molecules such as Ar plasma, which easily

destroys the whole 2D structures. The selenization temperature also plays a critical role. The substrate temperature needs to be higher than 350 °C for Mo-Se bond formation but not higher than 450 °C, in which the 2D structure becomes unstable and broken holes appears in the monolayer. When the temperature is higher than 600 °C randomized MoSSe alloy structures are obtained with fully random distribution of S and Se at the top and bottom of Mo atom plane, consistent with previous report [108].

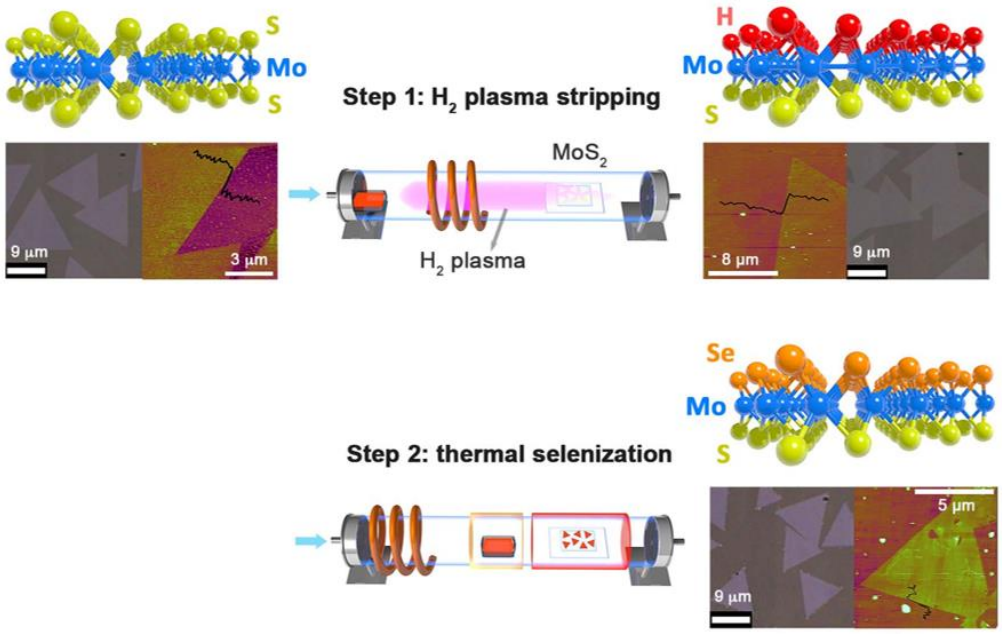

Figure 4.2: Synthesis of monolayer MoSSe. A MoS_2 monolayer grown by chemical vapor deposition was exposed to H_2 plasma to strip the top-layer S. The plasma was then switched off and a quartz boat loaded with Se powder was moved next to the sample without breaking the vacuum. Se powders were then thermally vaporized to achieve selenization and complete the synthesis of Janus MoSSe monolayers. Optical microscopy and atomic force microscopy images for each structure are shown below the corresponding molecular model.

Basic optical characterization such as Raman and photoluminescence measurements were conducted. Figure 4.3 shows that the characteristic Raman out-of-plane A_1 and in-plane E' modes for a MoS_2 monolayer appear at 406 and 387 cm^{-1} respectively. The intensity of A_1 and E' peaks decreases (curve 5 min stripping) and eventually vanishes (curve 20 min stripping) with the increasing stripping time. However, the A_1 and E' peaks appear again after sulfurization, indicating the recovery of MoS_2 monolayers from MoHS and the reversal ability of this process. On other hands, if the selenization is applied for MoSH, the A_1 peak shifts to 288 cm^{-1} from the original 406 cm^{-1}, and the E' peak shifts to 355

cm^{-1} from 387 cm^{-1}. These peaks match well with the two major phonon energies in phonon spectrum calculation for Janus MoSSe [57]. The shift of the A_1 frequency is caused by the out-of-plane symmetry change upon selenization, while the shift of the E′ mode is related to the lattice constant change. Figure 4.4 shows that the optical gap of a pristine MoS2 monolayer at 1.88 eV disappears after S-stripping, agreeing with the metallic property of the MoSH predicted by density functional theory (DFT) calculations. The photoluminescence (PL) for the MoSH samples recovers to that of MoS_2 after sulfurization, consistent with the observation in Raman. The optical gap for the Janus MoSSe monolayer is at 1.68 eV, close to the average of the optical gaps of MoS_2 and $MoSe_2$.

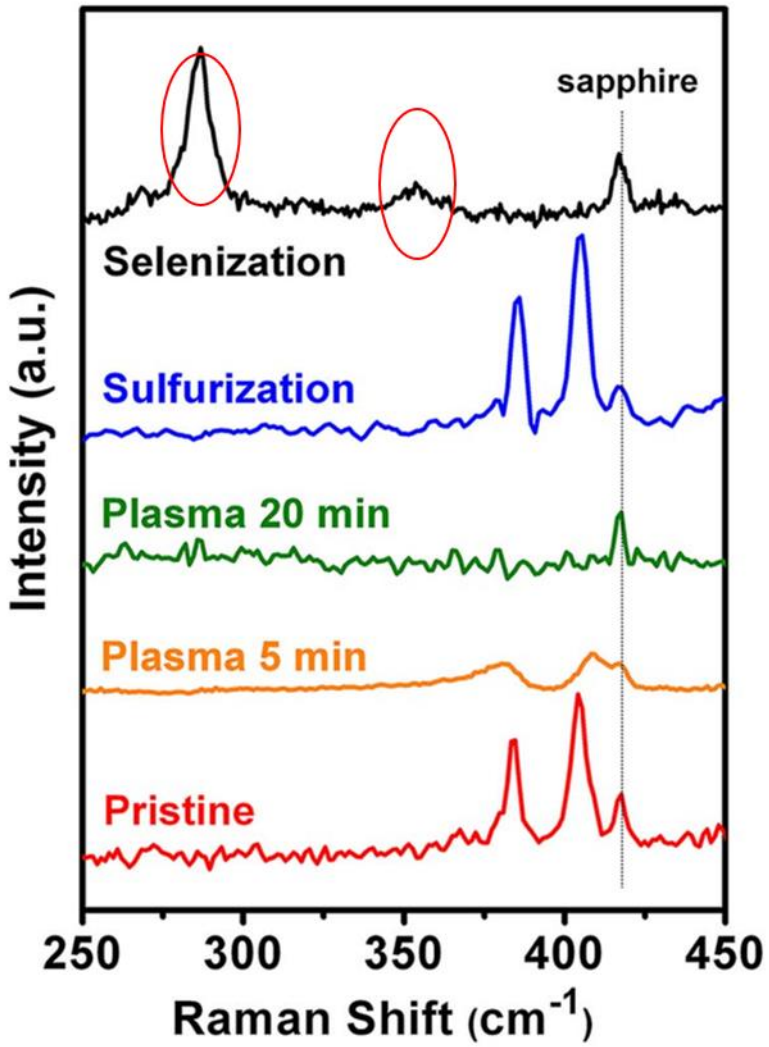

Figure 4.3: Raman characteristics at each synthesis step. It includes the MoS_2 and those after H_2 plasma treatment, sulfurization and selenization.

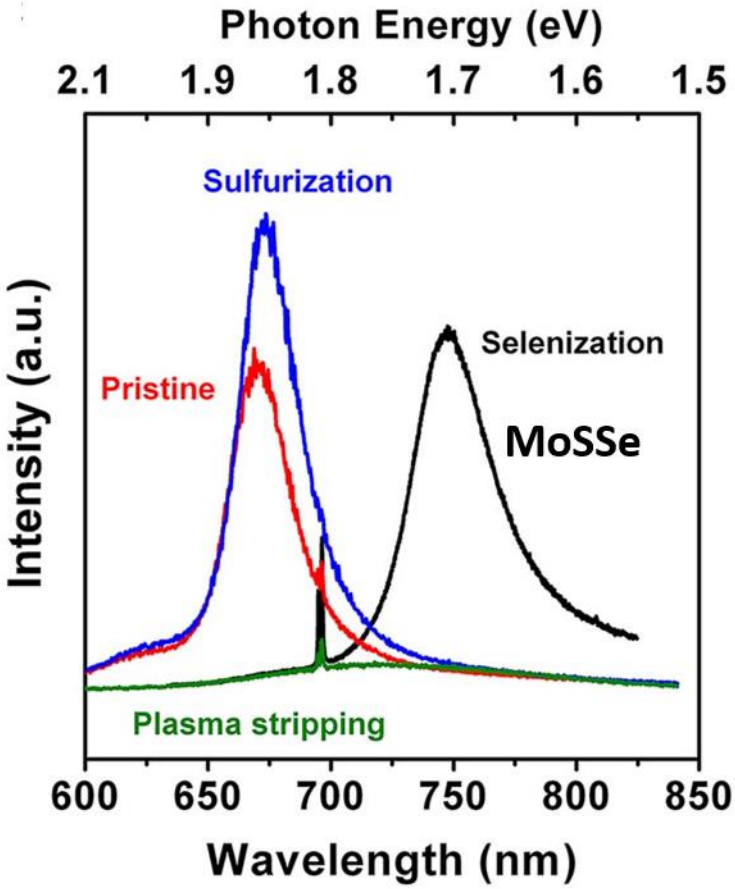

Figure 4.4: PL for synthetic product at each step. It includes the MoS_2 and those after H_2 plasma treatment, sulfurization and selenization.

More interestingly, valley emission is preserved in such Janus structure, as shown in Fig. 4.5. Also, figure 4.6 presents an annular dark-field scanning transmission electron microscopy image of a cross-section of the Janus MoSSe monolayer. Since the image contrast is proportional to the square of the atomic number, the bottom S and top Se atoms are clearly distinguishable, confirming the success of our proposed synthetic approach.

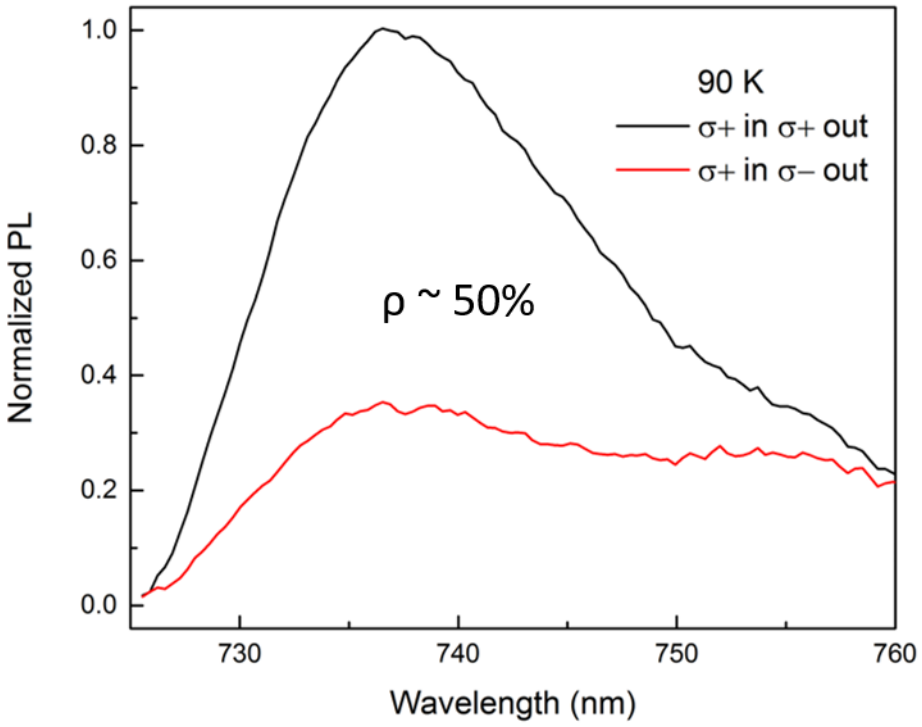

Figure 4.5: Valley PL emission from monolayer MoSSe.

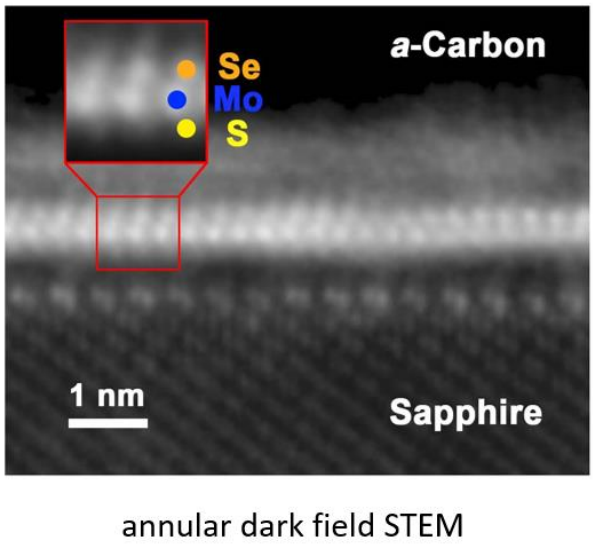

annular dark field STEM

Figure 4.6: Annular dark-field scanning TEM image of the sample cross-section. It shows the asymmetric MoSSe monolayer structure with Se (orange) on top and S (yellow) at the bottom of the Mo atoms (blue).

4.4 Discovery of vertical dipole of Janus monolayer MoSSe by SHG

The asymmetry of chemical bonding within monolayers can be revealed by optical second harmornic generation (SHG) [109]. In a polar crystal, the imbalance of electronic wavefunction results in asymmetry optical dipole transition. For ultrathin polar film with polar axis perpendicular to the film, angle resolved polarization selective SHG measurement can be performed to observe such influence (Fig. 4.7).

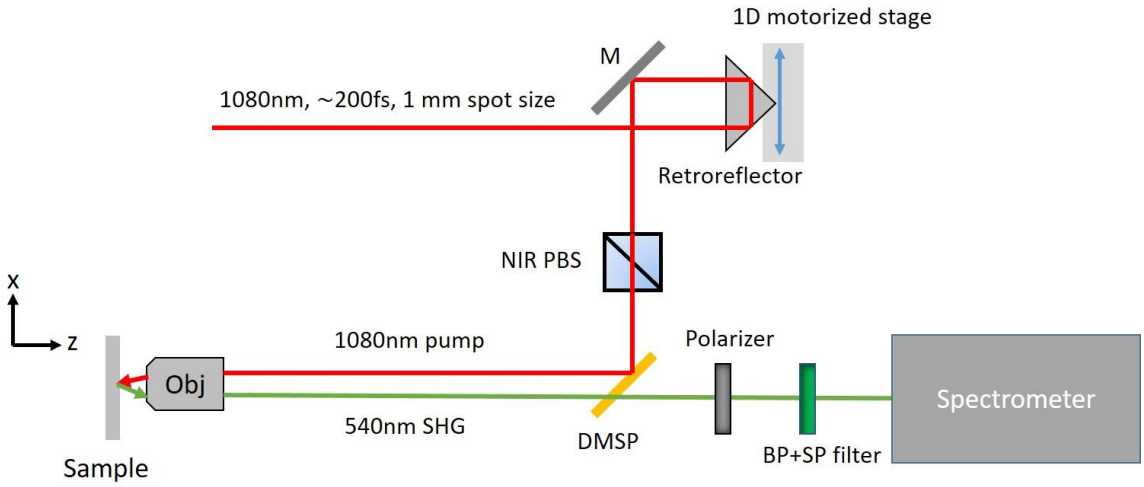

Figure 4.7: Angle-resolved polarization SHG set-up schematics. The incident angle scan is accomplished by moving retroreflector on a motorized stage, which accordingly shifts pump light beam position at back aperture of microscope objective. M1, M2, M3 are silver mirrors. LP, BP, SP represent long-pass, band-pass, short-pass filters. PBS is polarized beamsplitter, DMSP is dichroic short pass mirror. The Mitutoyo NIR 20x (N.A.= 0.4) with 7.6mm diameter backaperture is mounted on a x-y-z manual translation stage. The sample is mounted on a manual rotation stage stacked on a x-y-z manual translation state. The rotation stage can rotate 360 degrees continuously in x-y plane.

To drive the out-of-plane dipole, a vertical electric field in a tilted incidence beam is generated by scanning beam position off-center at the back aperture of the microscope objective. Since the projected z-component of the field increases as the tilt angle increases, it is expected to observe SHG intensity rises in a polar crystal with vertical polarization. Specifically speaking, firstly, the p-polarized fundamental light excites the sample under normal incidence and p-polarized SHG signal I_p is collected. Because of C_3 rotation crystal symmetry, the SHG induced by the in-plane dipole can be extinct by rotating crystal in-plane with the Mo-X bond direction perpendicular to the electric field

[110]. Secondly, to drive the out-of-plane dipole, a vertical electric field in a tilted incidence beam is generated by scanning beam position off-center at the back aperture of the microscope objective. Since the projected z-component of the field increases as the tilt angle increases, it is expected to observe SHG intensity rises in Janus MoSSe (Fig. 4.8). In contrast, SHG from randomized MoSSe alloy without out-of-plane dipole should be insensitive to the increasing z-component electrical field. Note that the trend of absolute SHG intensity not only includes information on out-of-plane dipole but is affected by the system angle (or position) dependent collection efficiency. In order to exclude such extrinsic factor, *s*-polarized SHG I_s induced by the in-plane dipole with the same collection efficiency is measured and the ratio I_p/I_s is used to evaluate intrinsic dipole contribution.

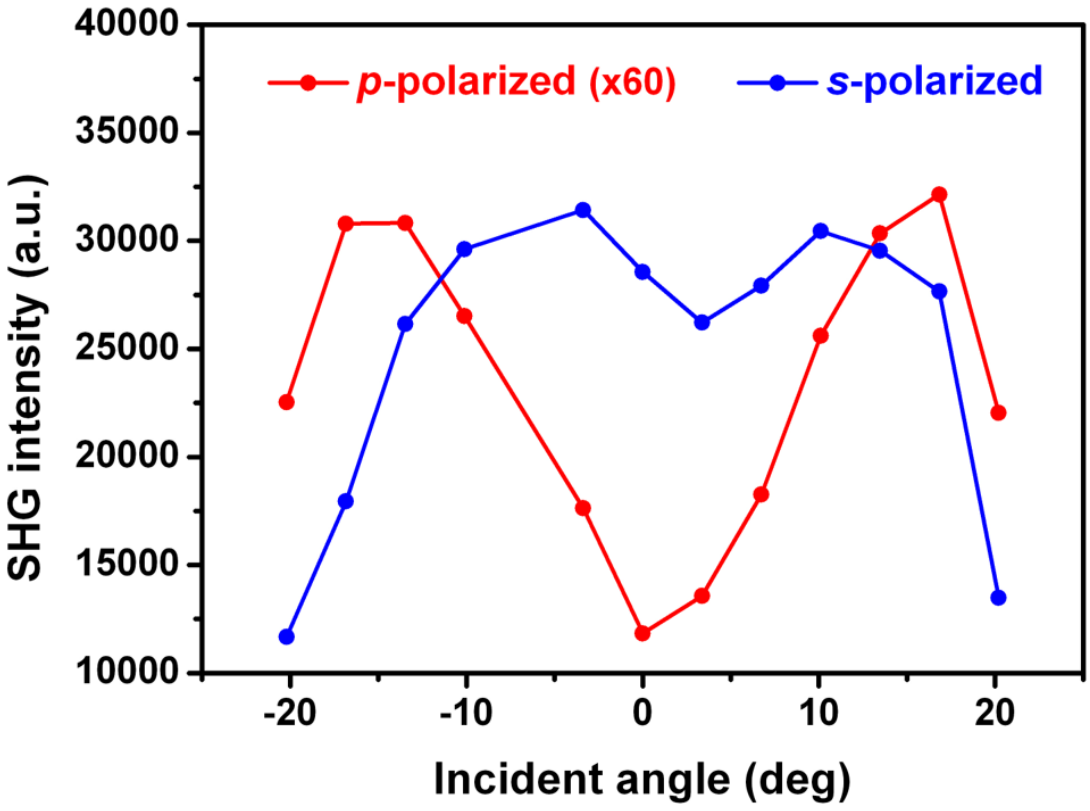

Figure 4.8: Angle dependent SHG signal from Janus MoSSe sample.

Figure 4.9 plots the angle dependent SHG ratio I_p/I_s from Janus and randomized MoSSe monolayers. The SHG of the Janus sample strongly depends on the incident angle while that from the alloy sample shows almost no change. In addition, such response is

symmetric for positive and negative tilt angle incidences. This observation confirmed the presence of an out-of-plane dipole in MoSSe monolayers.

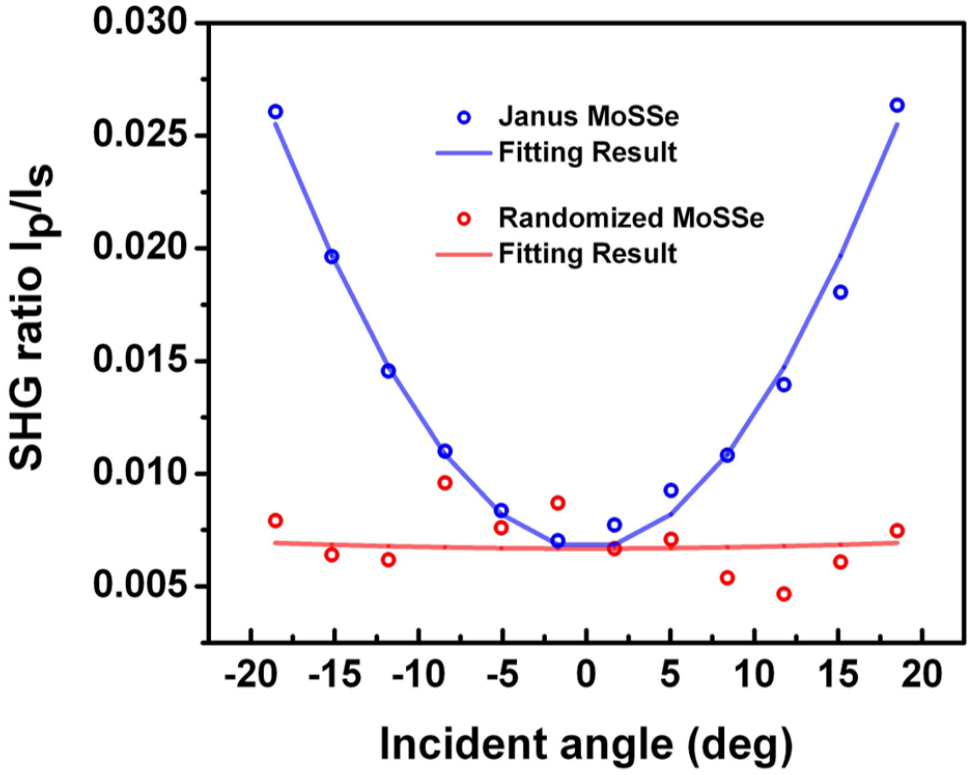

Figure 4.9: Angle-dependent SHG intensity ratio comparison. In the Janus MoSSe sample, the I_p/I_s ratio (blue circles) increases symmetrically with more tilted incidence, and is fitted well by an angle-dependent SHG model (blue curve). In the MoSSe alloy, the I_p/I_s ratio (red circles) undergoes almost no change as the incident angle varies, and the flat fitting (red curve) suggests a negligible out-of-plane dipole.

To extract the second-order susceptibility associated with the out-of-plane dipole, the data is fitted by an angle dependent SHG model described below.

$$I_p(\theta) = \eta(\theta) \cdot (\chi^{(2)}_{xxz} E_x(\theta)E_z(\theta)cos\,\theta + \chi^{(2)}_{xzx} E_z(\theta)E_x(\theta)cos\,\theta + \chi^{(2)}_{zxx} E_x(\theta)E_x(\theta)sin\,\theta)^2 \quad (4.1)$$

$$I_s(\theta) = \eta(\theta) \cdot (\chi^{(2)}_{yxx} E_x(\theta)E_x(\theta))^2 \quad (4.2)$$

$$E_x(\theta) = E_{in}(\theta)(1-r)\,cos\,\theta \quad (4.3)$$

$$E_z(\theta) = E_{in}(\theta)(1+r)\,sin\,\theta \quad (4.4)$$

$$r = \frac{r_{12}+e^{i2\delta}r_{23}}{1+e^{i2\delta}r_{12}r_{23}} \tag{4.5}$$

$$\delta = \frac{2\pi d_2}{\lambda}\, n_2\, cos\, \theta_2 \tag{4.6}$$

$$r_{ij} = \frac{n_j cos\theta_i - n_i cos\theta_j}{n_j cos\theta_i + n_i cos\theta_j} \tag{4.7}$$

Medium 1 is air, 2 is 2D material, 3 is sapphire substrate. Here SHG contributions from nonlinear susceptibility with two or three z index such as $\chi^{(2)}_{xzz}$ and $\chi^{(2)}_{zzz}$ are not considered due to small E_z/E_x field ratio and small ratio between out-of-plane and in-plane dipoles. Permutation symmetry requires $\chi^{(2)}_{xxz} = \chi^{(2)}_{xzx}$, if we further consider the fundamental and second harmonic photon energies are not resonant with any absorption peaks of monolayer MoSSe, Kleinman symmetry can be applied for a fair evaluation. Therefore, $\chi^{(2)}_{xxz} = \chi^{(2)}_{xzx} = \chi^{(2)}_{zxx}$.

$$\frac{I_p(\theta)}{I_s(\theta)} = \left[\frac{(3+r)sin\theta}{(1-r)} \cdot \frac{\chi^{(2)}_{xxz}}{\chi^{(2)}_{yxx}}\right]^2 \tag{4.8}$$

Meanwhile, for monolayer, its thickness d_2 is much smaller than wavelength λ. This simplifies expression for $r = \frac{r_{12}+r_{23}}{1+r_{12}r_{23}} \approx r_{13} = \frac{n_3 cos\theta_1 - n_1 cos\theta_3}{n_3 cos\theta_1 - n_1 cos\theta_3}$ ($n_1 sin\theta_1 = n_3 sin\theta_3$, $n_1 = 1, n_3 = 1.7542$ @$1080nm$), the approximation is confirmed by simulation shown in Fig. 4.10.

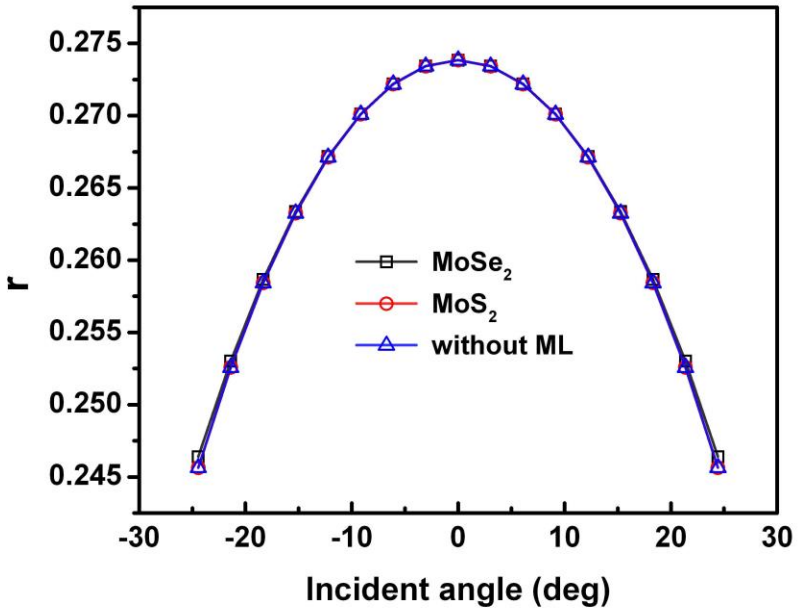

Figure 4.10: Angle dependent reflection coefficient r for 1080nm pump light.

The simulation considers three-layer structure air/2D material/sapphire. It confirms the approximation $r = \frac{r_{12}+r_{23}}{1+r_{12}r_{23}} \approx r_{13}$. By fitting data with formula (1) as θ varies, the ratio between second-order susceptibility linked with in-plane dipole and that linked with out-of-plane dipole could be extracted. Because of the relationship between second-order susceptibility and dipole matrix elements

$$\chi^{(2)}_{ijk}(2\omega,\omega,\omega) \propto \frac{\mu^i_{gn}\mu^j_{nm}\mu^k_{mg}}{(\omega_{ng}-2\omega)(\omega_{mg}-\omega)} \tag{4.9}$$

$$\mu^i_{gn} = < g|\hat{\mu}|n >_i \tag{4.10}$$

Such ratio infers similar magnitude comparison between in-plane and out-of-plane dipole strength for same optical transitions. Based on the above SHG fitting model for angle dependent SHG measurements, the well-matched fitting confirmed that second-order susceptibilities $\chi^{(2)}_{xxz}$, $\chi^{(2)}_{xzx}$, $\chi^{(2)}_{zxx}$ play the role and infer the magnitude ratio $\chi^{(2)}_{yxx}$: $\chi^{(2)}_{xxz}$ = 10 :1 at 1080 nm pump. To statistically confirm the vertical dipole SHG response, we measured five MoSSe Janus samples and three MoSSe alloy samples, whose second-order susceptibilities are summarized in Fig. XX. For all asymmetric samples, the out-of-plane dipole generates observable $\chi^{(2)}_{xxz}$, $\chi^{(2)}_{xzx}$, $\chi^{(2)}_{zxx}$ with little variation. While for all randomized samples, the out-of-plane dipole response is almost one order of magnitude smaller and within measurement limit (Fig. 4.11).

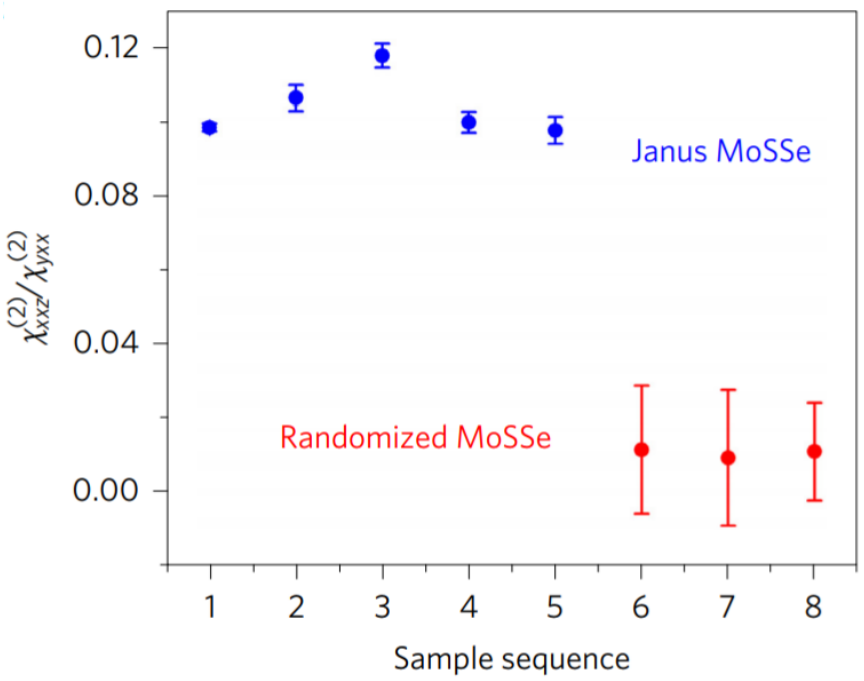

Figure 4.11: Second-order susceptibility ratio statistics. Five Janus MoSSe samples show a consistent out-of-plane and in-plane second-order susceptibility ratio (1:10); in

contrast, three MoSSe alloy samples show a one order of magnitude smaller ratio. The error bars represent fitting error.

In conclusion, we have made breakthroughs in 2D polar crystal development by creating non-equivalent (Janus) surfaces on MoS_2 monolayers through controlled atom replacement to form MoSSe monolayers, where the anticipated optical dipole and piezoelectric properties are verified in an atomically thin level. In the case of monolayer MoSSe, the saturation of surface bonds in the van der Waals layered material prevents surface reconstruction and thus preserves out-of-plane dipoles. In addition, monolayer MoSSe has direct band gap located at K/K' valley in Brillion zone. Such unique valley degree of freedom is important for potential valleytronics and absent in conventional polar materials. This synthetic Janus 2D monolayers by design are expected to provide an excellent platform for studying the surface chemistry and Rashba spin transport physics at the 2D physical limit.

4.5 Introduction to 2D ferroelectricity in ultrathin In_2Se_3

The above monolayer MoSSe proves to exhibit out-of-plane polarization. However, such polarization is expected to be almost impossibly flipped given the reversal requires S and Se migration through Mo atom plane. On the other hand, if the polarization in a 2D polar crystal can be stabilized and electrically switched to another energy-degenerate polarization direction, discovery of such 2D material can provide a unique platform to explore 2D ferroelectric physics and establish novel 2D memory devices.

Ferroelectric ordering dictates electrically switchable macroscopic polarization, arising from spontaneous alignment of electric dipoles [111], [112]. Such collective phase reveals fundamental interplay between crystal symmetry and quasiparticle interactions [113], [114]. The development of ferroelectric materials such as barium titanate ($BaTiO_3$) was also prompted by applications like electromechanical actuators and storage devices [115]. However, the strength of polarization and transition temperature drop as ferroelectric films scale down due to the reduced long-range Coulomb coupling and enhanced depolarization field (Fig. 4.12), and ferroelectricity disappears below a critical thickness [111], [116]–[118]. In addition, interfacial bonding related strain and chemical environment can also deteriorate thin film ferroelectricity[119]–[121]. In contrast, the emerging van der Waals layered materials have strong intralayer chemical bonds but weak interlayer interactions, and thus could provide a pathway to eliminate the role of interfacial defects and strain. With the presence of this strong anisotropy, 2D layered materials may go beyond such limitations and are unique platforms to study fundamental electronic and structural ordering in two dimensions [32], [122], [123]. Ferroelectricity in 2D materials is not only significant for device miniaturization but may reveal novel domain physics with enhanced quasiparticle interactions [22], [24]. Furthermore, the ferroelectric switching allows the control of asymmetry-induced properties such as spin-orbit coupling, valley degree of freedom and anisotropic transport [15], [25].

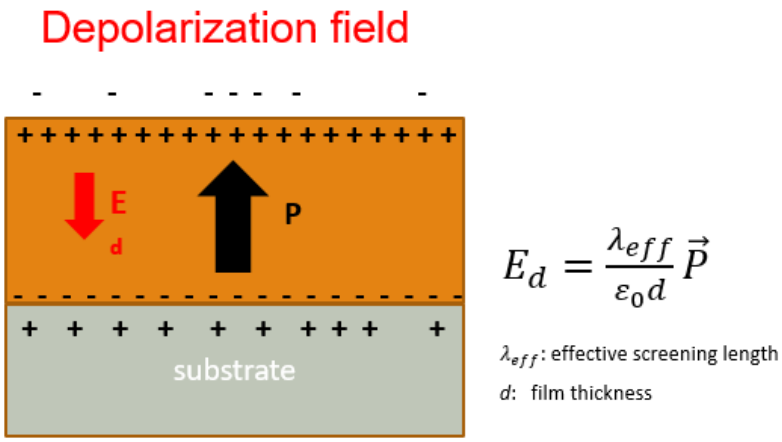

Figure 4.12: Schematics of depolarization field in a ferroelectric film.

While in-plane oriented spontaneous polarization can exist in single-unit-cell-thick materials [124], depolarizing electrostatic fields and interfacial chemical bonds with the substrate tend to destroy out-of-plane ferroelectricity in thin film ferroelectric crystal [117], [118], [120], [121]. Efforts have been made to stabilize the out-of-plane polarization and reduce the critical thickness by providing extrinsic screening from a conductive substrate [125]. Recently, a theoretical proposal reveals a new mechanism to achieve intrinsic out-of-plane ferroelectricity based on the strong correlations of covalent lattice structure [126]. In the following, I experimentally demonstrate intrinsic out-of-plane 2D ferroelectric ordering and unique polarization locking in atomically thin In_2Se_3 crystals, which has been predicted to be a ferroelectric semiconductor [126].

4.6 Polar crystal structure and unique dipole locking relationship in ultrathin In_2Se_3

Each In_2Se_3 layer contains five triangular atomic lattices stacked in the sequence of Se-In-Se-In-Se through covalent bonds and belongs to R_{3m} space group (No. 160). The asymmetric position of Se atom in the middle spontaneously breaks the centrosymmetry, providing two energetically-degenerate states with opposite out-of-plane electric polarization and in-plane asymmetry with reverse second-order nonlinear polarization (Fig. 4.13a and b). The stabilization of ferroelectricity is achieved primarily through the out-of-plane and in-plane polarization locking enforced by unique covalent bond configuration of In_2Se_3 crystal, instead of long-range Coulomb interaction in conventional ferroelectric materials [127]. To erase or even flip the out-of-plane electrical polarization, the middle Se atom must also move laterally (~ 100 pm) accompanied by the In-Se covalent bonds breaking and forming [126]. It is fundamentally distinct from traditional ferroelectric switching wherein small uniaxial atomic distortions (~ 10 pm) occur without bond breaking in, for example, perovskite oxides or via molecular chain

rotation in PVDF [128]. Such additional in-plane atomic movement enforced by locking provides strong resistance for out-of-plane polarization against depolarization field. Accordingly, the calculated domain wall energy is also several times to more than one order of magnitude larger than that in perovskite oxides such as $PbTiO_3$ and $BaTiO_3$ [126], [129], [130]. These features also distinguish the ferroelectricity in In_2Se_3 from recent reports on atomically thin SnTe and $CuInP_2S_6$ [124], [125], whose polarization only involves either pure in-plane or out-of-plane atomic distortion without breaking of covalent bonds. As a consequence, SnTe cannot exhibit out-of-plane polar order, while the ferroelectricity in $CuInP_2S_6$ does not exist below 50 nm in the absence of extrinsic electronic screening by a conductive substrate. Therefore, discovery of intrinsic 2D ferroelectricity based on the unique polarization locking provides a new degree of freedom to control structural and electronic ordering in layered materials, construct multiferroic heterostructures and scale down ferroelectric device.

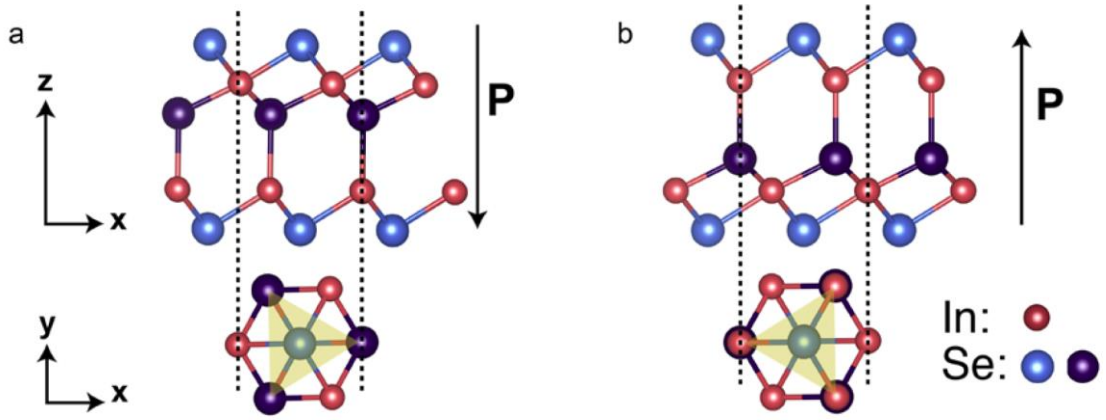

Figure 4.13: Two energy-degenerate ferroelectric In_2Se_3 structures. Single quintuple layer consists of covalently bonded indium and selenium triangular lattices. The crystal belongs to R_{3m} space group (No. 160). The polarization flipping requires locked out-of-plane and in-plane motion of middle Se atom (purple ball) accompanied by covalent bond breaking and formation, and reverses both the out-of-plane polarization and the in-plane lattice orientation with nonlinear optical polarization.

4.7 Sample preparation and basic optical characterization of In_2Se_3

We prepared atomically thin membranes of In_2Se_3 by both exfoliation and van der Waals epitaxial growth [131], [132]. Their thickness was then determined by atomic force microscopy, and the single layer step height is 1 nm (Fig. 4.14).

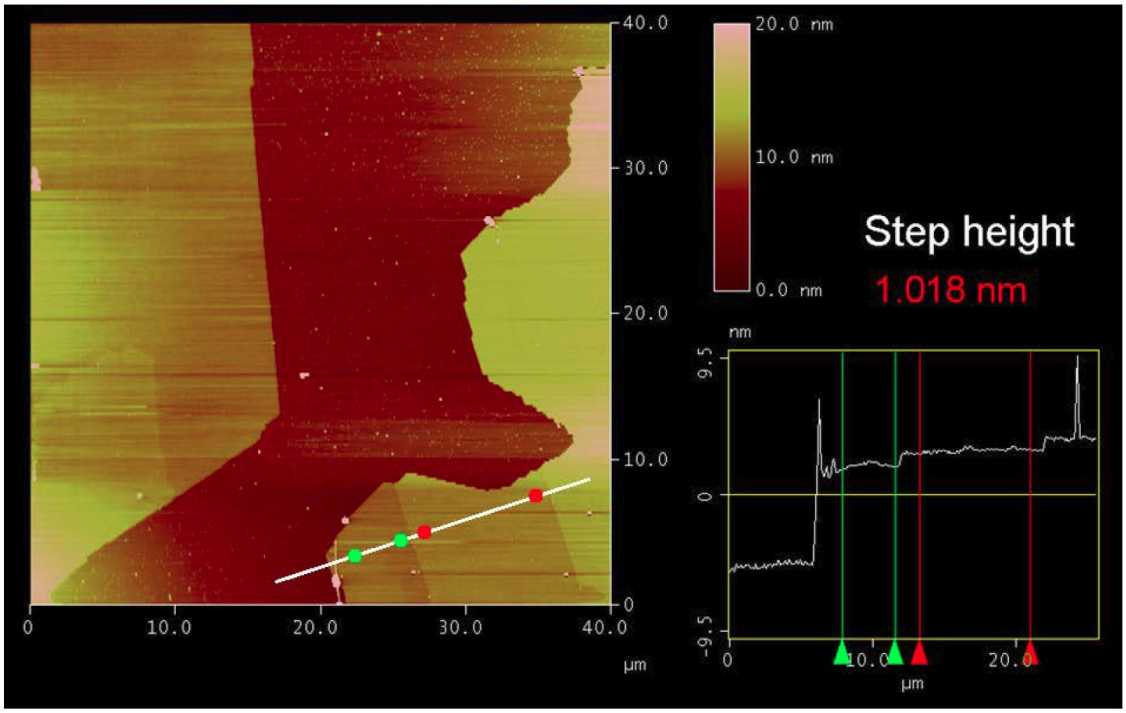

Figure 4.14: Measuring height of atomically thin In_2Se_3 samples by AFM. The CVD-grown layered In_2Se_3 is typically a few nanometers thick and tens of micrometers in lateral size. The bottom right panel shows the cross section corresponding to the white line. Each layer is around 1-nm-thick, measured by the smallest steps found in the height profile. The step height in the figure was calculated from the difference of average height of the regions between the green lines and red lines.

Meanwhile, the samples with strong SHG signal display the same Raman characteristic peaks (Fig, 4.15, Fig. 4.16a), as reported for α-phase In_2Se_3 [131]. Raman spectroscopy was performed by a commercial Raman system (Horiba Labram HR evolution) under normal incidence with a 532 nm laser. The laser beam was focused on the samples by 50X objective (N.A. = 0.6) and the beam diameter is ~1μm. Both grown and exfoliated samples were characterized in vacuum with moderate incident power to avoid damage. We found two sets of Raman characteristic peaks in grown ultrathin samples (figure 4.16a). Based on literature report [131], one corresponds to alpha phase, the other one corresponds to beta phase. The exfoliated samples are all alpha phases. SHG spectroscopy can further distinguish the alpha and beta phase in growth samples by the significant intensity difference. As shown in figure 4.16b, SHG intensity from alpha phase grown sample is about 1-2 orders higher than that from beta phase grown sample in ultrathin samples with same thickness. Such difference is repeatedly observed, which results from the inversion symmetry preservation (or breaking) in corresponding nonpolar (or polar) crystal structures. Therefore, we identified the strong correlation among SHG intensity, Raman peaks and corresponding crystal structure. Since alpha phase is the

target ferroelectric structure, we utilized SHG spectroscopy and Raman spectroscopy to screen growth samples and select alpha phase samples with strong SHG intensity and typical Raman modes for further study.

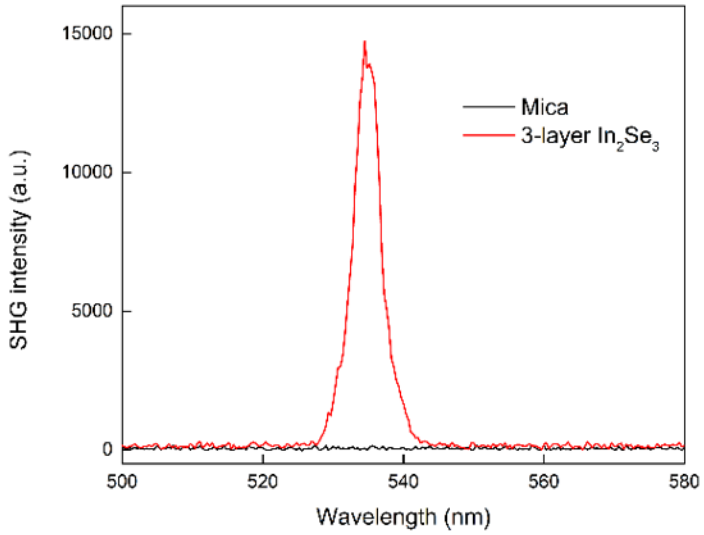

Figure 4.15: Strong SHG from alpha phase grown sample.

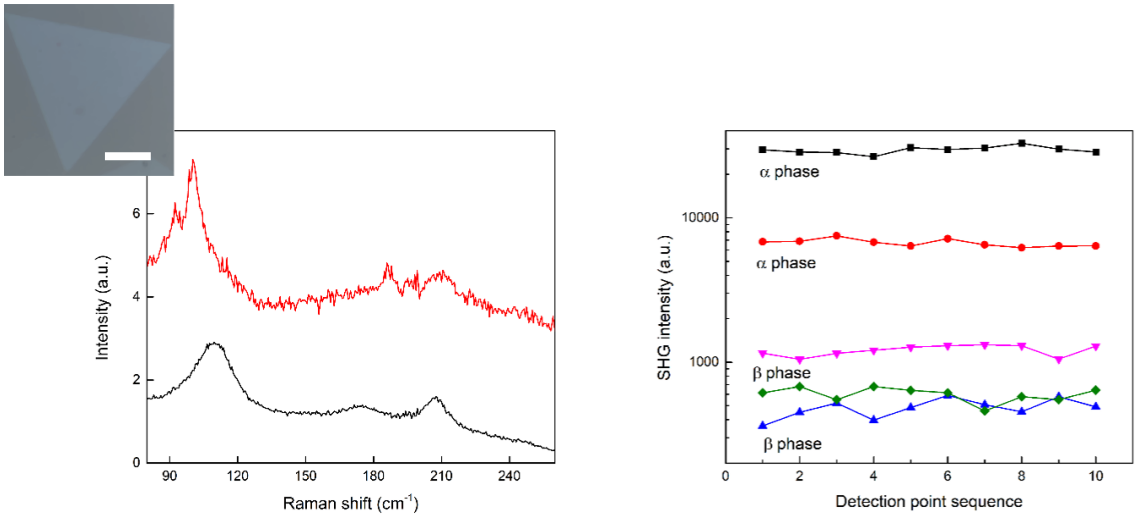

Figure 4.16: Raman and SHG characterization of ultrathin growth In_2Se_3 crystal. **a,** Raman spectra from two typical grown trilayer samples. The red curve shows typical Raman peaks for alpha phase In_2Se_3 while the black curve represents Raman feature from

beta phase In_2Se_3. All Raman measurements were conducted in vacuum chamber with moderate incident light power to avoid damage. The inset is typical optical image of a trilayer sample. The scale bar is 10 μm. **b,** Corresponding SHG comparison for ultrathin growth samples with different crystal phases. We first identified two alpha phase and three beta phase trilayer samples by Raman spectroscopy. Based on SHG measurement, SHG intensity from alpha phase grown samples is about 1-2 orders higher than that from beta phase grown samples, resulting from inversion symmetry breaking in its polar structure. Although current growth method leads to coexistence of alpha and beta phase ultrathin flakes, we identified the strong correlation among SHG intensity, Raman peaks and corresponding crystal structure for selection of samples with polar structure.

4.8 In-plane and out-of-plane asymmetry probed by SHG

To verify the presence of in-plane and out-of-plane asymmetry, we performed SHG studies with normal and oblique incidence at ambient conditions. The excitation light was extracted using an optical parametric oscillator (Inspire HF 100, Spectra Physics, Santa Clara, USA) pumped by a mode-locked Ti:sapphire oscillator. The excitation laser was linearly polarized by a 900–1300 nm polarizing beamsplitter. The transmitted *p*-polarized laser light can change its polarization by rotating a IR half waveplate before pumping sample. The laser is focused by a 50x NIR objective on sample. The second harmonic generation signal was detected in the backscattering configuration, analyzed by a visible-range polarizer, and finally collected by a cooled CCD spectrometer.

First, the SHG signal from a trilayer sample on insulating mica substrate can be observed under normal incidence (Fig. 4.15), which indicates inversion symmetry breaking with the presence of in-plane nonlinear optical polarization. The polarization-resolved SHG shows a six-fold intensity pattern when the excitation and detection polarization are rotated collinearly (Fig. 4.17). In this configuration, the fundamental pump beam was normal incident along z axis (perpendicular to In_2Se_3 layer) and linear polarized in x-y plane (parallel to In_2Se_3 layer). Only tensor elements with x and y components contribute to SHG signal. In_2Se_3 crystal belongs to R_{3m} space group with a 3-fold rotation symmetry along the z-axis, and a mirror symmetry with respect to the x-z plane, given coordinate axes depicted in Fig. 1b. Therefore, the only nonzero tensor components responsible for the SHG signal in Fig. 1c are χ_{xxx}, χ_{xyy}, χ_{yxy} and χ_{yyx}, with the following relationship: $\chi_{xxx} = -\chi_{xyy} = -\chi_{yxy} = -\chi_{yyx}$ [110], [133]. When the polarization of the excitation and the detection are kept the same and rotate together with respect to the crystal, the SHG intensity response is simply: $I = I_0 \cos^2(3\theta+\theta_0)$, where θ is crystal angle, θ_0 is the angle difference between laser polarization and crystal angle. Therefore, the observation of six-fold SHG intensity pattern is a clear signature of the crystalline belonging to R_{3m} space group, and the maximum of each lobe corresponds to the In-Se bond armchair direction. Although this three-fold rotational symmetry prohibits in-plane electric dipole polarization, it gives an effective in-plane second-order optical dipole emission due to inversion symmetry breaking [134].

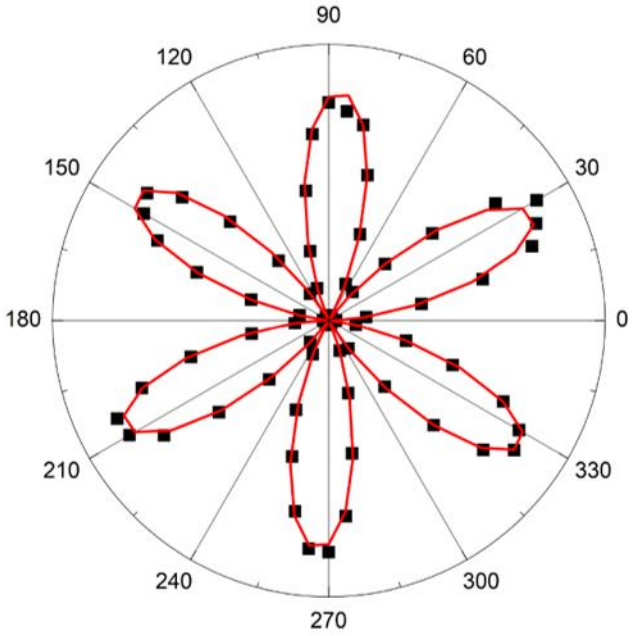

Figure 4.17: SHG polarization pattern of a trilayer In_2Se_3. The intensity is a function of crystal angle. The three-fold rotational symmetry manifests through the six-fold SHG intensity pattern (black square) when the polarization of the optical excitation and detection are rotated collinearly. The sample was under normal incidence. Red curve shows the fitting by $I = I_0 \cos^2(3\theta+\theta_0)$, θ is crystal angle.

Next, we used angle-resolved polarization-selective SHG measurements to observe the out-of-plane dipole [57]. By rotating the crystal to make the In-Se bond direction perpendicular to both the incident and detecting polarization direction, the SHG induced by the in-plane dipole is made extinct. Then the vertical electric field in a tilted beam drives the out-of-plane dipole and gives rise to a SHG signal (Fig. 4.18). Figure 4.18 shows the incident angle dependent SHG from the out-of-plane dipole in the same trilayer sample, normalized with collection efficiency. As the tilt angle increases, SHG intensity increases as the z-component of the optic electrical field becomes stronger and is symmetric for positive and negative tilt angle. This observation confirmed the presence of an out-of-plane asymmetry in the In_2Se_3 ultrathin crystals, which is the prerequisite for 2D out-of-plane ferroelectricity. The ratio between in-plane and out-of-plane second-order susceptibility is 13.6:1 at 1080 nm pump, consistent with the theoretical estimation that the static in-plane dipole is more than one order of magnitude larger than the out-of-plane dipole [126].

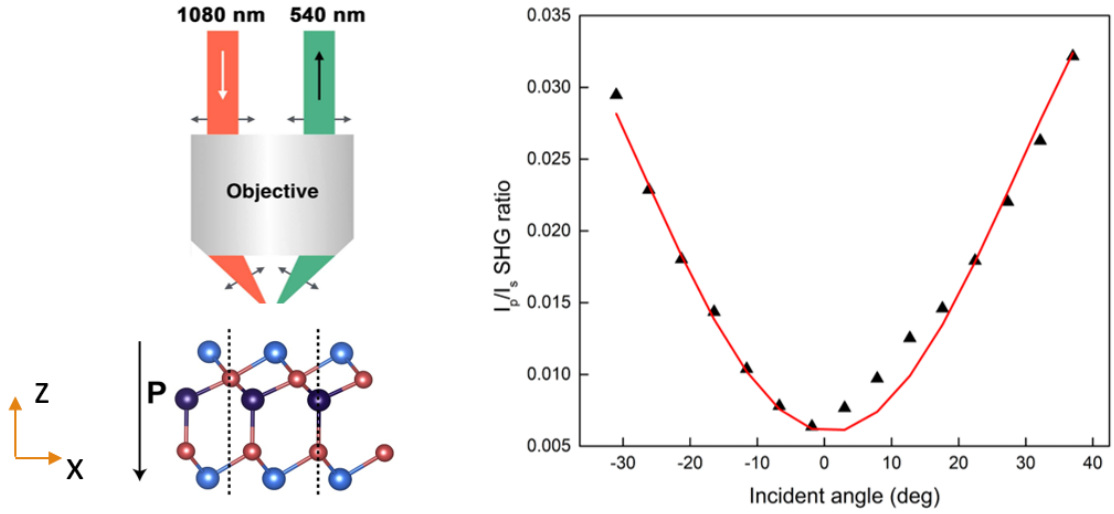

Figure 4.18: Out-of-plane dipole probed by angle resolved SHG of a trilayer sample. Angle-dependent SHG intensity ratio I_p/I_s increases symmetrically with tilted incidence (black triangular) and agrees well with the model of response from out-of-plane dipole to vertical electrical oscillation field, indicating the ratio (13.6:1) between in-plane and out-of-plane second-order susceptibility at 1080 nm pump (red curve,

An annular dark-field scanning transmission electron microscopy (ADF-STEM) cross-section image of a multilayer In_2Se_3 also confirms the asymmetric ferroelectric crystal structure as predicted (Fig. 4.19). In the following, I will discuss how the combination of piezoresponse force microscopy and SHG microscopy can reveal ferroelectric switching and dipole locking relationship in In_2Se_3.

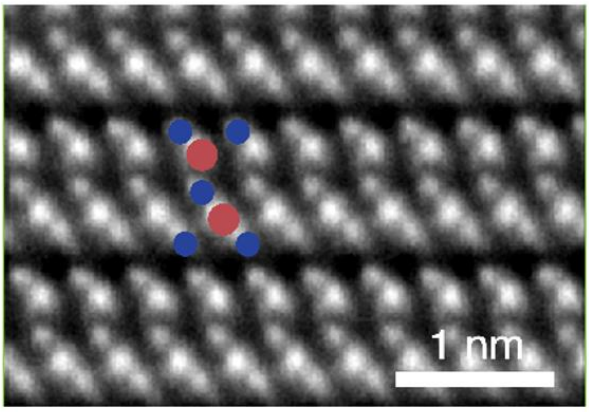

Figure 4.19: Cross-section image of an In_2Se_3 alpha phase multilayer flake. High-angle annular dark-field scanning transmission electron microscopy shows the polar structure of each layer with In (brown) and Se (blue) atoms.

4.9 Piezoresponse force microscopy

When it comes to studying the electromechanical response at nanoscale, piezoresonse force microscopy is a common technique widely applied [135]. It provides precise control over local electrical environment and high sensitivity of piezoelectric displacement to characterize traditional bulk piezoelectric and ferroelectric materials. General PFM is based on AFM integrated with specific electrical feedback module.

Typically, the PFM tip is in contact with the sample with constant force while the height of the tip is maintained by a low-frequency feedback loop. In the meantime, a high-frequency AC bias is applied between the tip and the sample. If the sample is piezoelectric, the oscillation electric field creates a proportional local strain as well as a mechanical vibration of the surface:

$$\boldsymbol{S}(\omega) = \boldsymbol{d} \cdot \boldsymbol{E}(\omega) \tag{4.11}$$
$$\boldsymbol{A}(\omega) = \boldsymbol{d_{eff}} \cdot \boldsymbol{V}(\omega) \tag{4.12}$$

where ω is the angular frequency of the bias, $\boldsymbol{S}(\omega)$ is the local strain, $\boldsymbol{A}(\omega)$ is the mechanical vibration, $\boldsymbol{d}$ is piezoelectric coefficient matrix, $\boldsymbol{d_{eff}}$ is the effective piezoelectric coefficient. Usually such vibration is small given piezoelectric coefficient is on the order of pm/V. In order to extract such small signal and avoid other artifacts such as electrostatic capacitor force and Joule heating (these are 2ω terms), a lock-in amplifier is used to track at oscillation frequency. With lock-in technique, the sensitivity of is high enough to detect very small electromechanical coupling (<0.1 pm/V), but at the cost of increasing integration time. Since scanning images are taken for contrast analysis, PFM is most used to characterize strong piezoelectric materials like ferroelectric perovskite oxides. This integration time issue sets a significant challenge for probing weak piezoelectric materials. To address this problem and boost sensitivity, researchers utilized mechanical resonance of the cantilever and developed the dual-frequency resonance-tracking to enhance the signal contrast by more than 100 times [136].

4.10 Ferroelectric domain structures in ultrathin In_2Se_3

In addition to the presence of dipoles, SHG and complementary PFM mapping of the trilayer at room temperature reveals domains and domain boundaries as shown in Fig. 4.20. The region with stronger SHG displays larger piezoresponse, while the region with weaker SHG shows smaller piezoresponse amplitude. The correlation indicates that the as-grown sample contains domains with different net dipole strength. We verified that the dipole strength difference does not come from composition inhomogeneity, because both regions give the same Raman spectra, meaning they have the same crystal phase. Therefore, we postulate that for as-grown sample, some regions are well aligned along one polarization,

while other regions may partially include lattice configuration with opposite polarization and reduce the average nonlinear optical response. Similar intensity variation has also been observed for SHG generated by out-of-plane dipole. In addition, in the SHG image we observed dark lines within the area that has uniform optical contrast (Fig. 4.20a inset). By superimposing these dark lines onto the piezoresponse and the phase mapping (blue curves in Fig. 4.20b, c), we found that they always occur at the boundaries of two 180-degree domains with comparable piezoresponse and SHG amplitude. The consistency proves that they result from destructive interference between the optical fields from adjacent domains with opposite polarizations [69]. On the other hand, for the boundary between a domain with large positive piezoresponse and a domain with small negative piezoresponse, SHG dark lines are shadowed due to the imperfect optical destructive interference.

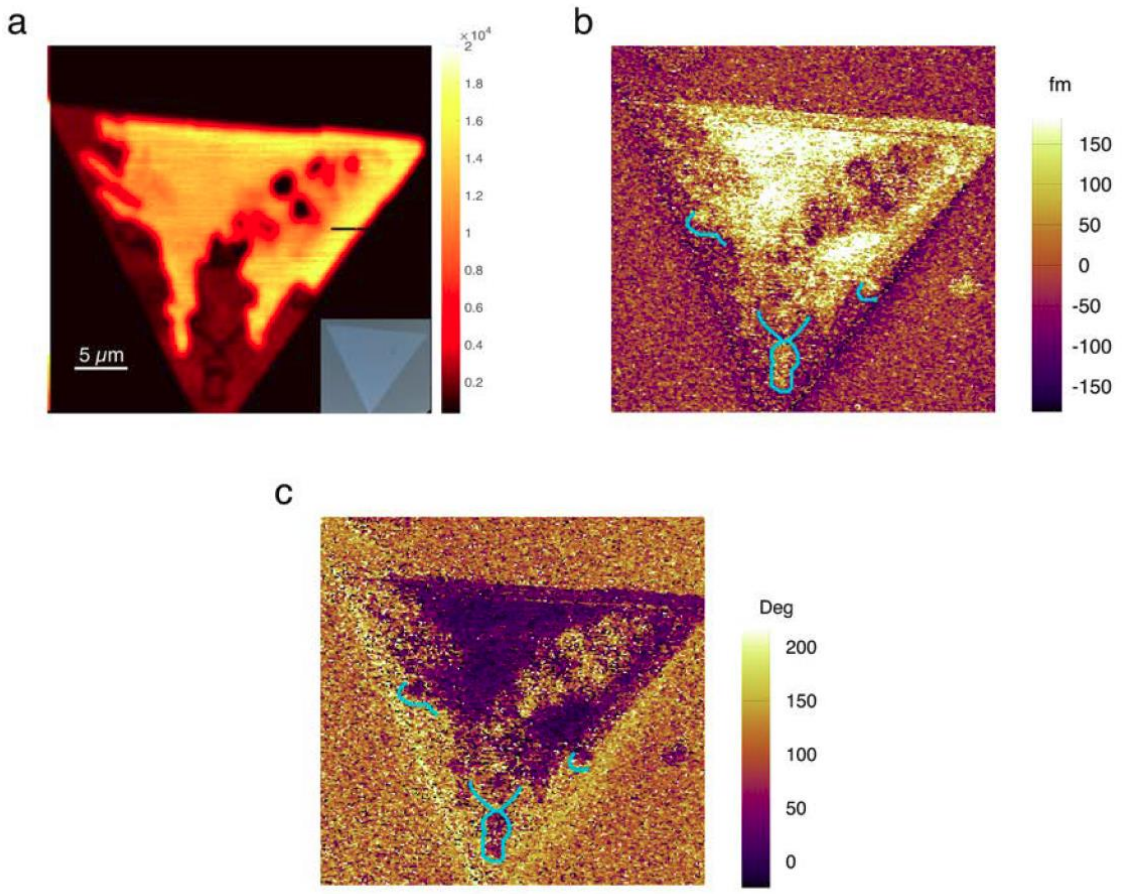

Figure 4.20: Visualization of domain structure in 2D In_2Se_3. **a,** SHG mapping of the 3-nm In_2Se_3 crystal, showing intensity contrast in different regions corresponding to domains with different dipole strength that match well with the piezoresponse mapping in **b**. The inset is the optical image of the same sample. SHG intensity dark lines are observed within the region of nearly uniform optical contrast and SHG intensity, that also match

the boundaries between domains with 180-degree piezoresponse phase contrast in **c** (blue curves). They originate from the destructive interference from the oppositely polarized domains.

On the other hand, the validity to identify antiparallel domains through SHG dark lines is supported by the similar intensity dip width and depth in In_2Se_3 domain structures and the boundary of two triangular monolayer MoS_2 with opposite orientation. In detail, a SHG intensity line scan orthogonally across two adjacent domains shows intensity dip around the domain wall position. The intensity dip originates from destructive SHG interference when light spot covers antiparallel domains. The width of such observed dip is mainly determined by the width of fundamental beam instead of the real domain wall width (Fig. 4.21a). Similar dark lines with comparable width can also be observed at the boundary of two triangular monolayer MoS_2 with opposite orientation, which proves the validity to identify antiparallel domains through this feature (Fig. 4.21b). The nonzero minimum may result from imperfect beam optics.

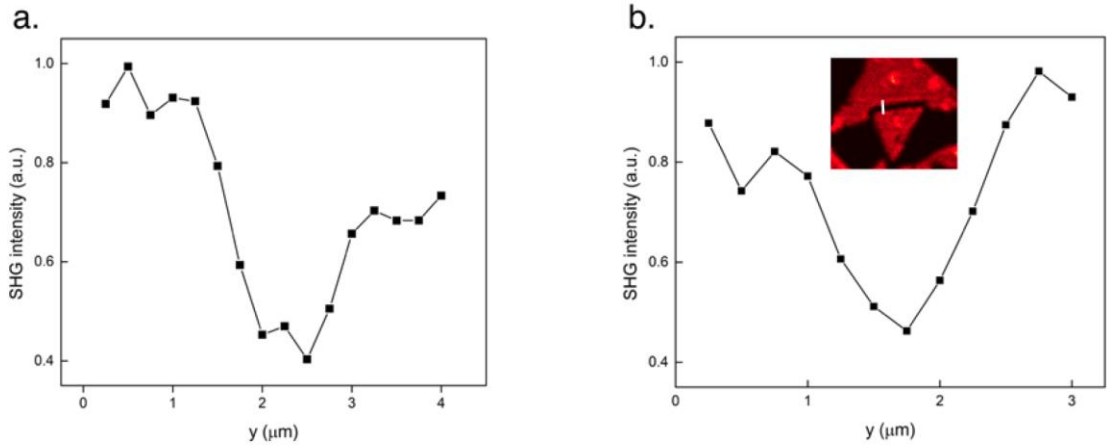

Figure 4.21: SHG dark line analysis. **a,** SHG line scan across the boundary between two domains with opposite orientations on a trilayer In_2Se_3 sample. **b,** SHG line scan across the boundary between two triangular monolayer MoS_2 with opposite orientations (white line in inset). Similar "dark" line was observed in SHG mapping originating from destructive SHG interference. The nonzero minimum may result from imperfect beam optics.

4.11 Electrical switching of out-of-plane ferroelectric polarization

Beyond the presence of polar structures with opposite spontaneous polarizations, we also demonstrated the switch of the polarization by applying electric field. Indeed, for ultrathin ferroelectric In_2Se_3, large out-of-plane field (~1V/nm) is predicted to flip the out-of-plane polar order. In the following, we demonstrated such polarization switching with vertical electric bias at room temperature. The sample was prepared by transferring the as-grown In_2Se_3 flakes onto strontium ruthenium oxide ($SrRuO_3$) thin film deposited on a (001)-oriented strontium titanate ($SrTiO_3$) substrate, which served as the back electrode. The electric field was applied through a conductive tungsten carbide probe with radius of 20 nm, and then the polarization switching was observed separately through inverse piezoelectric effect by resonance-enhanced piezoresponse force microscopy. Figure 4.22a shows the single-point off-field hysteresis loop of the piezoresponse as a function of poling electric field for a trilayer flake. With small probe voltage of 0.5 V, the coercive field of this piezoresponse loop is about 2-3 V over the 3-nm thickness, comparable to the theoretical prediction. Such observed large coercivity confirms the large energy barrier between the two polarization states, which is necessary to combat the depolarization field at the 2D limit. As the probe voltage increases to 1.5 V close to the coercive field, the loop collapses in both amplitude and width. This is a clear signature of field-switchable electromechanical deformation expected from ferroelectricity in In_2Se_3, and distinguished from the electrostatic force-induced artifacts from charging in non-ferroelectric materials [137]. Based on the obtained coercive field of 3-nm-thick the trilayer, we further observed areal ferroelectric domain reversal by scanning the probe with constant bias. Both positive and negative piezoresponse domains were written onto the trilayer sample as shown in figure 4.22b. The pattern remained stable in ambient conditions for at least three days when it was probed again. It should be noted that although other contributions (*e.g.*, injected charge, chemical changes, diffusion of species, etc.) can give rise to PFM contrast, the long-term stability of this signal suggests a link with the structural change and not one of these other spurious effects. In particular, we exclude charging effect as the source of the electromechanical response, which should quickly dissipate for ultrathin semiconducting film on conductive substrate.

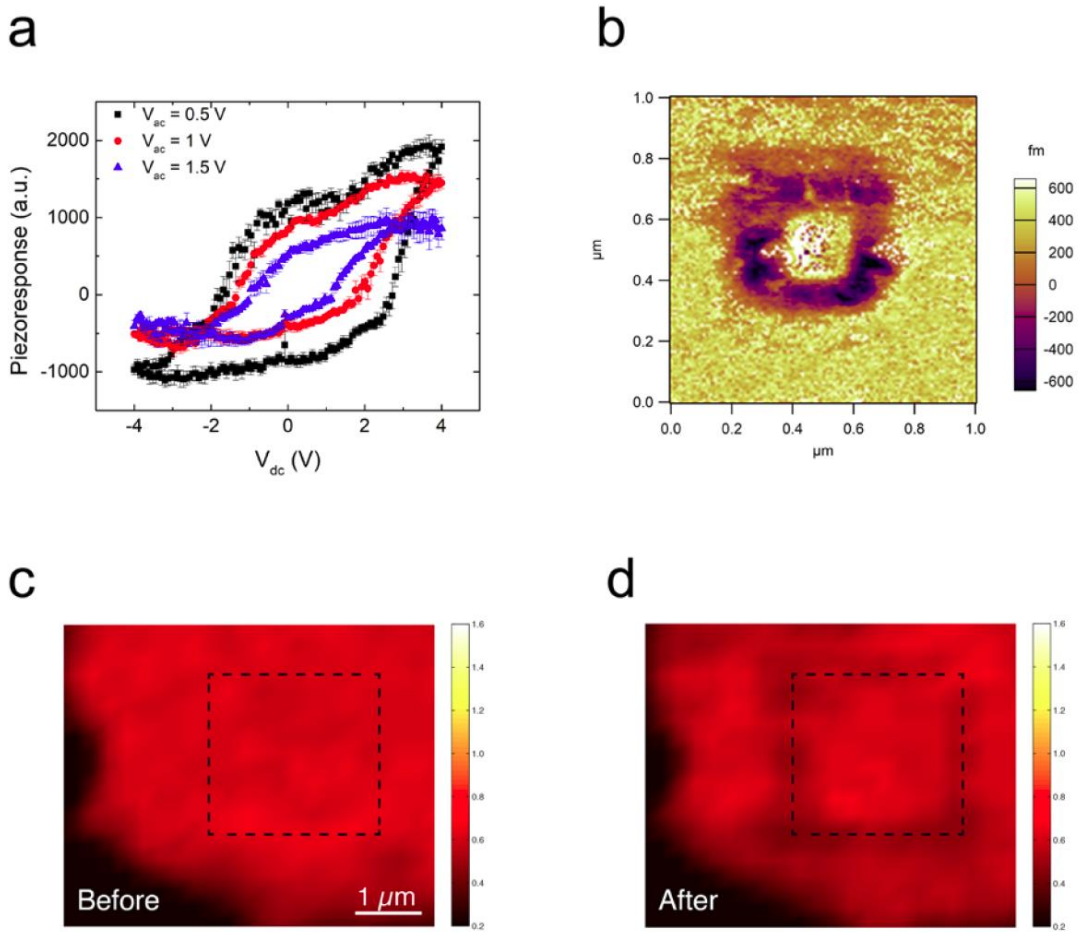

Figure 4.22: Switch of the out-of-plane polarization and in-plane configuration. **a,** The hysteresis of remnant out-of-plane polarization of a 3-nm-thick In_2Se_3 crystal on conductive $SrRuO_3$, as a function of perpendicular poling voltage. Black, red, blue curves represent the normalized piezoresponse measured with V_{ac} = 0.5, 1 and 1.5 V, respectively. The measured coercive voltage is between 2-3 V when V_{ac} is at 0.5V. When V_{ac} progressively increases to 1.5V and approaches the coercive field, both the effective switching voltage and the normalized response signal decrease. The collapse of the hysteresis loop agrees very well with the behavior of the conventional field-switchable ferroelectrics and is in contrast to the charging artifact of dielectrics. **b,** Polarized domain patterned by electrically biased scanning probe and measured by PFM. The inner box corresponds to positive applied voltage (+6V) and positive piezoresponse while the outer box to negative voltage (-6V) and negative piezoresponse. The piezoresponse signals were obtained from measured resonance amplitude and phase. **c,** SHG intensity mapping on another trilayer In_2Se_3 sample before PFM reversed poling. The area enclosed by dashed line was then scanning by a negatively biased AFM tip. The color bar is in linear scale with arbitrary unit. **d,** SHG mapping after the electrical reversed poling. The written area displays nearly uniform SHG intensity after reversal poling. We observed

appearance of SHG dark lines at the boundary of the patterned area resulting from destructive interference between the opposite in-plane crystal orientation and corresponding nonlinear optical polarization inside and outside reversal poling region. This finding not only confirmed the locking between the out-of-plane polarization and in-plane nonlinear optical polarization but demonstrated the functionality to manipulate in-plane crystal orientation through vertical electrical field.

4.12 Vertical electrical field switching in-plane lattice configuration

More strikingly, the unique polarization locking relationship in In_2Se_3 crystal structure requires that the in-plane atomic motion locked with the out-of-plane polarization switching and enables control in-plane asymmetry by out-of-plane electric fields. To demonstrate such control, we firstly selected one region of a trilayer In_2Se_3 sample on the $SrRuO_3/SrTiO_3$ (001) substrate showing strong SHG originating from in-plane dipoles (Figure 4.22c) and out-of-plane piezoresponse. Next, a rectangular region was scanned by a negatively biased probe and enclosed by dashed line (Fig. 4.22c). After the "writing" process, the orientation of the in-plane dipole was probed by SHG under normal incidence. Compared with the mapping before patterning, it showed unchanged SHG intensity distribution outside the "writing" region as well as uniform SHG intensity inside after reversal poling (Fig. 4.22d). Notably, we also observed clear dark lines with low SHG intensity exactly overlapping with the boundaries defined by the PFM writing pattern, evidencing the reversal of the in-plane nonlinear optical polarization and corresponding in-plane lattice asymmetry by the out-of-plane electric field patterning. Such observations further prove the strict locking between in-plane and out-of-plane dipoles, which allows electrical switching of in-plane crystalline symmetry by vertical electrical field.

Such dipole locking feature is also captured in previous SHG mapping measurement. I found the out-of-plane optical dipole has similar spatial intensity variation as that from in-plane dipole. In the line scan of the same sample (Fig. 4.23), large intensity variation and intensity dip between adjacent domains were observed. More interestingly, such variation trend matches well with that under normal incidence, indicating a strict correlation between in-plane and out-of-plane asymmetry. Such locking relationship is consistent with predicted ferroelectric crystal structure in which off-center distribution of Se atom is the common origin for both in-plane and out-of-plane asymmetry.

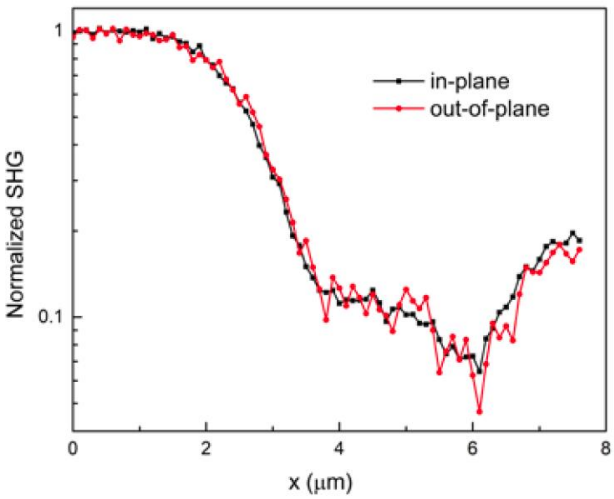

Figure 4.23: Observation of dipole locking from SHG intensity line scan. SHG from both dipoles show parallel variation after normalization, which is consistent with the strict polarization locking relationship in ferroelectric In_2Se_3 crystal structure. The SHG intensities in this figure is plotted with log scale.

4.13 Ferroelectric-centrosymmetric phase transition

Finally, I observed evidence of a temperature-induced phase transition in the ultrathin In_2Se_3 around 700 K by temperature-dependent SHG (Fig. 4). In a normal ferroelectric, increasing the temperature produces strong thermal fluctuations which act to destabilize the spontaneous polarization and drive the material into a high-temperature, high-symmetry structure possessing inversion symmetry. Similar effects were observed for a four-layer In_2Se_3 crystal transferred on a SiO_2/Si substrate. we first observed gradual SHG intensity decrease as a function of temperature over a broad range. The slow amplitude reduction of the SHG signal again confirms the robustness of the polar order. Starting at ~600 K, a sharp SHG intensity drop occurs, indicating the rapid disappearance of spontaneous polarization and the potential transition to a centrosymmetric phase. The observed high transition temperature is attributed to the energy difference between ferroelectric and high-temperature phases and the large kinetic transition barrier involving both in-plane and out-of-plane bond reconfiguration.

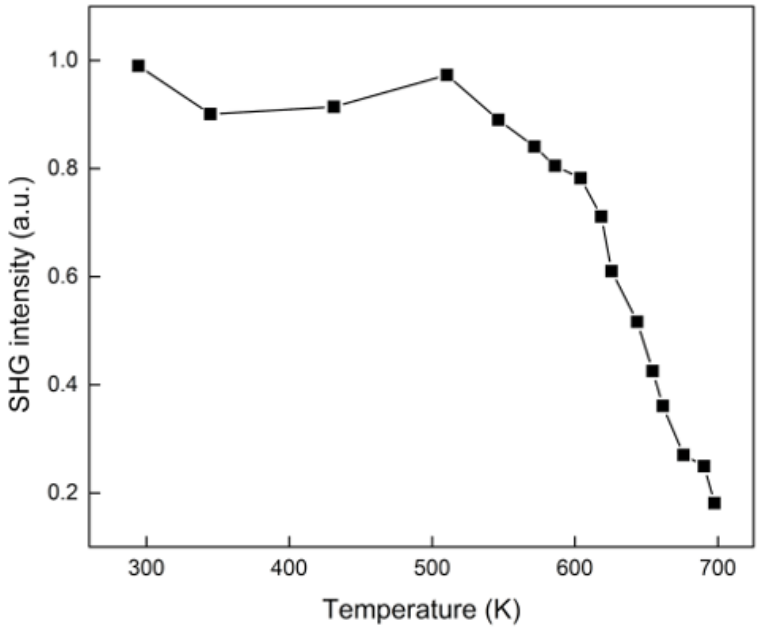

Figure 4.24: Observation of ferroelectric to centrosymmetric phase transition. The SHG intensity and the corresponding ferroelectric ordering remains robust as a four-layer In_2Se_3 sample on SiO_2/Si substrate was heated from room temperature to 600 K. It then dropped sharply to about one sixth of the initial value when the temperature further increased to 700 K, indicating the disappearance of spontaneous polarization and the structural transition to a centrosymmetric phase.

4.14 Conclusion

In conclusion, I have demonstrated out-of-plane ferroelectricity locked with in-plane asymmetry in ultrathin In_2Se_3 combining nonlinear optical analysis and electrical switching. Its unique covalent bond configuration and crystal symmetry lock the in-plane and out-of-plane atom movements, stabilizing the ferroelectricity even on dielectric substrates with little screening and result in a high transition temperature ~700 K. This discovery features new polarization switching mechanism involving covalent bond reconstruction and provides a unique platform to explore 2D ferroelectric physics and establish novel 2D optoelectronic devices based on polarization locking relationship.

Here I report the observation of locking between in-plane lattice asymmetry and out-of-plane dipoles, giving rise to intrinsic out-of-plane 2D ferroelectric ordering in atomically thin In_2Se_3 crystals. Through second harmonic generation (SHG) spectroscopy and piezoresponse force microscopy (PFM), we found switching of out-of-plane electric polarization leads to the flip of nonlinear optical polarization that corresponds to the inversion of in-plane lattice orientation. With such unique locking, the observed out-of-

plane polar order withstands depolarization field at ambient conditions and shows a very high transition temperature (~700 K) without the assistance of extrinsic screening. This discovery of intrinsic 2D ferroelectricity resulting from dipole locking offers new structural and electronic degree of freedoms in layered materials, which opens up possibilities to explore 2D vortex physics and develop ultrahigh density memory device and data storage [114], [138].

5 Structural engineering of 2D layered materials

In previous chapters, I explored several important topics in 2D layered materials such as valley degree of freedom and ferroelectricity, which originate from fundamental crystal symmetry breaking. In this chapter, I would further discuss how to engineer crystal symmetry through electrostatic doping, a new mechanism to manipulate structural phase transition and corresponding physical properties [59].

5.1 Introduction to multiple structures in 2D TMDCs

The discovery of atomically thin layered materials such as graphene and transition metal dichalcogenides has opened the exploration in two-dimensions. Compared with the bulk crystal, layered materials with reduced dimensions have two distinct features: highly confined in-plane motion of quasiparticles, and enhanced interactions among quasiparticles due to weak dielectric screening, both of which lead to unconventional phase transition physics in two-dimensional layered materials. Physical properties of layered materials can also be easily tuned by optical, electrical, and thermal stimuli, facilitating the development of device applications such as versatile memory.

Layered transition metal dichalcogenides (TMDCs) in the form of MX_2 (X = Se, S, Te, etc.) are covalently bonded within the layer, but weakly bound by van der Waals interactions between each layer. From semiconducting to metallic, the different electronic properties in TMDCs family results from the continuous electron filling of transition metal *d* bands [139]. Due to the three-atom layer, there are also multiple crystal configurations in TMDCs, each with distinct physical properties. In semiconducting TMDCs, the most commonly studied is the 2H phase (or 1H phase for monolayer, Fig. 5.1a), in which transition metal M atoms are trigonally coordinated with chalcogen X atom layers in Bernal (ABA) stacking. Typically, the bandgap transitions from indirect in the bulk to direct in monolayers [14]. In its monolayer form, inversion symmetry is broken and large spin-orbital splitting manifests in both conduction band ($\sim$ 10 meV) and valence band ($\sim$ 100 meV) [21]. Monolayer 2H MX_2 becomes direct bandgap semiconductor and breaks inversion symmetry, creating inequivalent K and K' valley [66], [140]. This valley degree of freedom together with the strong excitonic effect in low dimension make this phase unique platform for 2D valleytronics and optoelectronics [22], [24]–[27]. Alternatively, TMDC crystals can be in the 1T phase where the X atoms are octahedrally coordinated around M atoms in rhombohedral (ABC) stacking (Fig. 5.1b). If with a lattice distortion occurs along the in-plane axis, the variation is termed as 1T' structure [19], [20]. Monolayer TMDCs in 1T' phase maintain inversion symmetry (Fig. 5.1c). In addition, TMDCs in 1T' phase are mostly semimetals or narrow bandgap semiconductors. Coupled with the strong spin-orbit interactions, monolayer 1T' crystals are predicted to host a non-trivial topological state with the quantum spin Hall effect[19]. Various TMDC alloys like $MoS_{2x}Se_{2-2x}$ have also been synthesized with variable bandgaps [141].

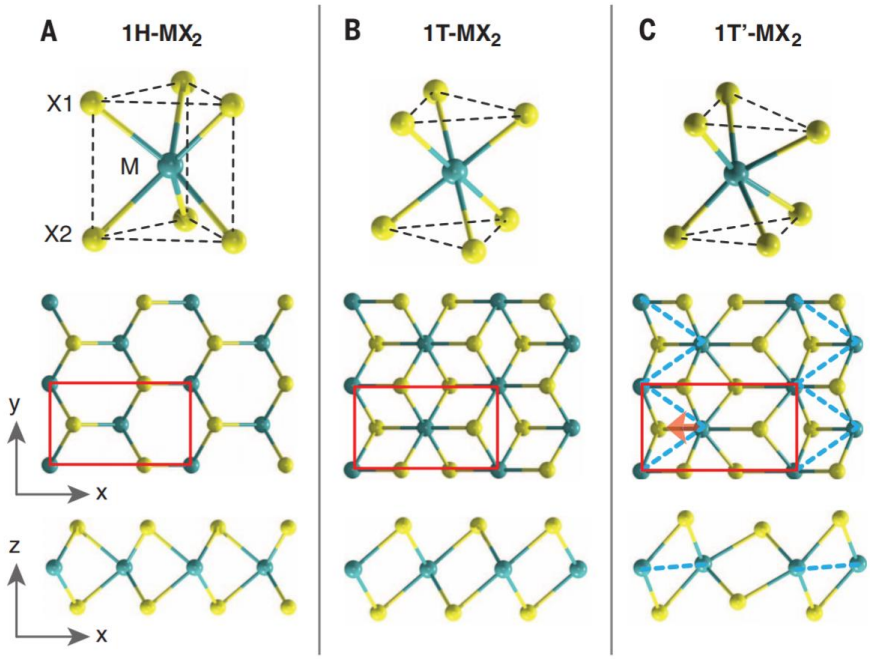

Figure 5.1: Atomistic structures of monolayer transition metal dichalcogenides MX_2. M stands for (W, Mo) and X stands for (Te, Se, S). (A) 1H-MX2 in ABA stacking with P6m2 space group. (B) 1T-MX2 in ABC stacking with P3m2 space group. (C) 1T′-MX2, distorted 1T-MX2, where the distorted M atoms form 1D zigzag chains indicated by the dashed blue line. The unit cell is indicated by red rectangles. Reprinted with permission from [19]. Copyright AAAS.

5.2 Structural phase transition in 2D materials

Phase transition dictates conversion between different thermodynamic states in a substance, ranging from common ice melting into water; to novel Bose-Einstein condensation [142]. The transition can be classified as a structural transition involving crystal lattice transformations or electronic structure transitions [143]. Studies on these phenomena in bulk materials have provided fundamental understanding of quasiparticle interactions in three-dimensionality and generated useful applications such as refrigerants and memory [144], [145].

The emerging layered transition metal dichalcogenides (TMDs) exhibit multiple crystal forms with distinct symmetry and topological characteristics [19], [146], [147], as described in last section. Such large contrast of physical properties, if reversibly controllable, potentially leads to broad applications such as memory, reconfigurable circuits and topological transistor at atomically thin limit [19], [145], [148]. The transition can also present fundamental understanding of how distinct physical characteristics interplay during phase coexistence in two dimensions.

Recently, large-scale and controllable structural phase transitions in atomic thin TMDs have been successfully realized [149]–[155]. Researchers have mapped out a phase diagram in which the stable 2H phase of $MoTe_2$ transforms into the 1T' phase at temperatures greater than 500 °C [154]. Slow (or fast) cooling from high temperature leads to the recovery of the 2H phase (or preservation of 1T' phase). Through such temperature control, the structural phase transition is reversible. In another work [153], laser light has been used as a local heat source to induce the 2H to 1T' phase transition in $MoTe_2$ at desired locations. By scanning the laser beam position, specific spatial patterns of 1T' $MoTe_2$ are created. Such local phase transition control is also achieved by patterned chemical doping. Researchers have demonstrated the phase transition from 2H to 1T phase in MoS_2 and WS_2 by Li ion intercalation [156]–[159]. To achieve local control, the target area is exposed to solution with Li ions while the rest of the area is protected through patterning a protection layer. In fig. 2b, Li ions penetrate into targeted 2H TMDC areas so the metastable 1T phase is transformed from 2H phase through electron donation from Li ions [158]. However, all above methods are demonstrated in few layers and difficult to utilize for device applications.

5.3 Electrostatic doping induced structural phase transition in 2D materials

Reversing the phase transition is limited to thermal annealing in all the methods demonstrated above. A dynamic electrical control of structural phases is necessary to create 2D information storage devices. In addition, such electrical control can reveal the fundamental role of the electron in the strong quasi-particle interaction during the phase transition, which has not been studied due to limited electrostatic doping levels in bulk crystals. Unlike three-dimensional bulk materials, 2D TMDs have large electrical tunability and theoretically enables a new mechanism of structural phase transition through electrostatic gating [34], [35], [160], [161]. Theoretical calculations show that monolayer $MoTe_2$ is an ideal material for the electronic control of the crystalline phases due to the small energy difference between the 2H and 1T' phases [150], [161]. Excess electrons occupy the lowest states above the Fermi level, which are 0.8 eV larger for 2H than for 1T' $MoTe_2$ (Fig. 5.2). Therefore, with high enough doping level, the extra electrons are expected to lift total energy of 2H phase sufficiently higher than that of 1T' to induce structural phase transition [161]. The calculated critical charge density for electrons (or holes) to trigger such phase transition is on the order of $10^{14}/cm^2$ (Fig. 5.3).

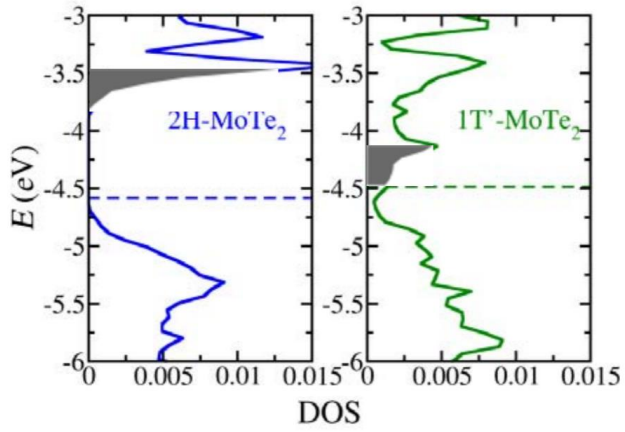

Figure 5.2: Electronic density of states of 2H and 1T' monolayer $MoTe_2$. The dashed lines label the Fermi level positions. Semiconducting 2H-MoTe2 has a band gap of 0.95 eV, and 1T'-MoTe2 has no band gap in calculation. The shaded regions depict the additional states occupied in negatively-charged monolayer. Reprinted with permission from [162]. Copyright Nature Publishing Group.

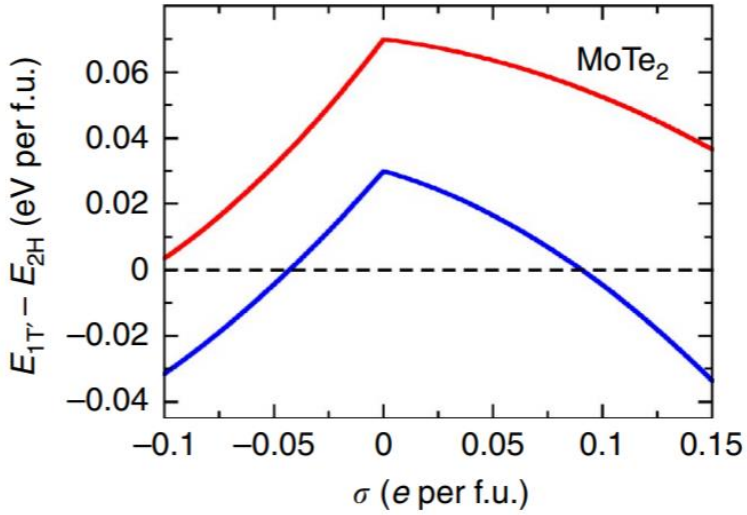

Figure 5.3: Phase boundary at constant charge in monolayer $MoTe_2$. Semiconducting 2H-$MoTe_2$ is a stable phase and semimetallic 1T′-$MoTe_2$ is metastable when the monolayer is charge neutral. However, 1T′-$MoTe_2$ is more thermodynamically favorable when the monolayer is charged beyond the positive or negative threshold values. Reprinted with permission from [162]. Copyright Nature Publishing Group.

5.4 Experimental observation of structural phase transition through Raman and SHG

To achieve such goal, monolayer $MoTe_2$ was chosen due to the smallest energy difference between two phases: 2H and 1T'. The control of structural phase transition from 2H monolayer $MoTe_2$ to 1T' phase is based on the platform of field-effect transistor (Fig. 5.4), by using ionic liquid (DEME-TFSI) as top gate, which usually could reach ultrahigher doping level 10^{14}-10^{15}/cm^2 [163].

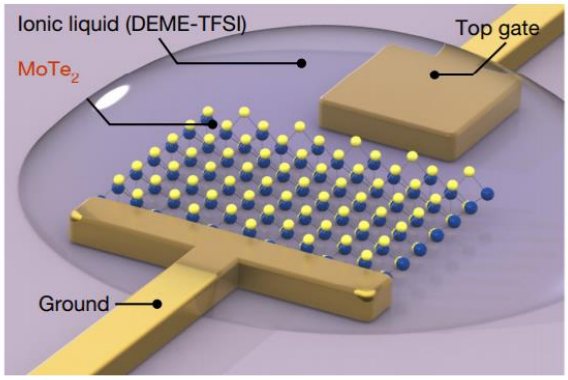

Figure 5.4: Schematics and measurement configuration. A monolayer of $MoTe_2$ is exfoliated onto a silicon wafer covered with a silicon oxide layer. The $MoTe_2$ monolayer is anchored by a ground indium/gold electrode; an isolated indium/gold pad nearby is the top-gate electrode, controlling the gate bias. A drop of ionic liquid (N,N-diethyl-N-(2-methoxyethyl)- N-methylammonium bis(trifluoromethylsulphonyl-imide), DEME-TFSI) covers the monolayer and the electrodes. This ionic liquid can manipulate the electron population in $MoTe_2$, resulting in a structural transition between the 2H and 1T′ phases. All devices were measured in vacuum and at 220 K.

Raman spectroscopy was applied to manifest the phases' evolution of the monolayer $MoTe_2$ when sweeping gate, shown from top to bottom in Fig. 5.5. The excitation wavelength is specifically chosen to be 633 nm, which gives the highest Raman intensity on monolayers [164]. When top gate is zero biased, the initial 2H monolayer $MoTe_2$, exfoliated from pristine crystal, shows two characteristic phonon modes: 171.7cm^{-1} (out of plane A_1' mode) and 233cm^{-1} (in plane E' mode) (Fig. 5.5). E_{2g} mode in figure 2b displays a sudden decrease passing V_g at 2.8V and after that it follows the decline until vanishing, indicating the absence of 2H phase at high voltage.

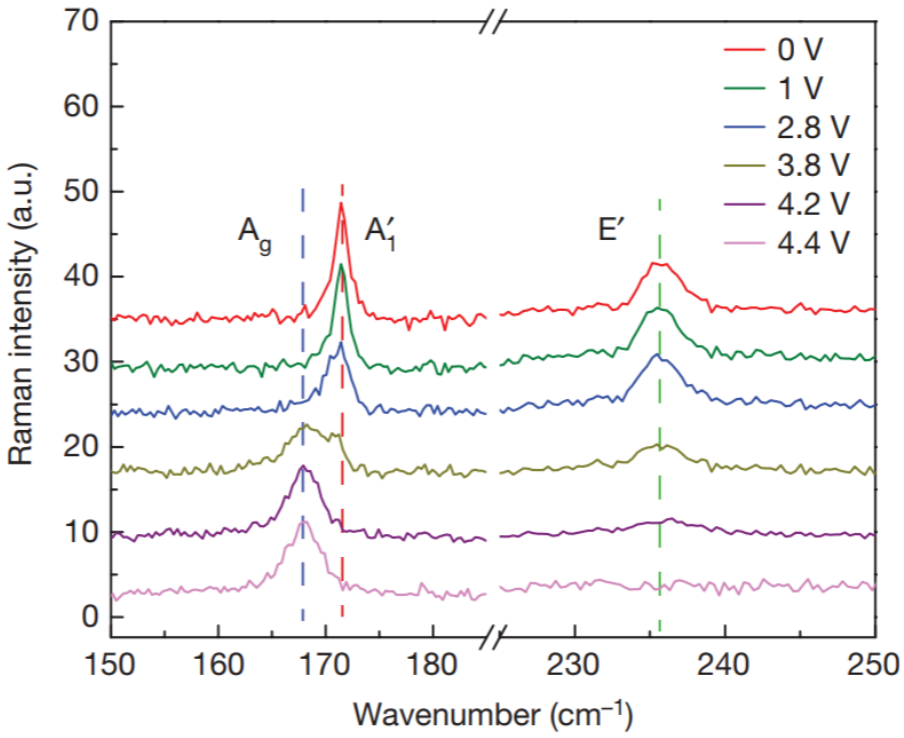

Figure 5.5: The 2H-1T' phase transition in monolayer $MoTe_2$ under bias. Representative Raman spectra before, during and after transition from the 2H to the 1T′ phase, as the bias changes from 0 V to 4.4 V. The characteristic Raman modes of the 2H phase, A_1' and E' (shown by the red and green dashed lines at 171.5 cm^{-1} and 236 cm^{-1}, respectively) gradually disappear, as the A_g mode of the 1T′ phase appears (167.5 cm^{-1}; blue dashed line).

Meanwhile, Raman spectra in figure 5.5 not only contains the falloff of A_1' mode of 2H phase, following the same trend in E' mode, but also exhibits a rising new peak, at 167.5 cm^{-1}. This new peak, corresponding to the characteristic A_g mode of 1T' phase [165] (Fig. 5.6), verifies the phase transition of monolayer $MoTe_2$. And the power of excitation light, limited under 1mW/μm^2, eliminates the possibility that 1T' is induced through laser irradiation.

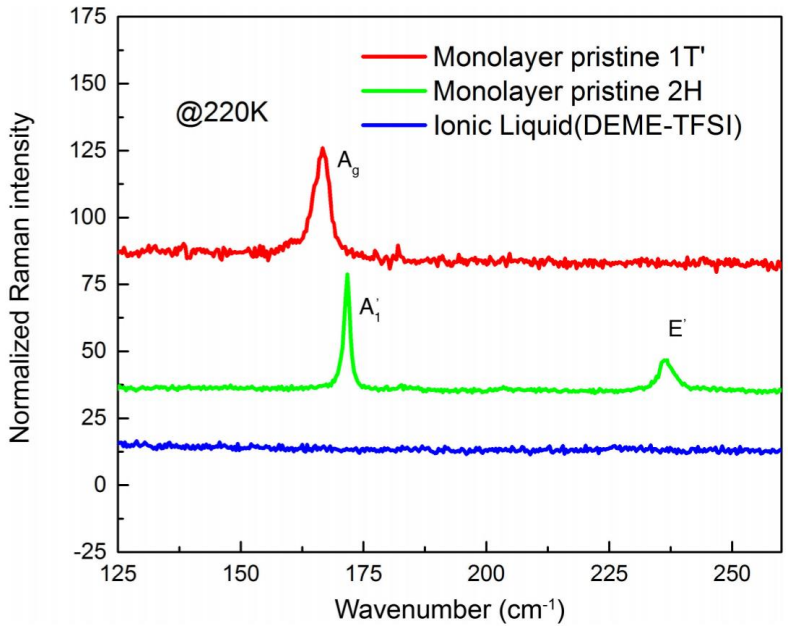

Figure 5.6: Raman features of pristine 2H-and 1T'-phase. Raman spectra for the 2H and 1T' phases of monolayer $MoTe_2$ are plotted in green and red, respectively. The Raman modes at 171.5 cm^{-1} and 236 cm^{-1} are the A_1' and E' oscillation modes, belonging to the 2H phase. Excited by the same wavelength (632.8 nm), the 1T' monolayer has just one dominant mode, at 166.8 cm^{-1}. The blue curve, from bare ionic liquid, shows no Raman modes and so acts as a clear and flat background in all Raman measurements.

On the other hand, a spatial SHG scan mapping shows such gate induced phase transition is global over the whole flake and leads to substantial crystal symmetry change. Without bias, a strip of monolayer was scanned (Fig. 5.7a). The SHG intensity shows some extent of variation over the flake, which is suspected due to local electron charging [166]. Then by applying forward bias up to 4V, a series of gate dependent SHG scan mappings are obtained and shown in figure 5.7. When the gate bias tunes up, SHG intensity gradually increases due to absorption profile modification by doping in 2H phase. Further increasing bias from 2 to 4V, SHG intensity shows sharp decrease about one order. By carefully excluding doping induced absorption change in 2H phase, such drop mainly attributes to transition from 2H phase to 1T' phase which preserves inversion symmetry. Note that, the SHG mappings indicate a near uniform and global transition, scaling up to micron meter, controlled by electrostatic gate. Additional evidences including polarized Raman anisotropy, SHG gate-dependent hysteresis and other control experiments to exclude thermal or strain origin for observed phase transition are elaborated in my published work [59].

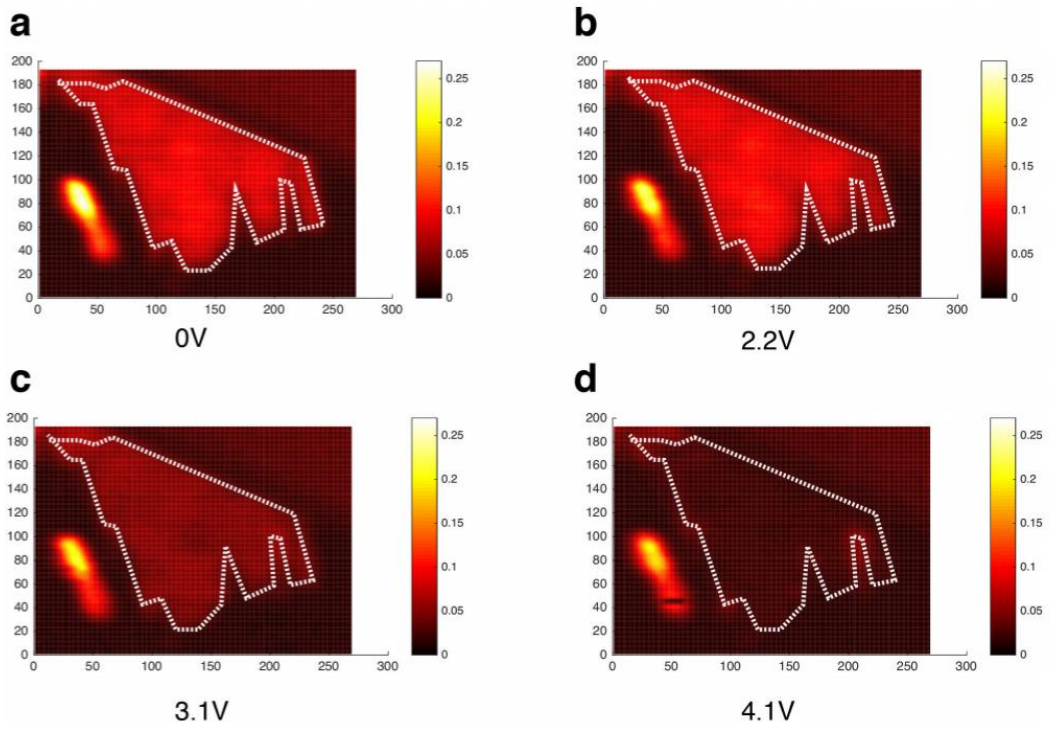

Figure 5.7: SHG mapping at several typical voltage biases. **a–d,** these biases correspond to before (0 V and 2.2 V; **a, b**), during (3.1 V; **c**) and after (4.1 V; **d**) phase transition.

5.5 Conclusion

In conclusion, we have demonstrated reversible electrical manipulation of structural phase transition in a typical 2D material: monolayer $MoTe_2$. Our electrical scheme of controlling phase transition provides a versatile platform to study fundamental physics on ordering interplay and novel topological phases. In addition, the observed large hysteresis window and modulation depth unravel the potential of developing 2D memory and reconfigurable devices [148].

6 Summary and Outlook

This dissertation presented experimental investigation in how crystal symmetry and symmetry breaking substantially influence on optoelectronic properties of 2D valleytronic materials and 2D polar structural phases.

It includes the discovery of optical selection for nonlinear optical process in monolayer WS_2 with both valley and excitonic degree of freedom into account [167]. The discovery of this new optical selection rule in a valleytronic 2D system reveal the important role of crystal symmetry and excitonic fine structures in nonlinear optical process. It also establishes a foundation for the control of optical transitions that will be crucial for valley optoelectronic device applications such as 2D valley-polarized THz sources with 2*p*–1*s* transitions, optical switches, and coherent control for quantum computing. This dissertation also covers the first demonstration of electrical valley generation through ferromagnetic spin injection [83], which validifies the unique spin-valley relationship and opens the door towards a new paradigm of electronics that manifests all three DOFs—charge, spin, and valley—for information processing.

On the other hand, this dissertation also demonstrates the exploration on novel polar structural ordering in 2D crystals such as monolayer MoSSe and ferroelectric In_2Se_3. The mirror symmetry breaking allows spontaneous polarization in these crystals, which show strong SHG signal from out-of-plane dipoles. They reveal the potentials for Rashba spin physics, new domain kinetics and memory devices down to atomically thin level [57]. Finally, the first demonstration of electrostatic doping induced structural phase transition in monolayer $MoTe_2$ not only show the capability for dynamic engineering of crystal symmetry at 2D limit but highlight the important role of electron doping in controlling different phases in low-dimensional system [59]. The common feature for such system is weakly electrostatic screening, whose quasi-particle interactions and following phase diagram are very sensitive to external stimuli such as electrical doping, mechanical strain.

In the rest of the chapter, I point out some current challenges and attempt to propose some future directions regarding the establishment of valleytronics and phase transition in quantum materials closely associated with crystal symmetry manipulation.

6.1 Future valleytronics

Despite the rapid research progress on valley degree of freedom induced by inversion symmetry breaking, there are still significant issues that call for future efforts to make valleytronics become a practical industrial application.

Firstly, longer valley carrier lifetime is in need. In early studies, optical excitation can easily generate valley exciton or trions, however, their valley lifetimes are at most on the order of tens of ps [168], [169]. The main roadblock is intervalley scattering

mediated by e-h exchange interaction [79]. Recently, two ways are utilized to bypass this limit. One is based on heavily doped monolayer in which residue free carrier shows nanosecond spin lifetime and potential longer valley lifetime at liquid helium temperature [170]. The other one takes advantage of van der Waals heterostructure. In such system, the optically excited exciton goes through charge transfer process, ending up with electron in one layer and hole in the other layer. The e-h exchange interaction is largely suppressed due to significantly reduced electron and hole wavefunction overlap. Indeed, valley lifetime of such interlayer exciton is about tens of nanoseconds at low temperature, much longer than that of intralayer exciton studied before [171]. Ultralong lifetime on the order of μs has been reported with both heterostructure and heavily doping nature [172]. Valleytronic research is enjoying a revival by these recent reports. But the field still needs to achieve longer valley lifetime at room temperature, simply based on the desire to have more operation cycles and more feasible for applications.

Another interesting point is about how to manipulate intervalley scattering for longer valley lifetime and valley operation. As mentioned above, intervalley scattering alone has been long thought as killing factor for long valley lifetime. However, the nature of intervalley scattering based on electron-hole exchange, electron-phonon interaction and electron-defect interaction is far from crystal clear. For instance, the coherent property of this scattering process is largely unexplored, let alone using quantum coherent process to control intervalley scattering for long valley lifetime or valley operation. Furthermore, crystal symmetry engineering may be another strategy to control intervalley scattering.

Besides, valley manipulation devices are in need to perform logic gate functions. So far, several electronic and optical methods are established to initialize, transport and readout valley polarization including circular polarization excitation, valley Hall effect, spin injection, magnetoelectric effect. However, for a fully functional valleytronic platform, it also requires logic gates to operate valley information. Corresponding devices include valley filter, valley modulator, valley multiplier and valley storage.

Meanwhile, it is worthwhile to expand valley degree of freedom to other quasiparticles beyond electron for new functionality. For instance, optical manipulation of the excitonic fine structure and utilizing spin and valley has potential in quantum information. The strong-coupling in exciton-polaritons may enable the valley Bose Einstein condensation and valley superfluid behavior in 2D systems [173]. More recently, the chiral valley phonon has been discovered in monolayer WSe_2 [174]. The broken inversion symmetry of the WSe_2 lattice lifts the degeneracy of clockwise and counterclockwise phonon modes at the same valley in momentum space. While in another valley, the energy degenerate phonon rotation mode has opposite chirality. Such chiral valley phonons could be used to control the electron-phonon coupling and achieve the phonon-driven topological states.

6.2 Symmetry engineering and quantum phase transition in 2D materials

Atomically thin-layered materials provide a rich platform for exploring novel 2D phase transitions and enables the development of diverse devices based on these materials. The strong spatial confinement, weak dielectric screening and large spin-orbit coupling in such 2D system reveal unique physics such as enhanced electron-phonon coupling in charge density waves and Ising pairing in superconductivity. The 2D nature makes the materials susceptible to interfaces and electrostatic doping, enabling the record-high transition temperature in Fe-based superconductors [175], and inspiring new mechanisms to drive structural change in crystal configuration [59], [161].

Several future directions can be envisioned. For example, artificial heterostructures assembled by layer stacking can provide new crystal symmetry breaking and functionality. Moreover, independent electrical access to individual layer in a heterostructure is realized, which provides more degree of freedom to control the interlayer interaction and the crystal symmetry of individual layers. More recently, the relative crystal orientation angle is found to be a key to achieve Mott-like insulator and superconductivity in bilayer stacking graphene systems. This bilayer graphene system stacked with a magic angle (~1.08°) is expected to a more feasible platform to clarify high-temperature superconductivity mechanism compared with conventional cuprates. Further explorations on ordering competition in such system and how the heterostructure crystal symmetry affect such process are in demand.

In addition, as theoretically envisioned [42], vortex-antivortex pair formation play a very important role in 2D magnetic and superconducting systems. The presence of such pairs in layered materials has been confirmed by scaling law analysis based on macroscopic current-voltage characteristic measurements[112], but it only shows an average effect over the whole crystal and long periods. It is quite interesting to directly visualize and study vortex dynamics at the microscopic spatial range and ultrafast time scale.

Finally, beyond classical phase transition in 2D systems at finite temperature, the quantum fluctuation can also drive the system from order to disorder with novel physics at the vicinity of transition point [178], if $k_B T < \hbar\omega_c$ (ω_c is the characteristic frequency for quantum oscillation mode). The large tunablity is a significant advantage in the observations of quantum phase transitions in 2D layered materials, as the transition point needs to be approached by tuning external parameters such as magnetic field and doping level. More interestingly, it has been theoretically shown that such quantum phase transitions in two dimensions acts similar to classical phase transition in 2 + Z dimension [179], which is known as quantum-classical mapping. The dynamic critical exponent Z can be integer or even fraction number depending on the relationship between correlation length ξ and correlation time t ($t \sim \xi^Z$). Research on quantum phase transitions in layered materials is still in its infancy [122], [180], and future efforts will explore the unique properties such as quantum-classical mapping in 2D layered materials.

Bibliography

[1] S. K. Chatterjee, *Crystallography and the World of Symmetry*. 2008.

[2] U. Englert, "Symmetry Relationships between Crystal Structures. Applications of Crystallographic Group Theory in Crystal Chemistry. By Ulrich Müller.," *Angew. Chemie Int. Ed.*, vol. 52, no. 46, pp. 11973–11973, 2013.

[3] S. Sternberg, *Group theory and physics*, vol. 5, no. 2. 1994.

[4] G. Blatter, M. V. Feigel'Man, V. B. Geshkenbein, A. I. Larkin, and V. M. Vinokur, "Vortices in high-temperature superconductors," *Rev. Mod. Phys.*, vol. 66, no. 4, pp. 1125–1388, 1994.

[5] B. Sipos, A. F. Kusmartseva, A. Akrap, H. Berger, L. Forró, and E. Tutis, "From Mott state to superconductivity in 1T-TaS2.," *Nat. Mater.*, vol. 7, no. 12, pp. 960–5, Dec. 2008.

[6] T. Dietl, "A ten-year perspective on dilute magnetic semiconductors and oxides," *Nature Materials*, vol. 9, no. 12. pp. 965–974, 2010.

[7] D. N. Basov, R. D. Averitt, and D. Hsieh, "Towards properties on demand in quantum materials," *Nat. Mater.*, vol. 16, no. 11, pp. 1077–1088, 2017.

[8] T. Senthil, "Symmetry-Protected Topological Phases of Quantum Matter," *Annu. Rev. Condens. Matter Phys.*, vol. 6, no. 1, pp. 299–324, 2015.

[9] X. Xu, W. Yao, D. Xiao, and T. F. Heinz, "Spin and pseudospins in layered transition metal dichalcogenides," *Nature Physics*, vol. 10, no. 5. pp. 343–350, 2014.

[10] R. W. Boyd, *Nonlinear Optics*, vol. 5, no. 10. 2003.

[11] J. Watson and F. Crick, "Molecular structure of nucleic acids," *Nature.*, vol. 171, no. 4356, pp. 737–8, 1953.

[12] K. S. Novoselov, A. K. Geim, S. V Morozov, D. Jiang, Y. Zhang, S. V Dubonos, I. V Grigorieva, and A. A. Firsov, "Electric field effect in atomically thin carbon films.," *Science*, vol. 306, no. 5696, pp. 666–9, 2004.

[13] A. Splendiani, L. Sun, Y. Zhang, T. Li, J. Kim, C.-Y. Chim, G. Galli, and F. Wang, "Emerging Photoluminescence in Monolayer MoS2," 2010.

[14] K. F. Mak, C. Lee, J. Hone, J. Shan, and T. F. Heinz, "Atomically thin MoS_2: a new direct-gap semiconductor.," *Phys. Rev. Lett.*, vol. 105, no. 13, p. 136805, Sep. 2010.

[15] F. Xia, H. Wang, and Y. Jia, "Rediscovering black phosphorus as an anisotropic layered material for optoelectronics and electronics," *Nat. Commun.*, vol. 5, 2014.

[16] B. Anasori, M. R. Lukatskaya, and Y. Gogotsi, "2D metal carbides and nitrides (MXenes) for energy storage," *Nature Reviews Materials*, vol. 2, no. 2. 2017.

[17] W. Ding, J. Zhu, Z. Wang, Y. Gao, D. Xiao, Y. Gu, Z. Zhang, and W. Zhu, "Prediction of intrinsic two-dimensional ferroelectrics in In2Se3 and other III2-VI3 van der Waals

materials," *Nat. Commun.*, vol. 8, p. 14956, 2017.

[18] S. Manzeli, D. Ovchinnikov, D. Pasquier, O. V. Yazyev, and A. Kis, "2D transition metal dichalcogenides," *Nature Reviews Materials*, vol. 2. 2017.

[19] X. Qian, J. Liu, L. Fu, and J. Li, "Quantum spin Hall effect in two-dimensional transition metal dichalcogenides," *Science (80-.).*, vol. 346, no. 6215, pp. 1344–7, Dec. 2014.

[20] K.-A. N. Duerloo, Y. Li, and E. J. Reed, "Structural phase transitions in two-dimensional Mo- and W-dichalcogenide monolayers," *Nat. Commun.*, vol. 5, Jul. 2014.

[21] K. Komider, J. W. González, and J. Fernández-Rossier, "Large spin splitting in the conduction band of transition metal dichalcogenide monolayers," *Phys. Rev. B - Condens. Matter Mater. Phys.*, vol. 88, no. 24, 2013.

[22] Z. Ye, T. Cao, K. O'Brien, H. Zhu, X. Yin, Y. Wang, S. G. Louie, and X. Zhang, "Probing excitonic dark states in single-layer tungsten disulphide," *Nature*, vol. 513, no. 7517, pp. 214–218, Aug. 2014.

[23] B. Zhu, X. Chen, and X. Cui, "Exciton Binding Energy of Monolayer WS2," *Sci. Rep.*, vol. 5, p. 9218, 2015.

[24] A. Chernikov, T. C. Berkelbach, H. M. Hill, A. Rigosi, Y. Li, O. B. Aslan, D. R. Reichman, M. S. Hybertsen, and T. F. Heinz, "Exciton Binding Energy and Nonhydrogenic Rydberg Series in Monolayer WS 2," *Phys. Rev. Lett.*, vol. 113, no. 7, p. 076802, Aug. 2014.

[25] K. F. Mak, K. He, J. Shan, and T. F. Heinz, "Control of valley polarization in monolayer MoS2 by optical helicity," *Nat. Nanotechnol.*, vol. 7, no. 8, pp. 494–498, 2012.

[26] H. Zeng, J. Dai, W. Yao, D. Xiao, and X. Cui, "Valley polarization in MoS2 monolayers by optical pumping," *Nat. Nanotechnol.*, vol. 7, no. 8, pp. 490–493, Jun. 2012.

[27] T. Cao, G. Wang, W. Han, H. Ye, C. Zhu, J. Shi, Q. Niu, P. Tan, E. Wang, B. Liu, and J. Feng, "Valley-selective circular dichroism of monolayer molybdenum disulphide.," *Nat. Commun.*, vol. 3, no. May, p. 887, Jun. 2012.

[28] J. R. Schaibley, H. Yu, G. Clark, P. Rivera, J. S. Ross, K. L. Seyler, W. Yao, and X. Xu, "Valleytronics in 2D materials," *Nature Reviews Materials*, vol. 1, no. 11. 2016.

[29] S. K. Kailasa, K. H. Cheng, and H. F. Wu, "Semiconductor nanomaterials-based fluorescence spectroscopic and matrix-assisted laser desorption/ionization (MALDI) mass spectrometric approaches to proteome analysis," *Materials*, vol. 6, no. 12. pp. 5763–5795, 2013.

[30] Y. Saito, Y. Nakamura, M. S. Bahramy, Y. Kohama, J. Ye, Y. Kasahara, Y. Nakagawa, M. Onga, M. Tokunaga, T. Nojima, Y. Yanase, and Y. Iwasa, "Superconductivity protected by spin–valley locking in ion-gated MoS2," *Nat. Phys.*, vol. 12, no. 2, pp. 144–149, Dec. 2015.

[31] J. M. Lu, O. Zheliuk, I. Leermakers, N. F. Q. Yuan, U. Zeitler, K. T. Law, and J. T. Ye, "Evidence for two-dimensional Ising superconductivity in gated MoS_2.," *Science*, vol. 350, no. 6266, pp. 1353–7, Dec. 2015.

[32] X. Xi, Z. Wang, W. Zhao, J.-H. Park, K. T. Law, H. Berger, L. Forró, J. Shan, and K. F. Mak, "Ising pairing in superconducting NbSe2 atomic layers," *Nat. Phys.*, vol. 12, no. 2,

pp. 139–143, Nov. 2015.

[33] D. A. B. Miller and T. B. Laboratories, “Optical Physics of Quantum Wells,” *Quantum Dyn. Simple Syst.*, pp. 239–266, 1996.

[34] K. F. Mak, K. He, C. Lee, G. H. Lee, J. Hone, T. F. Heinz, and J. Shan, “Tightly bound trions in monolayer MoS2.,” *Nat. Mater.*, vol. 12, no. 3, pp. 207–11, 2013.

[35] J. S. Ross, S. Wu, H. Yu, N. J. Ghimire, A. M. Jones, G. Aivazian, J. Yan, D. G. Mandrus, D. Xiao, W. Yao, and X. Xu, “Electrical control of neutral and charged excitons in a monolayer semiconductor.,” *Nat. Commun.*, vol. 4, p. 1474, 2013.

[36] K. L. Seyler, J. R. Schaibley, P. Gong, P. Rivera, A. M. Jones, S. Wu, J. Yan, D. G. Mandrus, W. Yao, and X. Xu, “Electrical control of second-harmonic generation in a WSe2 monolayer transistor,” *Nat. Nanotechnol.*, vol. 10, no. 5, pp. 407–411, 2015.

[37] J. T. Ye, Y. J. Zhang, R. Akashi, M. S. Bahramy, R. Arita, and Y. Iwasa, “Superconducting Dome in a Gate-Tuned Band Insulator,” *Science (80-.).*, vol. 338, no. 6111, pp. 1193–1196, 2012.

[38] P. A. Lee, N. Nagaosa, and X. G. Wen, “Doping a Mott insulator: Physics of high-temperature superconductivity,” *Rev. Mod. Phys.*, vol. 78, no. 1, 2006.

[39] Y. Takabayashi, A. Y. Ganin, P. Jeglič, D. Arčon, T. Takano, Y. Iwasa, Y. Ohishi, M. Takata, N. Takeshita, K. Prassides, and M. J. Rosseinsky, “The Disorder-Free Non-BCS Superconductor Cs3C60 Emerges from an Antiferromagnetic Insulator Parent State,” *Science (80-.).*, vol. 323, no. 5921, pp. 1585–1590, 2009.

[40] D. Costanzo, S. Jo, H. Berger, and A. F. Morpurgo, “Gate-induced Superconductivity in atomically thin MoS2 crystals,” *Nat. Nanotechnol.*, vol. 11, no. January, pp. 339–344, 2015.

[41] V. L. Berezinskii, “Destruction of long-range order in one-dimensional and two-dimensional systems with a continuous symmetry group. II. Quantum systems,” *Zhurnal Eksp. i Teor. Fiz.*, vol. 61, no. 3, pp. 1144–1156, 1971.

[42] J. M. Kosterlitz, D. J. Thouless, A. M. and S. I. A, A. B. J. and W. T. A, A. P. W. and Y. G, Y. G. and H. D. R. Anderson P W, B. V L, B. V L, Y. L. C. and S. J. B. Chester M, F. J, de G. P. G, H. E. H. and H. P. C, H. J. A. and D. J. G, H. P. C, J. J. D, K. J. M. and T. D. J, L. L. D. and L. E. M, M. N. D, M. N. D. and W. H, M. M. A, N. F. R. N, P. J, P. R. E, P. R. E, P. O. and O. L, S. F, S. H. E, S. H. E. and K. T. A, B. D. F. and T. A. L. Symonds A J, T. D. J, and W. F, “Ordering, metastability and phase transitions in two-dimensional systems,” *J. Phys. C Solid State Phys.*, vol. 6, no. 7, pp. 1181–1203, 1973.

[43] E. J. G. Santos and E. Kaxiras, “Electrically Driven Tuning of the Dielectric Constant in MoS 2 Layers,” *ACS Nano*, vol. 7, no. 12, pp. 10741–10746, 2013.

[44] X. Chen, Z. Wu, S. Xu, L. Wang, R. Huang, Y. Han, W. Ye, W. Xiong, T. Han, G. Long, Y. Wang, Y. He, Y. Cai, P. Sheng, and N. Wang, “Probing the Electron States and Metal-Insulator Transition Mechanisms in Atomically Thin MoS2 Based on Vertical Heterostructures,” *Nat. Commun.*, vol. 6, p. 6088, 2014.

[45] S. Lebègue and O. Eriksson, “Electronic structure of two-dimensional crystals from ab initio theory,” *Phys. Rev. B - Condens. Matter Mater. Phys.*, vol. 79, no. 11, 2009.

[46] J. K. Ellis, M. J. Lucero, and G. E. Scuseria, “The indirect to direct band gap transition in

multilayered MoS2 as predicted by screened hybrid density functional theory," *Appl. Phys. Lett.*, vol. 99, no. 26, p. 261908, 2011.

[47] Y. Ge and A. Y. Liu, "Phonon-mediated superconductivity in electron-doped single-layer MoS 2: A first-principles prediction," *Phys. Rev. B - Condens. Matter Mater. Phys.*, vol. 87, no. 24, 2013.

[48] D. Akinwande, N. Petrone, and J. Hone, "Two-dimensional flexible nanoelectronics.," *Nat. Commun.*, vol. 5, p. 5678, 2014.

[49] K. He, C. Poole, K. F. Mak, and J. Shan, "Experimental demonstration of continuous electronic structure tuning via strain in atomically thin MoS2," *Nano Lett.*, vol. 13, no. 6, pp. 2931–2936, 2013.

[50] H. J. Conley, B. Wang, J. I. Ziegler, R. F. Haglund, S. T. Pantelides, and K. I. Bolotin, "Bandgap engineering of strained monolayer and bilayer MoS2," *Nano Lett.*, vol. 13, no. 8, pp. 3626–3630, 2013.

[51] A. K. Geim and I. V Grigorieva, "Van der Waals heterostructures.," *Nature*, vol. 499, no. 7459, pp. 419–25, Jul. 2013.

[52] X. Wang and F. Xia, "Van der Waals heterostructures: Stacked 2D materials shed light," *Nat. Mater.*, vol. 14, no. March, pp. 264–265, 2015.

[53] Y. Liu, N. O. Weiss, X. Duan, H.-C. Cheng, Y. Huang, and D. Xiangfeng, "Van der Waals heterostructures and devices," *Nat. Rev. Mater.*, vol. 490, p. 16042, 2016.

[54] H. Wang, H. Yuan, S. Sae Hong, Y. Li, and Y. Cui, "Physical and chemical tuning of two-dimensional transition metal dichalcogenides.," *Chem. Soc. Rev.*, vol. 44, no. 9, pp. 2664–80, 2015.

[55] J. Xiao, Z. Ye, Y. Wang, H. Zhu, Y. Wang, and X. Zhang, "Nonlinear optical selection rule based on valley-exciton locking in monolayer ws2," *Light Sci. Appl.*, vol. 4, no. 12, p. e366, 2015.

[56] Y. Ye, J. Xiao, H. Wang, Z. Ye, H. Zhu, M. Zhao, Y. Wang, J. Zhao, X. Yin, and X. Zhang, "Electrical generation and control of the valley carriers in a monolayer transition metal dichalcogenide," *Nat. Nanotechnol.*, vol. 11, no. 7, pp. 598–602, Apr. 2016.

[57] A.-Y. Lu, H. Zhu, J. Xiao, C.-P. Chuu, Y. Han, M.-H. Chiu, C.-C. Cheng, C.-W. Yang, K.-H. Wei, Y. Yang, Y. Wang, D. Sokaras, D. Nordlund, P. Yang, D. A. Muller, M.-Y. Chou, X. Zhang, and L.-J. Li, "Janus monolayers of idestransition metal dichalcogenides," *Nat. Nanotechnol.*, pp. 1–29, 2017.

[58] J. Xiao, H. Zhu, Y. Wang, W. Feng, C. Hu, A. Dasgupta, Y. Han, Y. Wang, D. A. Muller, L. W. Martin, P. Hu, and X. Zhang, "Intrinsic two-dimensional ferroelectricity with dipole locking," *Phys. Rev. Lett.*, accepted, 2018.

[59] Y. Wang, J. Xiao, H. Zhu, Y. Li, Y. Alsaid, K. Y. Fong, Y. Zhou, S. Wang, W. Shi, Y. Wang, A. Zettl, E. J. Reed, and X. Zhang, "Structural phase transition in monolayer MoTe2 driven by electrostatic doping," *Nature*, 2017.

[60] D. J. Hilton and C. L. Tang, "Optical Orientation and Femtosecond Relaxation of Spin-Polarized Holes in GaAs," *Phys. Rev. Lett.*, vol. 89, no. 14, 2002.

[61] B. D. Gerardot, D. Brunner, P. a Dalgarno, P. Ohberg, S. Seidl, M. Kroner, K. Karrai, N.

G. Stoltz, P. M. Petroff, and R. J. Warburton, “Optical pumping of a single hole spin in a quantum dot.,” *Nature*, vol. 451, no. 7177, pp. 441–444, 2008.

[62] W. Yao, D. Xiao, and Q. Niu, “Valley-dependent optoelectronics from inversion symmetry breaking,” *Phys. Rev. B - Condens. Matter Mater. Phys.*, vol. 77, no. 23, 2008.

[63] D. Xiao, W. Yao, and Q. Niu, “Valley-contrasting physics in graphene: Magnetic moment and topological transport,” *Phys. Rev. Lett.*, vol. 99, no. 23, 2007.

[64] H. Zeng, G. Bin Liu, J. Dai, Y. Yan, B. Zhu, R. He, L. Xie, S. Xu, X. Chen, W. Yao, and X. Cui, “Optical signature of symmetry variations and spin-valley coupling in atomically thin tungsten dichalcogenides,” *Sci. Rep.*, vol. 3, 2013.

[65] K. F. Mak, K. He, J. Shan, and T. F. Heinz, “Control of valley polarization in monolayer MoS2by optical helicity,” *Nat. Nanotechnol.*, vol. 7, no. 8, pp. 494–498, 2012.

[66] D. Xiao, G. Bin Liu, W. Feng, X. Xu, and W. Yao, “Coupled spin and valley physics in monolayers of MoS 2 and other group-VI dichalcogenides,” *Phys. Rev. Lett.*, vol. 108, no. 19, p. 196802, May 2012.

[67] P. J. Campagnola and L. M. Loew, “Second-harmonic imaging microscopy for visualizing biomolecular arrays in cells, tissues and organisms,” *Nature Biotechnology*, vol. 21, no. 11. pp. 1356–1360, 2003.

[68] X. Yin, Z. Ye, D. A. Chenet, Y. Ye, K. O’Brien, J. C. Hone, and X. Zhang, “Edge nonlinear optics on a MoS2 atomic monolayer,” *Science (80-.).*, vol. 344, no. 6183, pp. 488–490, 2014.

[69] S. A. Denev, T. T. A. Lummen, E. Barnes, A. Kumar, and V. Gopalan, “Probing ferroelectrics using optical second harmonic generation,” *J. Am. Ceram. Soc.*, vol. 94, no. 9, pp. 2699–2727, 2011.

[70] C. Kittel, *Introduction to Solid State Physics*, vol. 8th editio. 2004.

[71] B. Zaslow and M. E. Zandler, “Two-Dimensional Analog to the Hydrogen Atom,” *Am. J. Phys.*, vol. 35, no. 12, pp. 1118–1119, 1967.

[72] D. Y. Qiu, F. H. da Jornada, and S. G. Louie, “Optical spectrum of MoS2: many-body effects and diversity of exciton states.,” *Phys. Rev. Lett.*, vol. 111, no. 21, p. 216805, Nov. 2013.

[73] H. J. Simon and N. Bloembergen, “Second-harmonic light generation in crystals with natural optical activity,” *Phys. Rev.*, vol. 171, no. 3, pp. 1104–1114, 1968.

[74] N. Bloembergen, “Conservation laws in nonlinear optics*,” *J. Opt. Soc. Am.*, vol. 70, no. 12, p. 1429, 1980.

[75] G. Kioseoglou, A. T. Hanbicki, M. Currie, A. L. Friedman, D. Gunlycke, and B. T. Jonker, “Valley polarization and intervalley scattering in monolayer MoS2,” *Appl. Phys. Lett.*, vol. 101, no. 22, 2012.

[76] S. D’Auria, M. Rossi, J. Malicka, Z. Gryczynski, and I. Gryczynski, *Topics in Fluorescence Spectroscopy*, vol. 8. 2003.

[77] H. Shi, R. Yan, S. Bertolazzi, J. Brivio, B. Gao, A. Kis, D. Jena, H. G. Xing, and L. Huang, “Exciton dynamics in suspended monolayer and few-layer MoS22D crystals,” *ACS Nano*, vol. 7, no. 2, pp. 1072–1080, 2013.

[78] N. Kumar, Q. Cui, F. Ceballos, D. He, Y. Wang, and H. Zhao, "Exciton-exciton annihilation in MoSe 2 monolayers," *Phys. Rev. B - Condens. Matter Mater. Phys.*, vol. 89, no. 12, 2014.

[79] T. Yu and M. W. Wu, "Valley depolarization due to intervalley and intravalley electron-hole exchange interactions in monolayer MoS2," *Phys. Rev. B - Condens. Matter Mater. Phys.*, vol. 89, no. 20, 2014.

[80] G. Slavcheva and A. V. Kavokin, "Polarization selection rules in exciton-based terahertz lasers," *Phys. Rev. B - Condens. Matter Mater. Phys.*, vol. 88, no. 8, 2013.

[81] M. Fleischhauer, A. Imamoglu, and J. P. Marangos, "Electromagnetically induced transparency: Optics in coherent media," *Rev. Mod. Phys.*, vol. 77, no. 2, pp. 633–673, 2005.

[82] Y. Silberberg, "Quantum Coherent Control for Nonlinear Spectroscopy and Microscopy," *Annu. Rev. Phys. Chem.*, vol. 60, no. 1, pp. 277–292, 2009.

[83] Y. Ye, J. Xiao, H. Wang, Z. Ye, H. Zhu, M. Zhao, Y. Wang, J. Zhao, X. Yin, and X. Zhang, "Electrical generation and control of the valley carriers in a monolayer transition metal dichalcogenide," *Nat. Nanotechnol.*, no. April, pp. 1–6, 2016.

[84] J. Fabian, A. Matos-Abiague, C. Ertler, P. Stano, and I. Žutić, "Semiconductor spintronics," *Acta Phys. Slovaca. Rev. Tutorials*, vol. 57, no. 4–5, 2007.

[85] Y. Ohno, D. K. Young, B. Beschoten, F. Matsukura, H. Ohno, and D. D. Awschalom, "Electrical spin injection in a ferromagnetic semiconductor heterostructure," *Nature*, vol. 402, no. 6763, pp. 790–792, 1999.

[86] T. Dietl and H. Ohno, "Dilute ferromagnetic semiconductors: Physics and spintronic structures," *Rev. Mod. Phys.*, vol. 86, no. 1, pp. 187–251, 2014.

[87] J. S. Ross, P. Klement, A. M. Jones, N. J. Ghimire, J. Yan, D. G. Mandrus, T. Taniguchi, K. Watanabe, K. Kitamura, W. Yao, D. H. Cobden, and X. Xu, "Electrically tunable excitonic light-emitting diodes based on monolayer WSe2 p-n junctions.," *Nat. Nanotechnol.*, vol. 9, no. 4, pp. 268–72, Mar. 2014.

[88] B. W. H. Baugher, H. O. H. Churchill, Y. Yang, and P. Jarillo-Herrero, "Optoelectronic devices based on electrically tunable p-n diodes in a monolayer dichalcogenide.," *Nat. Nanotechnol.*, vol. 9, no. 4, pp. 262–7, 2014.

[89] Y. J. Zhang, T. Oka, R. Suzuki, J. T. Ye, and Y. Iwasa, "Electrically Switchable Chiral Light-Emitting Transistor," *Science (80-.).*, vol. 344, no. 6185, pp. 725–728, May 2014.

[90] T. Cheiwchanchamnangij and W. R. L. Lambrecht, "Quasiparticle band structure calculation of monolayer, bilayer, and bulk MoS 2," *Phys. Rev. B - Condens. Matter Mater. Phys.*, vol. 85, no. 20, 2012.

[91] B. Zhu, H. Zeng, J. Dai, Z. Gong, and X. Cui, "Anomalously robust valley polarization and valley coherence in bilayer WS2," *Proc. Natl. Acad. Sci.*, vol. 111, no. 32, pp. 11606–11611, 2014.

[92] S. Ghosh and P. Bhattacharya, "Surface-emitting spin-polarized In0.4Ga0.6As/GaAs quantum-dot light-emitting diode," *Appl. Phys. Lett.*, vol. 80, no. 4, pp. 658–660, 2002.

[93] J. Lee, Z. Wang, H. Xie, K. F. Mak, and J. Shan, "Valley magnetoelectricity in single-

layer MoS 2," *Nat. Mater.*, vol. 16, no. 9, pp. 887–891, 2017.

[94] A. Nouailhat, *An introduction to nanoscience and nanotechnology*. 2010.

[95] L. W. Martin and A. M. Rappe, "Thin-film ferroelectric materials and their applications," *Nat. Rev. Mater.*, vol. 2, p. 16087, 2016.

[96] J. Yan, M. Bloom, S. C. Bae, E. Luijten, and S. Granick, "Linking synchronization to self-assembly using magnetic Janus colloids," *Nature*, vol. 491, no. 7425, pp. 578–581, 2012.

[97] P. W. Tasker, "The stability of ionic crystal surfaces," *J. Phys. C Solid State Phys.*, vol. 12, no. 22, pp. 4977–4984, 1979.

[98] C. H. Bates, W. B. White, and R. Roy, "New High-Pressure Polymorph of Zinc Oxide," *Science (80-.).*, vol. 137, no. 3534, pp. 993–993, 1962.

[99] M. Topsakal, S. Cahangirov, E. Bekaroglu, and S. Ciraci, "First-principles study of zinc oxide honeycomb structures," *Phys. Rev. B - Condens. Matter Mater. Phys.*, vol. 80, no. 23, 2009.

[100] D. Wu, M. G. Lagally, and F. Liu, "Stabilizing graphitic thin films of wurtzite materials by epitaxial strain," *Phys. Rev. Lett.*, vol. 107, no. 23, 2011.

[101] A. N. Baranov, P. S. Sokolov, V. A. Tafeenko, C. Lathe, Y. V. Zubavichus, A. A. Veligzhanin, M. V. Chukichev, and V. L. Solozhenko, "Nanocrystallinity as a route to metastable phases: Rock salt ZnO," *Chem. Mater.*, vol. 25, no. 9, pp. 1775–1782, 2013.

[102] C. L. Freeman, F. Claeyssens, N. L. Allan, and J. H. Harding, "Graphitic Nanofilms as Precursors to Wurtzite Films: Theory," *Phys. Rev. Lett.*, vol. 96, no. 6, p. 066102, 2006.

[103] B.-H. Liu, M. E. McBriarty, M. J. Bedzyk, S. Shaikhutdinov, and H.-J. Freund, "Structural Transformations of Zinc Oxide Layers on Pt(111)," *J. Phys. Chem. C*, vol. 118, no. 49, pp. 28725–28729, 2014.

[104] C. Tusche, H. L. Meyerheim, and J. Kirschner, "Observation of depolarized ZnO(0001) monolayers: Formation of unreconstructed planar sheets," *Phys. Rev. Lett.*, vol. 99, no. 2, 2007.

[105] A.-Y. Lu, H. Zhu, J. Xiao, C.-P. Chuu, Y. Han, M.-H. Chiu, C.-C. Cheng, C.-W. Yang, K.-H. Wei, Y. Yang, Y. Wang, D. Sokaras, D. Nordlund, P. Yang, D. A. Muller, M.-Y. Chou, X. Zhang, and L.-J. Li, "Janus monolayers of transition metal dichalcogenides," *Nat. Nanotechnol.*, vol. 12, no. 8, pp. 744–749, 2017.

[106] A. Manchon, H. C. Koo, J. Nitta, S. M. Frolov, and R. A. Duine, "New perspectives for Rashba spin-orbit coupling," *Nat. Mater.*, vol. 14, no. 9, pp. 871–882, 2015.

[107] Y. C. Cheng, Z. Y. Zhu, M. Tahir, and U. Schwingenschlögl, "Spin-orbit-induced spin splittings in polar transition metal dichalcogenide monolayers," *EPL*, vol. 102, no. 5, 2013.

[108] S. H. Su, Y. Te Hsu, Y. H. Chang, M. H. Chiu, C. L. Hsu, W. T. Hsu, W. H. Chang, J. H. He, and L. J. Li, "Band gap-tunable molybdenum sulfide selenide monolayer alloy," *Small*, vol. 10, no. 13, pp. 2589–2594, 2014.

[109] R. M. Corn and D. A. Higgins, "Optical Second Harmonic Generation as a Probe of Surface Chemistry," *Chem. Rev.*, vol. 94, no. 1, pp. 107–125, 1994.

[110] L. M. Malard, T. V. Alencar, A. P. M. Barboza, K. F. Mak, and A. M. De Paula,

"Observation of intense second harmonic generation from MoS2 atomic crystals," *Phys. Rev. B - Condens. Matter Mater. Phys.*, vol. 87, no. 20, 2013.

[111] M. E. Lines and A. M. (Alastair M. . Glass, *Principles and applications of ferroelectrics and related materials*. Clarendon Press, 2001.

[112] M. Dawber, K. M. Rabe, and J. F. Scott, "Physics of thin-film ferroelectric oxides," *Rev. Mod. Phys.*, vol. 77, no. 4, pp. 1083–1130, 2005.

[113] T. Egami, S. Ishihara, and M. Tachiki, "Lattice effect of strong electron correlation: implication for ferroelectricity and superconductivity.," *Science*, vol. 261, no. 5126, pp. 1307–10, 1993.

[114] A. K. Yadav, C. T. Nelson, S. L. Hsu, Z. Hong, J. D. Clarkson, C. M. Schlepütz, A. R. Damodaran, P. Shafer, E. Arenholz, L. R. Dedon, D. Chen, A. Vishwanath, A. M. Minor, L. Q. Chen, J. F. Scott, L. W. Martin, and R. Ramesh, "Observation of polar vortices in oxide superlattices," *Nature*, vol. 530, pp. 198–201, 2016.

[115] J. F. Scott, "Applications of Modern Ferroelectrics," *Science (80-.).*, vol. 315, no. 5814, pp. 954–959, 2007.

[116] E. A. Eliseev, S. V. Kalinin, and A. N. Morozovska, "Finite size effects in ferroelectric-semiconductor thin films under open-circuit electric boundary conditions," *J. Appl. Phys.*, vol. 117, no. 3, p. 034102, 2015.

[117] C. H. Ahn, K. M. Rabe, and J.-M. J.-M. Triscone, "Ferroelectricity at the Nanoscale: Local Polarization in Oxide Thin Films and Heterostructures," *Science (80-.).*, vol. 303, no. 5657, pp. 488–491, 2004.

[118] J. Junquera and P. Ghosez, "Critical thickness for ferroelectricity in perovskite ultrathin films," *Nature*, vol. 422, no. February, pp. 506–509, 2003.

[119] Y. Wang, M. K. Niranjan, K. Janicka, J. P. Velev, M. Y. Zhuravlev, S. S. Jaswal, and E. Y. Tsymbal, "Ferroelectric dead layer driven by a polar interface," *Phys. Rev. B - Condens. Matter Mater. Phys.*, vol. 82, no. 9, 2010.

[120] C. G. Duan, R. F. Sabirianov, W. N. Mei, S. S. Jaswal, and E. Y. Tsymbal, "Interface effect on ferroelectricity at the nanoscale," *Nano Lett.*, vol. 6, no. 3, pp. 483–487, 2006.

[121] C.-L. Jia, V. Nagarajan, J.-Q. He, L. Houben, T. Zhao, R. Ramesh, K. Urban, and R. Waser, "Unit-cell scale mapping of ferroelectricity and tetragonality in epitaxial ultrathin ferroelectric films.," *Nat. Mater.*, vol. 6, no. 1, pp. 64–69, 2007.

[122] Y. Saito, Y. Kasahara, J. Ye, Y. Iwasa, and T. Nojima, "Metallic ground state in an ion-gated two-dimensional superconductor.," *Science*, no. October, p. 33, 2015.

[123] Y. Yu, F. Yang, X. F. Lu, Y. J. Yan, H. ChoYong, L. Ma, X. Niu, S. Kim, Y.-W. Son, D. Feng, S. Li, S.-W. Cheong, X. H. Chen, and Y. Zhang, "Gate-tunable phase transitions in thin flakes of 1T-TaS2," *Nat Nano*, vol. 10, no. 3, pp. 270–276, Jan. 2015.

[124] K. Chang, L. Junwei, L. Haicheng, N. Wang, K. Zhao, A. Zhang, F. Jin, Y. Zhong, X. Hu, W. Duan, Q. Zhang, L. Fu, Q.-K. Xue, X. Chen, and S.-H. Ji, "Discovery of robust in-plane ferroelectricity in atomic-thick SnTe," *Science (80-.).*, vol. 353, no. 6296, pp. 274–278, 2016.

[125] F. Liu, L. You, K. L. Seyler, X. Li, P. Yu, J. Lin, X. Wang, J. Zhou, H. Wang, H. He, S. T.

Pantelides, W. Zhou, P. Sharma, X. Xu, P. M. Ajayan, J. Wang, and Z. Liu, “Room-temperature ferroelectricity in CuInP2S6 ultrathin flakes,” *Nat. Commun.*, vol. 7, p. 12357, 2016.

[126] W. Ding, J. Zhu, Z. Wang, Y. Gao, D. Xiao, Y. Gu, Z. Zhang, and W. Zhu, “Prediction of intrinsic two-dimensional ferroelectrics in In2Se3 and other III2-VI3 van der Waals materials,” *Nat. Commun.*, vol. 8, p. 14956, 2017.

[127] G. A. Samara, T. Sakudo, and K. Yoshimitsu, “Important generalization concerning the role of competing forces in displacive phase transitions,” *Phys. Rev. Lett.*, vol. 35, no. 26, pp. 1767–1769, 1975.

[128] W. J. Hu, D.-M. Juo, L. You, J. Wang, Y.-C. Chen, Y.-H. Chu, and T. Wu, “Universal ferroelectric switching dynamics of vinylidene fluoride-trifluoroethylene copolymer films.,” *Sci. Rep.*, vol. 4, p. 4772, 2014.

[129] M. Li, Y. Gu, Y. Wang, L. Q. Chen, and W. Duan, “First-principles study of 180 domain walls in BaTiO3: Mixed Bloch-Neel-Ising character,” *Phys. Rev. B - Condens. Matter Mater. Phys.*, vol. 90, no. 5, p. 054106, 2014.

[130] B. Meyer and D. Vanderbilt, “Ab initio study of ferroelectric domain walls in PbTiO3,” *Phys. Rev. B*, vol. 65, no. 10, p. 104111, 2002.

[131] X. Tao and Y. Gu, “Crystalline-crystalline phase transformation in two-dimensional In2Se3 thin layers.,” *Nano Lett.*, vol. 13, no. 8, pp. 3501–5, 2013.

[132] W. Feng, W. Zheng, F. Gao, X. Chen, G. Liu, T. Hasan, W. Cao, and P. Hu, “Sensitive Electronic-Skin Strain Sensor Array Based on the Patterned Two-Dimensional α-In2Se3,” *Chem. Mater.*, p. acs.chemmater.6b01073, 2016.

[133] Y. R. Shen, *Principles of Nonlinear Optics*. 2002.

[134] Y. Li, Y. Rao, K. F. Mak, Y. You, S. Wang, C. R. Dean, and T. F. Heinz, “Probing symmetry properties of few-layer MoS2 and h-BN by optical second-harmonic generation,” *Nano Lett.*, vol. 13, no. 7, pp. 3329–3333, 2013.

[135] K. Franke, J. Besold, W. Haessler, and C. Seegebarth, “Modification and detection of domains on ferroelectric PZT films by scanning force microscopy,” *Surf. Sci.*, vol. 302, no. 1–2, 1994.

[136] B. J. Rodriguez, C. Callahan, S. V. Kalinin, and R. Proksch, “Dual-frequency resonance-tracking atomic force microscopy,” *Nanotechnology*, vol. 18, no. 47, 2007.

[137] N. Balke, P. Maksymovych, S. Jesse, A. Herklotz, A. Tselev, C. B. Eom, I. I. Kravchenko, P. Yu, and S. V. Kalinin, “Differentiating Ferroelectric and Nonferroelectric Electromechanical Effects with Scanning Probe Microscopy,” *ACS Nano*, vol. 9, no. 6, pp. 6484–6492, 2015.

[138] Q. Chen, Y. Shen, S. Zhang, and Q. M. Zhang, “Polymer-Based Dielectrics with High Energy Storage Density,” *Annu. Rev. Mater. Res.*, vol. 45, no. 1, pp. 433–458, 2015.

[139] A. V. Kolobov and J. Tominaga, *Two-Dimensional Transition-Metal Dichalcogenides*, vol. 239. Cham: Springer International Publishing, 2016.

[140] Q. H. Wang, K. Kalantar-Zadeh, A. Kis, J. N. Coleman, and M. S. Strano, “Electronics and optoelectronics of two-dimensional transition metal dichalcogenides,” *Nat.*

Nanotechnol., vol. 7, no. 11, pp. 699–712, Nov. 2012.

[141] H. Li, X. Duan, X. Wu, X. Zhuang, H. Zhou, Q. Zhang, X. Zhu, W. Hu, P. Ren, P. Guo, L. Ma, X. Fan, X. Wang, J. Xu, A. Pan, and X. Duan, "Growth of alloy MoS2xSe2(1-x) nanosheets with fully tunable chemical compositions and optical properties," *J. Am. Chem. Soc.*, vol. 136, no. 10, pp. 3756–3759, 2014.

[142] B. Fultz, *Phase Transitions in Materials*. Cambridge: Cambridge University Press, 2014.

[143] W. Hanke and Y. V. Kopaev, *Electronic phase transitions*. North-Holland, 1992.

[144] O. Tegus, E. Brück, K. H. J. Buschow, and F. R. de Boer, "Transition-metal-based magnetic refrigerants for room-temperature applications.," *Nature*, vol. 415, no. 6868, pp. 150–152, 2002.

[145] J. J. Yang, D. B. Strukov, and D. R. Stewart, "Memristive devices for computing," *Nat. Nanotechnol.*, vol. 8, no. 1, pp. 13–24, Dec. 2012.

[146] K. F. Mak, C. Lee, J. Hone, J. Shan, and T. F. Heinz, "Atomically Thin MoS 2 : A New Direct-Gap Semiconductor."

[147] Y. Ma, L. Kou, X. Li, Y. Dai, S. C. Smith, and T. Heine, "Quantum spin Hall effect and topological phase transition in two-dimensional square transition-metal dichalcogenides," *Phys. Rev. B*, vol. 92, no. 8, p. 085427, Aug. 2015.

[148] M. Wuttig and N. Yamada, "Phase-change materials for rewriteable data storage," *Nat. Mater.*, vol. 6, no. 11, pp. 824–832, 2007.

[149] G. Eda, T. Fujita, H. Yamaguchi, D. Voiry, M. Chen, and M. Chhowalla, "Coherent atomic and electronic heterostructures of single-layer MoS 2," *ACS Nano*, vol. 6, no. 8, pp. 7311–7317, 2012.

[150] C. Zhang, S. Kc, Y. Nie, C. Liang, W. G. Vandenberghe, R. C. Longo, Y. Zheng, F. Kong, S. Hong, R. M. Wallace, and K. Cho, "Charge Mediated Reversible Metal-Insulator Transition in Monolayer MoTe2 and WxMo1-xTe2 Alloy," *ACS Nano*, vol. 10, no. 8, pp. 7370–7375, 2016.

[151] M. Kan, J. Y. Wang, X. W. Li, S. H. Zhang, Y. W. Li, Y. Kawazoe, Q. Sun, and P. Jena, "Structures and Phase Transition of a MoS 2 Monolayer," *J. Phys. Chem. C*, vol. 118, no. 3, pp. 1515–1522, 2014.

[152] Y. Kang, S. Najmaei, Z. Liu, Y. Bao, Y. Wang, X. Zhu, N. J. Halas, P. Nordlander, P. M. Ajayan, J. Lou, and Z. Fang, "Plasmonic Hot Electron Induced Structural Phase Transition in a MoS2 Monolayer," *Adv. Mater.*, vol. 26, no. 37, pp. 6467–6471, 2014.

[153] S. Cho, S. Kim, J. H. Kim, J. Zhao, J. Seok, D. H. Keum, J. Baik, D.-H. Choe, K. J. Chang, K. Suenaga, S. W. Kim, Y. H. Lee, and H. Yang, "Phase patterning for ohmic homojunction contact in MoTe2," *Science (80-.).*, vol. 349, no. 6248, pp. 625–628, 2015.

[154] D. H. Keum, S. Cho, J. H. Kim, D.-H. Choe, H.-J. Sung, M. Kan, H. Kang, J.-Y. Hwang, S. W. Kim, H. Yang, K. J. Chang, and Y. H. Lee, "Bandgap opening in few-layered monoclinic MoTe2," *Nat. Phys.*, vol. 11, no. 6, pp. 482–486, May 2015.

[155] Y.-C. Lin, D. O. Dumcenco, Y.-S. Huang, and K. Suenaga, "Atomic mechanism of the semiconducting-to-metallic phase transition in single-layered MoS2.," *Nat. Nanotechnol.*, vol. 9, no. 5, pp. 391–6, Apr. 2014.

[156] R. Kappera, D. Voiry, S. E. Yalcin, B. Branch, G. Gupta, A. D. Mohite, and M. Chhowalla, “Phase-engineered low-resistance contacts for ultrathin MoS2 transistors.,” *Nat. Mater.*, vol. 13, no. August, pp. 1–15, 2014.

[157] C. M, “Photoluminescence from Chemically Exfoliated MoS2,” *Nano Lett.*, vol. 12, no. 12, p. 526, 2012.

[158] M. a. Py and R. R. Haering, “Structural destabilization induced by lithium intercalation in MoS 2 and related compounds,” *Can. J. Phys.*, vol. 61, no. 1, pp. 76–84, 1983.

[159] P. J. Mulhern, “Lithium intercalation in crystalline Li $_x$ MoS $_2$,” *Can. J. Phys.*, vol. 67, no. 11, pp. 1049–1052, 1989.

[160] A. Chernikov, A. M. Van Der Zande, H. M. Hill, A. F. Rigosi, A. Velauthapillai, J. Hone, and T. F. Heinz, “Electrical Tuning of Exciton Binding Energies in Monolayer WS2,” *Phys. Rev. Lett.*, vol. 115, no. 12, 2015.

[161] Y. Li, K.-A. N. Duerloo, K. Wauson, and E. J. Reed, “Structural Semiconductor-to-Semimetal Phase Transition in Two-Dimensional Materials Induced by Electrostatic Gating,” *Nat. Commun.*, pp. 1–8, 2016.

[162] Y. Li, K.-A. N. Duerloo, K. Wauson, and E. J. Reed, “Structural semiconductor-to-semimetal phase transition in two-dimensional materials induced by electrostatic gating,” *Nat. Commun.*, vol. 7, p. 10671, Feb. 2016.

[163] J. T. Ye, Y. J. Zhang, R. Akashi, M. S. Bahramy, R. Arita, and Y. Iwasa, “Superconducting Dome in a Gate-Tuned Band Insulator,” *Science (80-.).*, vol. 338, no. 6111, pp. 1193–1196, 2012.

[164] C. Ruppert, O. B. Aslan, and T. F. Heinz, “Optical properties and band gap of single- and few-layer MoTe2 crystals,” *Nano Lett.*, vol. 14, no. 11, pp. 6231–6236, 2014.

[165] J. C. Park, S. J. Yun, H. Kim, J. H. Park, S. H. Chae, S. J. An, J. G. Kim, S. M. Kim, K. K. Kim, and Y. H. Lee, “Phase-Engineered Synthesis of Centimeter-Scale 1T and 2H-Molybdenum Ditelluride Thin Films,” *ACS Nano*, vol. 9, no. 6, pp. 6548–6554, 2015.

[166] D. Sercombe, S. Schwarz, O. Del Pozo-Zamudio, F. Liu, B. J. Robinson, E. a Chekhovich, I. I. Tartakovskii, O. Kolosov, and a I. Tartakovskii, “Optical investigation of the natural electron doping in thin MoS2 films deposited on dielectric substrates,” *Sci. Rep.*, vol. 3, p. 3489, 2013.

[167] J. Xiao, Z. Ye, Y. Wang, H. Zhu, Y. Wang, and X. Zhang, “Nonlinear optical selection rule based on valley-exciton locking in monolayer ws 2,” *Light Sci. Appl.*, vol. 4, 2015.

[168] G. Moody, C. Kavir Dass, K. Hao, C. H. Chen, L. J. Li, A. Singh, K. Tran, G. Clark, X. Xu, G. Berghäuser, E. Malic, A. Knorr, and X. Li, “Intrinsic homogeneous linewidth and broadening mechanisms of excitons in monolayer transition metal dichalcogenides,” *Nat. Commun.*, vol. 6, 2015.

[169] T. Korn, S. Heydrich, M. Hirmer, J. Schmutzler, and C. Schller, “Low-temperature photocarrier dynamics in monolayer MoS2,” *Appl. Phys. Lett.*, vol. 99, no. 10, 2011.

[170] W. T. Hsu, Y. L. Chen, C. H. Chen, P. S. Liu, T. H. Hou, L. J. Li, and W. H. Chang, “Optically initialized robust valley-polarized holes in monolayer WSe 2,” *Nat. Commun.*, vol. 6, 2015.

[171] P. Rivera, K. L. Seyler, H. Yu, J. R. Schaibley, J. Yan, D. G. Mandrus, W. Yao, and X. Xu, "Valley-polarized exciton dynamics in a 2D semiconductor heterostructure," *Science (80-.).*, vol. 351, no. 6274, pp. 688–691, 2016.

[172] J. Kim, C. Jin, B. Chen, H. Cai, T. Zhao, P. Lee, S. Kahn, K. Watanabe, T. Taniguchi, S. Tongay, M. F. Crommie, and F. Wang, "Observation of ultralong valley lifetime in WSe2/MoS2heterostructures," *Sci. Adv.*, vol. 3, no. 7, 2017.

[173] Y. J. Chen, J. D. Cain, T. K. Stanev, V. P. Dravid, and N. P. Stern, "Valley-polarized exciton-polaritons in a monolayer semiconductor," *Nat. Photonics*, vol. 11, no. 7, pp. 431–435, 2017.

[174] H. Zhu, J. Yi, M. Y. Li, J. Xiao, L. Zhang, C. W. Yang, R. A. Kaindl, L. J. Li, Y. Wang, and X. Zhang, "Observation of chiral phonons," *Science (80-.).*, vol. 359, no. 6375, pp. 579–582, 2018.

[175] J.-F. Ge, Z.-L. Liu, C. Liu, C.-L. Gao, D. Qian, Q.-K. Xue, Y. Liu, and J.-F. Jia, "Superconductivity above 100 K in single-layer FeSe films on doped SrTiO3," *Nat. Mater.*, vol. 14, no. 3, pp. 285–289, Nov. 2014.

[176] W. Zhao, C.-Z. Chang, X. Xi, K. F. Mak, J. S. Moodera, F. M. P. A, F. M. P. A. and H. D. A. Fisher D S, N. T. and S. S, G. A. and F. M. P. A. Koch R H, Foglietti V, Gallagher W J, Koren G, R. A. P. and H. F. Jiang W, Yeh N C, Reed D S, Kriplani U, Tombrello T A, L. L. and Z. Z. X. Zhang Y Z, Deltour R, de Marneffe J F, Wen H H, Qin Y L, Dong C, M. M. B. and M. M. P. Taylor B J, Li S, S. K. and A. Y. Xu H, Li S, Anlage S M, Lobb C J, Sullivan M C, C. Y. and X. X. X. Yang H, Jia Y, Shan L, Zhang Y Z, Wen H H, Zhuang C G, Liu Z K, Li Q, S. J. and V. J. L. Villegas J E, Gonzalez E M, Sefrioui Z, V. J. E. and V. J. L, S. M. and C. M. H. W. Sun Y, Wang J, Zhao W W, Tian M L, H. B. W. and G. A. Dekker C, Woltgens P J M, Koch R H, H. B. W. and G. A. Woltgens P J M, Dekker C, Koch R H, W. Q. Y. et al, H. S. L. et al, T. S. Y. et al, L. J. J. et al, X. Q. K. and W. J. Sun Y, Zhang W H, Xing Y, Li F S, Zhao Y F, Xia Z C, Wang L L, Ma X C, Z. W. H. et al, L. Y. and J. J. F. Ge J F, Liu Z L, Liu C H, Gao C L, Qian D, Xue Q K, F. C. A. and H. F. Worthington T K, Fisher M P A, Huse D A, Toner J, Marwick A D, Zabel T, G. A. M. and K. A. M. Epstein K, H. A. F. and F. A. T, E. K. and G. A. M. Kadin A M, Z. W. et al, and T. M, "Vortex phase transitions in monolayer FeSe film on SrTiO3," *2D Mater.*, vol. 3, no. 2, p. 024006, Apr. 2016.

[177] X. Xi, H. Berger, L. Forró, J. Shan, and K. F. Mak, "Gate Tuning of Electronic Phase Transitions in Two-Dimensional NbSe 2," *Phys. Rev. Lett.*, vol. 117, no. 10, p. 106801, Aug. 2016.

[178] S. Sachdev, *Quantum phase transitions*. 2011.

[179] M. Vojta, "Quantum phase transitions," *Rep. Prog. Phys.*, vol. 66, pp. 2069–2110, 2003.

[180] A. W. Tsen, B. Hunt, Y. D. Kim, Z. J. Yuan, S. Jia, R. J. Cava, J. Hone, P. Kim, C. R. Dean, and A. N. Pasupathy, "Nature of the quantum metal in a two-dimensional crystalline superconductor," *Nat. Phys.*, vol. 12, no. 3, pp. 208–212, Dec. 2015.